Master thesis and internship[BR]- Master's thesis : Investigation of the transition to turbulence on a flat-plate boundary layer at supercritical pressure[BR]- Integration Internship : Delft University of Technology

Auteur : Gaspar, Romain
Promoteur(s) : Terrapon, Vincent
Faculté : Faculté des Sciences appliquées
Diplôme : Master en ingénieur civil en aérospatiale, à finalité spécialisée en "aerospace engineering"
Année académique : 2022-2023
URI/URL : http://hdl.handle.net/2268.2/17888

University of Liege
Faculty of applied sciences
Academic Year 2022-2023

Investigation of the transition to turbulence on a flat-plate boundary layer at supercritical pressure

Author: Romain Gaspar

Thesis supervisors: Prof. Vincent E. Terrapon

Prof. Rene Pecnik

Dr. Benjamin Bugeat

M.Sc. Pietro Carlo Boldini

Research project conducted at the Process and Energy Department, 3mE Faculty, Delft University of Technology

Master thesis presented in partial fulfillment of the requirements for the degree of Master in Aerospace Engineering

Acknowledgements

First of all, I would like to express my deep gratitude to my research supervisor Rene Pecnik, his postdoctoral researcher, Benjamin Bugeat and his PhD student, Pietro Carlo Boldini for providing guidance throughout this work and for giving me the opportunity to do my master's thesis at the Process and Energy Department at TU Delft. Their availability and kindness ensured that I received excellent supervision throughout the internship and the process of writing this thesis.

I would like to thank my promoter in Liège, Prof. V.E. Terrapon, for his support, his useful advice and for making this exchange possible.

Finally, I want to thank my friends for their kind support throughout our studies, my girlfriend who let me live away from her during this period and my parents for always believing in me.

Abstract

This thesis investigates the development and breakdown of a transcritical boundary layer over a zero-pressure-gradient flat-plate with a heated isothermal wall by solving the full compressible Navier-Stokes equations using direct numerical simulations. The wall temperature is adjusted to ensure that the temperature profile varies through the pseudo-critical temperature within the boundary layer to form a transcritical boundary layer. The discovery of an additional unstable mode in this configuration, referred to as Mode II, exhibiting a wider and stronger unstable range in comparison to Mode I, has led to significant interest in comprehending the resulting transitions. The pronounced non-ideality of a supercritical fluid requires the use of the Van der Waals equation of state. The results of this analysis reveal that the strong gradient of properties at the Widom line becomes more pronounced as the free-stream pressure approaches the critical point, thereby complicating the grid analysis. An increase in the free-stream pressure or a reduction in the Mach number elicits a wider and lower peak within the density fluctuation profiles, thereby alleviating the restrictions on mesh quality. This study highlights the pronounced non-ideal behaviour of fluids in the transcritical regime, leading to the generation of higher harmonics with significant amplitudes and the occurrence of spurious pressure field oscillations. To mitigate these issues, a new method that uses the shape function derived from the linear stability theory as the imposed disturbances was implemented but proved unsuccessful in reducing the amplitude of these additional frequency components. To address the problem of spurious oscillations, modifications were made to the kinetic-energy and entropy preserving scheme. These modifications ensured discrete verification of pressure equilibrium for an ideal-gas, leading to a reduction in undesirable oscillations in the present supercritical fluid. The skin-friction coefficient, which serves as an indicator of transition, undergoes significant modifications within a transcritical boundary layer. This includes lower values in both the laminar and turbulent regimes, as well as significantly reduced growth rates and amplitudes of the overshoot, in comparison to subcritical conditions. This modification has been attributed to the different breakdown of the coherent structures, such as the $\Lambda-$vortices, that are significantly altered by the variations in quantities such as density, internal energy, and temperature, resulting in an accelerated interaction along the span. The investigation into various physical parameters has unveiled a delayed transition phenomenon when the free-stream pressure is increased. This delay is attributed to the delayed primary and secondary instability, resulting in a slowed growth of distinct oblique modes and consequently the friction coefficient. The analysis of mean turbulent statistics highlights a decrease in the amplitude of fluctuations in density, viscosity, and specific heat as the pressure increases. Consequently, there is a reduction in the deviation of the mean velocity profiles in the log-law region, in comparison to an ideal-gas scenario, as the pressure is raised. Furthermore, the decrease in the Eckert number to eliminate compressibility effects leads to a slight delay in the transition, accompanied by lower amplitude $\Lambda-$vortices. However, this decrease does not produce significant modifications in the turbulent statistics of fully turbulent flows, but it reduces the peak in the density fluctuation profiles, thereby facilitating its numerical capture. Finally, it has been demonstrated that increasing the wall temperature in a transcritical boundary layer expands both the range and strength of the unstable Mode II, resulting in an earlier transition, which contrast to the observations in a subcritical simulation. Overall, this study provides insights into the breakdown of supercritical boundary layers and on the influence of thermodynamic variations on flow characteristics and turbulence statistics.

Contents

List of Figures

Nomenclature

Acronyms

DNS	Direct Numerical Simulations
EoS	Equation of State
FFT	Fast Fourier Transform
IG	Ideal-Gas
LES	Large Eddy Simulations
LST	Linear Stability Theory
SCF	SuperCritical Fluid
TS	Tollmien-Schlichting
VdW	Van der Waals

Dimensionless Numbers

Ec	Eckert number
Ma	Mach number
Pr	Prandtl number
Re	Reynolds number

Superscripts and Subscripts

$(\cdot)'$	Fluctuation quantity
$(\cdot)^*$	Dimensional quantity
$(\cdot)_\infty$	Free-stream quantity
$(\cdot)_i$	Imaginary part of a quantity
$(\cdot)_r$	Real part of a quantity
$(\cdot)_w$	Wall quantity
$(\cdot)_c$	Critical value
$(\cdot)_{pc}$	Pseudo-critical value

$(\cdot)_{ref}$ Reference value

$\bar{(\cdot)}$ Time-averaged quantity

$\hat{(\cdot)}$ Fourier-transformed quantity

Symbols

Amplitude

α Streamwise wavenumber

α_i Local growth rate

β Spanwise wave number

$\mathbf{q}$ Perturbation vector

δ_{99} non-dimensional 99% boundary layer thickness

η, ζ self-similar coordinates

γ Ratio of specific heats

κ Heat conductivity

μ Dynamic viscosity

ω_i Angular frequency of perturbation

ρ Density

σ Sponge strength

τ_{ij} Viscous stress tensor

c Speed of sound

C_p Specific heat capacity

E Total energy

F Dimensionless frequency of perturbation

h Enthalpy

l_0 Characteristic length

L_x Streamwise domain length

L_y Wall-normal domain length

L_z Spanwise domaine length

L_{sp} Sponge length

n_x Maximal number of grid points in the streamwise direction

n_y Maximal number of grid points in the wall-normal direction

n_z Maximal number of grid points in the spanwise direction

p	Pressure
q_i	Heat-flux vector
R	Ideal gas constant
S_f	Grid-stretching factor
T	Temperature
T_{cr}	Critical Temperature
T_{pc}	Pseudo-critical Temperature
T_w	Wall Temperature
u	Streamwise velocity
v	Wall-normal velocity
w	Spanwise velocity
x	Streamwise coordinate
y	Wall-normal coordinate
z	Spanwise coordinate

Chapter 1

Introduction

The increasing demand for energy, coupled with major events such as the 500% increase in CO_2 emission quotas between 2018 and 2021 [1], as well as the war in Ukraine, has led to a surge in energy prices. Consequently, there is a constant need for research focused on enhancing the efficiency of existing energy production systems. In many industrial energy production, fluids are subjected to high Reynolds numbers such that the flow transition from a laminar to a turbulent state. This transition is attributed to the amplification of small disturbances within the flow. As the Reynolds number increases, the inertial forces become more dominant, rendering the flow more susceptible to transition [2]. Predicting the onset of turbulence is crucial in practical applications because the transition results in a significant increase in the friction coefficient and heat transfer. Depending on the specific application, it may be advantageous to either delay or intentionally trigger this transition [3]. Therefore, hydrodynamic stability is used to identify the conditions that promote the amplification of disturbances, leading to transition. The types of transition are determined by the specific flow characteristics and the nature of perturbation [4]. The experiments of Klebanoff *et al.* [5] and Kovasznay *et al.* [6] on forced transition in incompressible flow over a flat-plate attempts to describe theoretically the transition phenomena. Perturbations were introduced within the boundary layer to artificially induce finite-amplitude Tollmien-Schlichting waves using the vibrating ribbon technique. The introduction of small perturbations initiates the interaction of various instability modes, leading to the breakdown of the laminar flow and resulting in enhanced mixing and increased turbulence intensity. Different works have been conducted on the transition to turbulence induced by naturally occurring disturbances [7] and [8]). However, the precise mechanisms underlying the introduction of these disturbances are unknown.

The groundbreaking discovery of the critical point of a substance by Baron Charles Cagniard de la Tour during his cannon barrel experiments [9] revolutionised the understanding of fluid behaviour. This discovery introduced the concept of a single supercritical fluid phase, which combines the advantageous properties of both gases and liquids. The unique combination of gas-like viscosity and diffusivity, along with liquid-like density, makes supercritical fluids an optimal choice for various applications, as demonstrated by Brunner [10]. One of the notable advantages is the ability to finely tune the thermophysical properties of supercritical fluids by adjusting the operating pressure and temperature. Among the commonly used fluids, carbon dioxide (CO_2) stands out due to its relatively low critical pressure of 7.4 MPa and critical temperature of 31 degrees Celsius, making it a cost-effective option for achieving the supercritical state as discussed by Haas [11]. Moreover, it is important to emphasise the low compression ratio of supercritical CO_2, which contributes to higher compressor efficiency and a larger volumetric refrigeration capacity [12]. These characteristics enable the reduction in system size of a compressor system and the associated costs. The unique heat transfer and refrigeration properties also make it suitable for various applications, including conductor cooling for achieving superconductivity effects, cooling of rockets and military aircraft, and cooling of turbine blades.

These industrial applications have led to extensive research to better understand the behaviour and

the characteristics of a supercritical fluid in laminar and turbulent flows separately. For example, Sengupta *et al.* [13] analysed the behaviour of supercritical turbulent flow over a flat-plate, at low Mach number close to its vapour-liquid critical point, from which they showed that the mean turbulent statistics are dependent on the location of the transcritical temperature. Later, Kawai [14] studied the behaviour of a heated transcritical boundary layer at supercritical pressure for parahydrogen. He showed the abrupt variations of thermodynamic properties through the pseudo-critical temperature. More specifically, he noticed that the large density fluctuations $\sqrt{\overline{\rho'\rho'}}/\bar{\rho} \approx 0.4 - 1.0$ induced within the transcritical turbulent boundary layer significantly alter the near-wall turbulence and the resultant turbulent statistics. These observations challenge Morkovin's hypothesis [15], which assumes that at moderate Mach numbers, "*the essential dynamics of these shear flows will follow the incompressible pattern.*" According to Morkovin's hypothesis, the impact of density fluctuations on turbulence can be disregarded if the root mean squared density fluctuations are relatively small compared to the absolute density i.e. $\sqrt{\overline{\rho'\rho'}}/\bar{\rho} << 1$. However, the observations made by Kawai [14] reveal the significant presence of density fluctuations in a transcritical boundary layer. These findings invalidate Morkovin's hypothesis and highlight the importance of considering density fluctuations in such flows.
These direct numerical simulations also reveal some numerical issues associated with the use of a supercritical fluid. These include the amplification of aliasing errors through nonlinear interactions, as observed by Coppola [16]. Additionally, other studies by Abgrall [17] and, recently, Shima *et al.* [18] have demonstrated that the pressure equilibrium at the interface between gas-like and liquid-like phases is not maintained when using a classic kinetic-energy entropy preservation scheme, which is employed in this study. This lack of pressure equilibrium leads to the generation of spurious pressure oscillations, which affect the flow physics. Furthermore, Schmitt [19] demonstrated in his study of transcritical fluids that pressure oscillations can result in solution divergence.

1.1 Theoretical review

Hydrodynamic stability is used to gain a better insight into the pathway connecting a purely laminar flow to a fully turbulent flow. This field of research aims to investigate how a flow responds when subjected to disturbances of a certain magnitude, which trigger instabilities in the flow field. There are two possible outcomes: firstly, the instabilities may decay, leading the flow to return to its original laminar state; secondly, the instabilities may be amplified by the flow, causing a radical change in fluid movement and leading to a chaotic state known as turbulence. In this study, the focus is directed towards understanding this second scenario, where the flow undergoes a transition to turbulence. In Fig 1.1, Morkovin's research highlighted the various pathways existing for transitioning from laminar to turbulent flow. Each path represents a distinct route which depends on the initial disturbance level present in the flow. The first crucial step in all paths involves the generation and receptivity of perturbations within the boundary layer, which serves as a common basis for all transition routes.

1.1.1 Transition to a turbulent flow

A significant amount of research has been conducted to comprehend the physical mechanisms involved in transition from a laminar to a turbulent boundary layer. The pioneering work of Morkovin [15] has provided valuable insights into the different potential mechanisms that contribute to the breakdown of laminar flow. These different routes are presented in Fig 1.1.

Morkovin's work emphasises that the specific route to turbulence is influenced by the nature and characteristics of the initially introduced perturbations in the flow. These disturbances can be triggered by various mechanisms, including external factors such as free-stream turbulence or surface

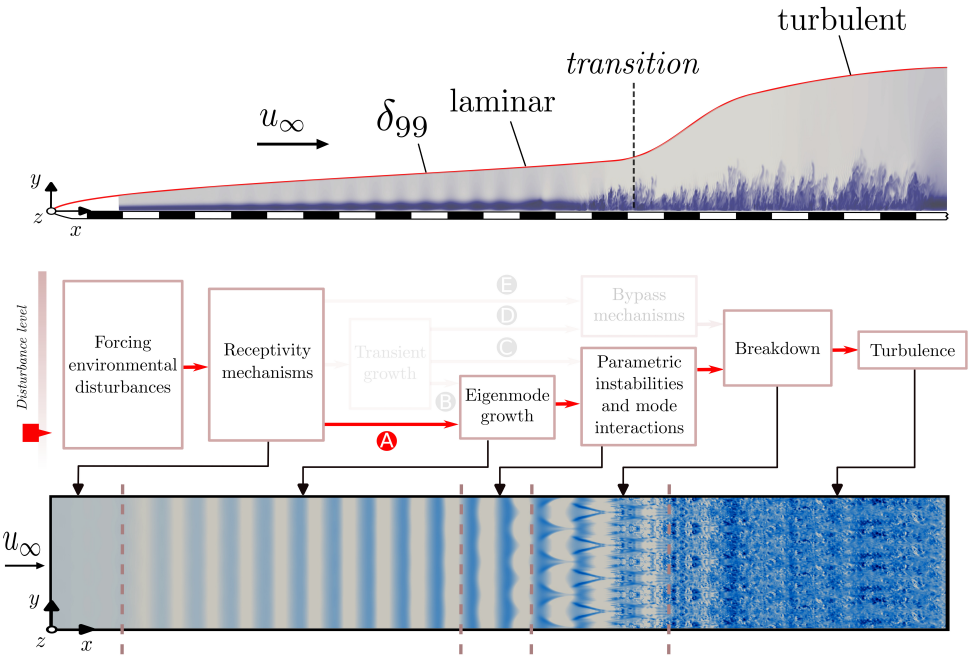

Figure 1.1: The various potential pathways from a laminar boundary layer to a turbulent boundary layer. Inspired from Morkovin [15].

imperfections, as well as internal factors inherent to the flow. The receptivity mechanisms act as the gateway for these perturbations to enter the laminar flow and initiate the transition process. In this study, a particular pathway, denoted as A in Fig 1.1, is investigated. This path is associated with a natural transition process that occurs when the initial disturbance level in the flow is relatively small. Disturbances in the flow are characterised by different spatial and temporal patterns, which are represented by various eigenmodes. Each eigenmode corresponds to a specific frequency and wavelength. For path A, the primary instability occurs first, where $2D$ modes exhibit an exponential growth in amplitude over time. Once the amplitude of these disturbances reaches a certain threshold, nonlinear effects become significant. Specifically, the base flow and the primary instability combine to form a new periodic stable flow, which can then undergo a second instability, hence its name. The secondary instability is characterised by a higher growth rate in the amplitude of different oblique modes. The growth of these modes introduces additional nonlinear effects arising from the interaction between the fundamental and oblique modes. These nonlinear interactions give rise to the formation of coherent structures and turbulent spots, as observed by Jimenez and Javier [20].
Conversely, transient growth, which refers to a temporary amplification of perturbation magnitude within a flow that is linearly stable [21], will not be studied. The bypass transition, labelled as path E can occur when moderate or high levels of disturbances induce the flow to directly transition to turbulence, bypassing the growth and interactions of the eigenmodes. This transition pathway does not rely on the modest growth and interaction of eigenmodes but instead involves a more direct route to turbulence.

1.1.2 Linear Stability Theory

The Linear Stability Theory (LST), proposed by Rayleigh [22], provides an efficient and cost-effective approach to accurately predict the linear behaviour of a flow. This tool makes it possible to gain valuable insights into the growth of modal perturbations during the linear regime, eliminating the

need to solve the full compressible Navier-Stokes Equations. Its application to compressible flows over a flat-plate has been investigated several times and has demonstrated good accuracy when compared with higher-fidelity or empirical results, as reported by Ozgen [23], Lees [24], and Malik [25]. Different authors: Gaster [26] and Smith [27], and the present study, have considered a parallel base flow in their investigations, which neglects the wall-normal velocity and the growth of the boundary layer. This approximation proves to be valid various practical scenarios where the flow can be approximated as nearly parallel. All studies agree that the parallel-flow approximation remains accurate when the excitation frequencies are sufficiently low. On top of that, Fani *et al.* [28] explained that the LST neglects higher harmonics as their amplitude are lower than that of the fundamental mode and do not significantly contribute to the initial growth of disturbances. This basic theory relies on linearising the NSE by decomposing the flow into small disturbances superimposed on a mean flow. The LST assumes that the eigenfunction of the perturbations exhibits variation only along the wall-normal direction, while their amplitude depends on the streamwise and spanwise positions, the spanwise wavenumber, the angular frequency, and time. The linearised stability equations are obtained by neglecting the higher-order perturbations, through the small amplitude assumption. The detailed expressions are found in Ren *et al.*'s [29].

1.1.3 Secondary instability over a flat-plate

In this study, the amplification of small initial disturbances along a flat-plate, will be analysed, following path A depicted in Fig 1.1. The dominant two-dimensional instabilities observed on this geometry are the Tollmien–Schlichting (TS) waves, which were discovered by Tollmien and Schlichting [30] [31] and results from the unstable Mode I. If a detached boundary layer is present (although not in the scope of this study), the instabilities associated with it are commonly referred to as Kelvin-Helmholtz instabilities. Although the TS waves indicate the first instability in the flow, the breakdown to turbulence is caused by a second instability that, unlike the primary instability, does not saturate in amplitude. As the amplitude of the second instability grows and approaches the amplitude of the TS wave, an interaction occurs between them, giving rise to three-dimensional structures known as coherent structures [32]. In the flat-plate boundary layer case, the early coherent structures are the Λ-shaped vortices that have been numerically investigated by Rist & Fasel [33]. These vortices evolve through the boundary layer and eventually form the hairpin-shaped loops, which precede the onset of turbulence. Extensive studies have been conducted on these vortices to investigate their characteristics and the formation mechanisms attributed to shear instability (Monkewitz & Chomaz [34], Christensen & Adrian [35]).

Herbert classifies the second instabilities of the TS wave into three types: fundamental modes, subharmonic modes, and detuned mode. The fundamental mode refers to the interaction of oblique waves and the fundamental TS wave with the same frequency. This scenario generates successive Λ vortices that are aligned, as shown in Fig 1.2, it refers to the K-type transition, which has been studied by Saric & Thomas [36] and observed by Meyer & Rist [33]. The second type occurs when the subharmonic fluctuation is excited with the frequency of the fundamental TS wave. Those interactions delayed the transition compared to the fundamental mode, and instead of an aligned pattern of Λ vortices. Flow visualisation reveals a staggered pattern of Λ vortices as shown Fig 1.2. This second scenario corresponds to the H-type transition, described by Herbert. This is confirmed by Sayadi [37] which demonstrated that, under similar disturbance amplitudes, the K-type transition has an earlier onset compared to the H-type transition. This difference can be attributed to the more rapid formation of key vortical structures, such as Λ, hairpins, and Ω vortices, resulting from the excitation of both fundamental and subharmonic frequencies. Bake *et al.* [38] reveals that each Λ-vortex found in the staggered pattern during an H-type transition is developed by the same nonlinear mechanisms as the aligned Λ pattern in the K-type transition. Those two scenarios have been observed experimentally by Kachanov *et al.* [39] and numerically by Fasel, Rist & Konzelmann [40]. The last scenario, known as

the oblique transition was introduced by Schmid & Henningson [41]. It involves a different mechanism compared to the standard TS-wave scenario. It requires the introduction of two oblique waves with small amplitudes. Although these oblique waves have small amplitudes, as they propagate, interact, and amplify, they trigger a transition process similar to bypass transition described in the work by Elofsson [42].

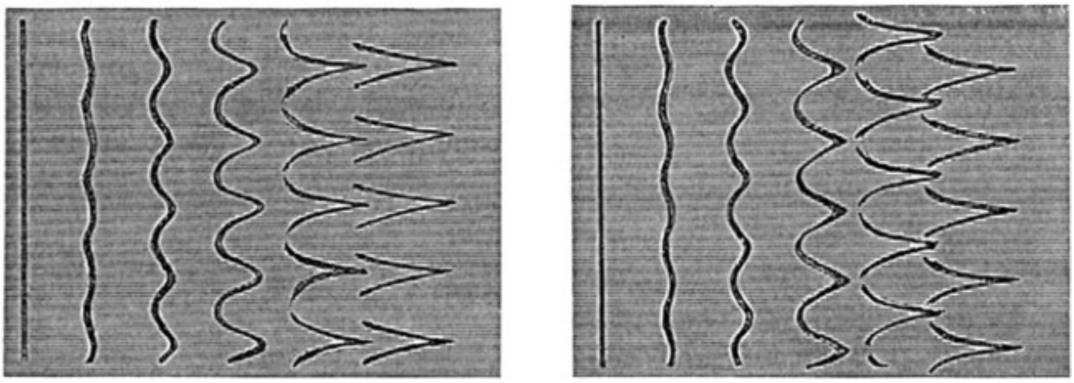

Figure 1.2: Representation of the arrangement Λ-vortices caused by a fundamental mode (left) and a subharmonics mode (right). The flow goes from left to right. Figure from Saric & Thomas [43].

The transition from laminar to turbulent flow can be characterised using different indicators, including the skin-friction coefficient and the boundary layer thickness, as discussed by Vinuesa *et al.* [44]. In this study, the skin-friction coefficient is employed as an indicator. The behaviour of the skin-friction coefficient in zero-pressure gradient flows over a flat-plate has been extensively investigated in both numerical and experimental studies ([45],[46],[47],[37] and [48]). This parameter serves as a reliable indicator of the transition process, making it a subject of significant interest. All of the aforementioned studies consistently demonstrate a similar behaviour in the skin-friction coefficient for subcritical fluid flows, such as those of ideal gases. This coefficient decreases in the laminar regime following a reciprocal square root relationship with the Reynolds number until the onset of transition, which is relatively easy to detect as it is marked by a sudden increase. However, predicting the location is a more challenging task as it is dependent on the type of transition and the amplitude of disturbances. Throughout the transition phase, the skin-friction coefficient continues to rise, reaching a second maximum known as the overshoot skin-friction, before subsequently decreasing again within the fully turbulent region. The second indicator, the boundary-layer thickness exhibits a significant change when the flow undergoes transition, as depicted in Fig 1.1.

1.1.4 Unstable Mode II

The investigation into the influence of non-ideal gas effects in the transition process by Ren *et al.* [49] demonstrates the existence of a new unstable mode, referred to as Mode II, within a transcritical boundary layer. Specifically, their study focused on analysing the stability of the boundary layer in the proximity of the Widom line for supercritical fluids. The Widom line is a thermodynamic concept that enables to distinguish the different regions within the supercritical fluid, introduced by Fisher & Widom [50]. The initial findings of their studies reveal the stabilisation of subcritical or supercritical flows as a result of the growing influence of non-ideal gas effects close to the pseudo-critical temperature. Subcritical (resp. supercritical) flow refers to a flow where the temperature profile remains below (resp. above) the pseudo-critical temperature. Moreover, within the transcritical regime, where the temperature profile intersects the pseudo-critical line, they identified the presence of an additional

mode, denoted as Mode II, in addition to Mode I. Note that Mode I corresponds to the primary instability generating the TS waves in the flat-plate configuration. This additional unstable mode, solely present within a transcritical boundary layer, is depicted on the stability diagram in Fig 1.3. The coexistence of these two unstable modes highly destabilised the flow through the combined effects of both modes. In such a special case, the growth rate of Mode II can become one order of magnitude larger than that of the usual Mode I. This new unstable mode has been further analysed in the limit of zero Eckert number by Bugeat *et al.* [51] to rule out any possible acoustic origin. From an inviscid analysis, the existence of the Mode II resulting from a large gradient of dynamic viscosity coupled with a minimum of kinematic viscosity at the Widom line has been confirmed.
Wang [52] studied the possible secondary instabilities related to the new Mode II. This study revealed the existence of a possible $H-$type secondary instability, resulting from Mode II, in a transcritical flat-plate boundary layer. However, significant differences were observed in the amplitudes of higher harmonics due to nonlinear effects. These effects were negligible in a subcritical boundary layer but became significant in a transcritical boundary layer.

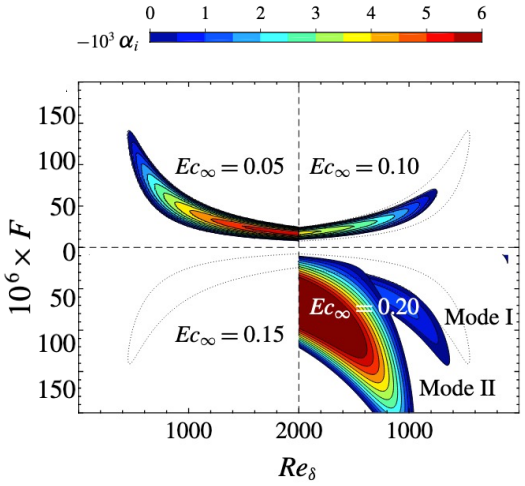

Figure 1.3: Growth rates of perturbations in the $F - Re_\delta$ stability diagram with subcritical free-stream temperatures: $T^*_\infty = 280$K for various Eckert numbers. Fig from Ren *et al.* [49].

1.1.5 Turbulent flow

The appearance of Λ-vortices indicates an increase in turbulence levels within the flow. These coherent structures exhibit a positive wall-normal velocity at the inlet of their legs and a negative velocity at the outlet, leading in the formation of a pair of streamwise vortices [53]. Consequently, these vortices generate regions characterised by high streamwise vorticity. Flow instability and the shear stress within the boundary layer cause the vortices to stretch and elongate, resulting in the formation of connections in the spanwise direction between the vortices. Eventually, these connections transform the $\Lambda-$vortices into Ω-shaped structures, as observed by Schmid & Henningson [54]. As the omega vortices become more prominent and flow instability intensifies, the vortices undergo a transition from organised to highly irregular and chaotic structures. This transformation leads to the breakdown of the organised vortical pattern, as discussed by Nishioka *et al.* [55], which results in the emergence of smaller-scale vortices and the onset of turbulent flow, characterised by rapid fluctuations and mixing. As the flow reaches a turbulent state, phenomena begin to occur at smaller length scales, referred as

the Kolmogorov's scales. As the Reynolds number increases, turbulence levels intensify, leading to smaller Kolmogorov length scales, observed by Kolmogorov [56].

1.2 Supercritical fluid

Every substance on Earth can be found in three different states: solid, liquid and gas. A phase transition, which leads to a change of state, occurs under specific temperature and pressure conditions. This transition is driven by the phase equilibrium, where the free energies of the phases are equal [57]. In Fig 1.4, the equilibrium between the solid and gaseous phases is represented by a red line. The green line indicates the separation between the liquid and solid phases, while the blue line represents the boundary between the liquid and gas phases. The temperature and pressure at the triple point, denoted by the subscript $(\cdot)_{tp}$, signify the conditions at which all the three phases coexist in a thermodynamic equilibrium [58]. This triple point is depicted as a red dot. The critical pressure and temperature, denoted by the subscript $(\cdot)_{cr}$, marks the boundary of this equilibrium region at the critical point, shown as a red light dot. Below this point, different phases can coexist,with distinct boundaries separating them. However, above the critical point, these phase boundaries disappear, resulting in a state of matter where there is no clear distinction between the liquid and gas phases. This phenomenon is attributed to the absence of surface tension, which means that no cohesive force between molecules at the fluid's interface exists [59]. This state corresponds to a supercritical fluid (SCF).

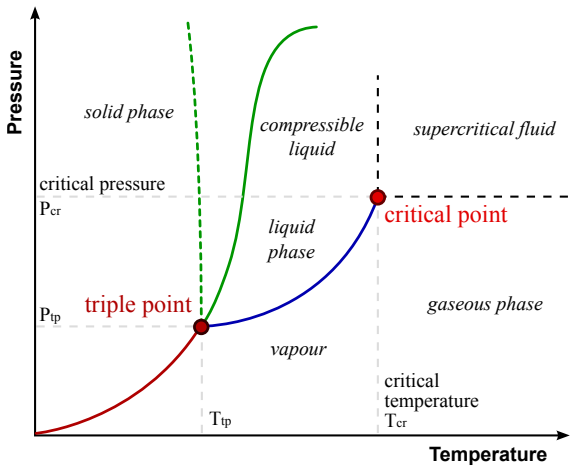

Figure 1.4: The liquid-vapor critical point is depicted on the pressure-temperature phase diagram. The solid green line represents the typical shape of the phase boundary between the liquid and solid phases. The dotted green line represents the specific case with water [60].

The behaviour of SCFs is exemplified by Supercritical Carbon dioxide ($scCO_2$), which possesses the following critical properties taken from the reference fluid thermodynamic properties database REFPROP [61],

$$T_{cr} = 304.1 \text{ K} \qquad P_{cr} = 7.38 \text{ MPa}.$$

The interest of supercritical fluids is the presence of substantial deviations from normal behaviour near the critical point. Therefore, by varying the pressure and the temperature, the thermodynamic properties of the fluid can be adjusted depending on the intended use of the fluid. Fisher & Widom predicted the presence a peak in the specific heat C_p at the Widom line and called it, the pseudo-critical point. This maximum was observed experimentally by Jones *et al.* [62]. This steep change of properties is due to a liquid-like state below the critical point and a vapour-like state above.

To quantify the deviation from ideal gas in SCFs, the compressibility factor Z, is introduced in the ideal-gas law. The value of Z, which is the ratio of pressure to the product of density, gas constant, and temperature, indicates the degree of non-ideal gas effects. A smaller value of Z corresponds to a greater presence of non-ideal gas behaviour, while $Z = 1$ signifies an ideal-gas. Fig 1.5 represents the $T - v$ diagram of CO_2 at a supercritical pressure of $P_r = 1.08$ and shows the compressibility factor in different regions. The subscript $\cdot_r$ denotes the reduced quantities, where each quantity is normalised by its corresponding critical value. Non-ideal effects are strongly present in the vicinity of the Widom line (represented by red stars), where Z decreases below 0.5. The Van der Waals equation of state is preferred for modelling the physics of supercritical fluids due to its simplicity and computational efficiency, surpassing alternative models.

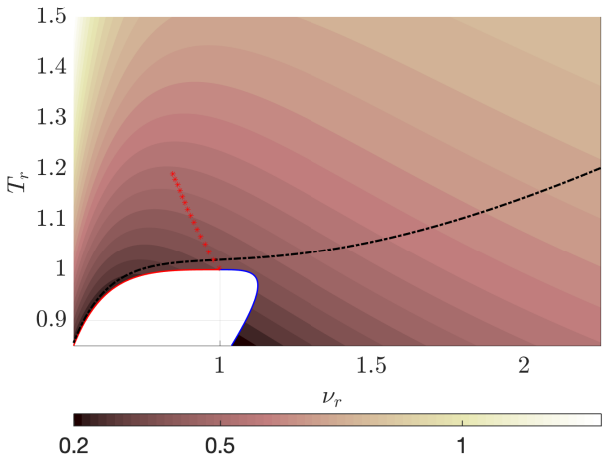

Figure 1.5: $T - v$ diagram of CO_2 using the Van der Waals equation of state, along with the Widom line (red starred line), two saturation curves (blue and red lines) and an isobar of $P_r = 1.08$ (black line). The shaded area represents the contour of the compressibility factor Z, indicating the degree of non-ideality.

The use of supercritical fluids in an industrial processes has been experienced significant growth in recent years. This has been driven by the growing interest in the development of new technologies that minimise the environmental impact by reducing the energy consumption. The unique combination of gas-like viscosity and liquid-like density makes SCF an excellent solvent for mass transfer processes ([10],[63] and [64]). The application of supercritical fluids in energy generation appeared in 1957 with the world's first commercial supercritical steam-electric generating unit called Philo 6 [65]. This innovation led to a major breakthrough in the energetic sector as it significantly advanced the thermal efficiency of power generation and thus decreasing the production costs. At that time, the average efficiency of the fossil-fuelled power plants was about 30%. The introduction of a steam at supercritical pressure and temperature led to a new level of thermal efficiency approaching 40%. Three years later, a second supercritical pressure unit, larger and more efficient, called Eddystone [66], entered the commercial service in the U.S. in 1960. Supercritical plants that are built nowadays are based on Eddystone. In 2013, the first U.S. ultrasupercritical power plant in operation born with a power of 600 MW. In 2019, more than 400 supercritical steam power plants were operational in the USA, Russia and Europe [67].
Moreover, the use of SCF encompasses the objective of improving the efficiency of gas turbines. Specifically, the use of supercritical CO_2 as a working fluid is driven by its combination of high density similar to that of a liquid while retaining the ability to fill containers like a gas [68]. Furthermore, its potential as a supercritical fluid to reduce greenhouse gas emissions, thanks to its low global warming

potential [69] combined with its moderate critical temperature and pressure, which make it easy to contain and safe to handle [70], establish $scCO_2$ as an optimal choice. The work of Sengupta *et al.* [13] reveals that emplying $scCO_2$ in a closed Brayton cycle enables to reach higher conversion efficiency. The higher density of $scCO_2$ compared to traditional gases, along with the nearly constant density during compression, requires a smaller volume change to achieve the desired pressure. This results in a lower compression ratio and, therefore relatively high compressor efficiency [71]. In addition, various works (Keller *et al.* [72] and Samini *et al.* [73]) have demonstrated that the compactness of SCFs makes them well suited for applications with spatial constraints, such as micro-gas turbines or portable power systems. SCFs have also been implemented in the Brayton cycle of nuclear power plants to achieve efficiencies higher than 50% [74]. Finally, this fluid has also been incorporated into the field of solar energy as a working fluid in Rankine cycle systems, aiming to increase overall efficiency [75]. The inherent flexibility of SCFs with respect to their operating temperature and pressure ranges allows for adaptation to both high-temperature and low-temperature heat sources, thus expanding their potential applications [76]. In summary, the incorporation of $scCO_2$ in power cycles contributes to improved energy efficiency and performances.

1.3 Objectives

The objective of this thesis is to investigate the transition process and turbulent statistics of a transcritical boundary layer along a flat-plate. To achieve this, the fluid will be introduced at a supercritical pressure and subcritical temperature. The wall temperature will be maintained isothermal and set higher than the critical temperature to ensure that the flow temperature varies across the pseudo-critical temperature, thus creating a transcritical boundary layer. Direct Numerical Simulations will be employed to observe the breakdown phenomenon resulting from the unstable Mode II discovered in these configurations, allowing the extrapolation of the findings to various industrial applications involving supercritical fluids over surfaces. The understanding of the H-type transition caused by the secondary instability of subharmonic oblique waves will be achieved through modal analysis, involving the observation of growth and interactions of different eigenmodes. The unique properties of supercritical fluids necessitate a careful analysis to determine the optimal numerical parameters that ensure simulations free from numerical errors. Once these parameters have been determined, the influence of various flow parameters such as pressure or Mach number will be varied to assess their impact on the breakdown process and turbulent statistics.

1.4 Thesis outline

Chapter 1 provides a theoretical review of the transition from laminar to turbulent flow and the characteristics of supercritical fluids. Chapter 2 introduces to the governing equations and the non-dimensionalisation used in this study, along with an explanation of the numerical methods employed to solve these equations. A detailed description of the post-processing techniques is also presented. Chapter 3 conducts simulations using the ideal-gas law to validate the post-processing tools and introduce the turbulent statistics. Numerical simulations employing a real equation of state are carried out in Chapter 4. This section includes a parameter analysis study aimed at evaluating the influence of various numerical parameters. It also addresses specific numerical issues, and their proposed resolutions will be discussed. After reducing the numerical errors to a negligible level, Chapter 5 analyse the influence of the free-stream pressure, Mach number, and wall temperature on the transition process and the resulting turbulent statistics.

Chapter 2

Governing equations and numerical approaches

In this section, several theoretical aspects related to the governing Navier-Stokes equations and the equation of state used to accurately model the non-ideal gas effects are introduced. Secondly, a detailed explanation of the numerical setup is provided, outlining the specific parameters and variables considered in the direct numerical simulations. This includes informations about the computational grid used, its resolution, and the numerical schemes implemented. Furthermore, the boundary conditions imposed on the right-hand side of the Navier-Stokes equations are presented. Lastly, a comprehensive discussion is provided regarding the computed initial conditions that define the initial state of the fluid prior to the simulation.

2.1 Governing equations

The Navier-Stokes Equations (NSE) provide a mathematical description of the motion of viscous fluids. In their non-dimensional form, the Navier-Stokes equations can be expressed as a set of differential equations that govern the conservation of mass, momentum, and energy as follows

$$\frac{\partial \rho}{\partial t} + \frac{\partial \left(\rho u_j\right)}{\partial x_j} = 0, \tag{2.1.1}$$

$$\frac{\partial \left(\rho u_i\right)}{\partial t} + \frac{\partial \left(\rho u_i u_j + p\delta_{ij} - \tau_{ij}\right)}{\partial x_j} = F_i, \tag{2.1.2}$$

$$\frac{\partial (\rho E)}{\partial t} + \frac{\partial \left(\rho E u_j + p u_j + q_j - u_i \tau_{ij}\right)}{\partial x_j} = u_j F_j, \tag{2.1.3}$$

where:

- $x_i = (x, y, z)$ being the coordinates, respectively, in the streamwise, in the wall-normal and the spanwise direction;
- $u_i = (u, v, w)$ being the velocity components, respectively, in the streamwise, in the wall-normal and the spanwise direction;
- t being the time;
- ρ being the fluid density;

- $E = e + u_i u_i/2$ and e, respectively, the total and the internal energy;
- F_i being the body force which is set to $\mathbf{0}$ since the effects of gravity on the development of a boundary layer over a flat-plate can be neglected [77];
- p being the pressure.

The viscous stress tensor τ_{ij}, and the heat flux, q_j, are given by

$$\tau_{ij} = \frac{\mu}{Re}\left(\frac{\partial u_i}{\partial x_j} + \frac{\partial u_j}{\partial x_i}\right) + \frac{\lambda}{Re}\delta_{ij}\frac{\partial u_k}{\partial x_k}, \qquad q_j = -\frac{\kappa}{\mathrm{RePrEc}}\frac{\partial T}{\partial x_j}, \tag{2.1.4}$$

where:

- μ being the dynamic viscosity;
- $\lambda = \mu_b - 2/3\mu$ being the second viscosity;
- μ_b being the bulk viscosity;
- κ being the thermal conductivity.

Dimensionless quantities

Non-dimensional values and equations are preferred due to their simplicity and generalised form. By converting dimensional quantities into non-dimensional ones, the mathematical formulations are simplified and become more manageable for analysis and computations. To achieve this non-dimensionalisation, various reference values are employed to scale the dimensional quantities, those are

$$u = \frac{u^*}{u^*_\infty},\ x_i = \frac{x^*_i}{l^*_0},\ t = \frac{t^* u^*_\infty}{l^*_0},\ p = \frac{p^*}{\rho^*_\infty u^{*2}_\infty},\ \rho = \frac{\rho^*}{\rho^*_\infty} \tag{2.1.5}$$

$$T = \frac{T^*}{T^*_\infty},\ E = \frac{E^*}{u^{*2}_\infty},\ \mu = \frac{\mu^*}{\mu^*_\infty},\ \kappa = \frac{\kappa^*}{\kappa^*_\infty}. \tag{2.1.6}$$

The superscript $\cdot^*$ refers to the dimensional values, while the subscript $\cdot_\infty$ refers to the free-stream values. The dimensional length scale is represented by l^*_0. The dimensionless parameters characterising flow conditions are introduced. Firstly, the Reynolds, Re and the Prandtl, Pr number are defined as

$$Re = \frac{\rho^*_\infty u^*_\infty l^*_o}{\mu^*_\infty}, \qquad Pr = \frac{c^*_{p,\infty}\mu^*_\infty}{\kappa^*_\infty}, \tag{2.1.7}$$

where $c^*_{p,\infty}$ being the specific heat capacity. The first dimensionless parameters relates the ratio between the inertial and viscous forces while the Prandtl number reflects the ratio between the thermal and the velocity boundary layer [78].

The reference length, l^*_0 is chosen to correspond to the Blasius length scale δ^*, which refers to the boundary layer thickness as

$$\delta^* = \sqrt{\frac{\mu^*_\infty x^*}{u^*_\infty \rho^*_\infty}}.$$

The related Reynolds numbers based on the Blasius length and the relation with the one based on the non-dimensional streamwise position, x^* are

$$Re_{\delta(x)} = \frac{\rho^*_\infty u^*_\infty \delta(x)^*}{\mu^*_\infty} \qquad Re_x = \frac{\rho^*_\infty u^*_\infty x^*}{\mu^*_\infty} = Re^2_{\delta(x)}.$$

Similarly, the 99$^{\text{th}}$ boundary layer thickness, denoted as $\delta^{99}(x)$, is defined as the distance from the wall at which the boundary layer extends to a location where the boundary layer thickness reaches 99% of its maximum value.
Secondly, the dimensionless numbers that provide an overview of the compressibility of the fluid are the Mach number, M and the Eckert number, Ec as

$$M = \frac{u^*_\infty}{a^*_\infty}, \qquad Ec = \frac{(u^*_\infty)^2}{c^*_{p,\infty} T^*_\infty}, \tag{2.1.8}$$

related by

$$Ec = M^2 \frac{(a^*_\infty)^2}{c^*_{p,\infty} T^*_\infty}, \tag{2.1.9}$$

where a^*_∞ being the speed of sound.

It is common to neglect the compressibility effects for Mach numbers lower than 0.3 [78]. The Eckert number expresses the relationship between the advective mass transfer and the heat dissipation potential. It characterises the heat dissipation through viscosity in high-speed flows. When these numbers are large, acoustic effects come into play. In this work, the aim is to rule out any compressibility or acoustic effect. For this purpose, both dimensionless numbers must be decreased. Nevertheless, the significant change in thermodynamic properties near the critical point causes the speed of sound to exhibit a large gradient in this area. Different works ([49] and [79]) reveal that the compressibility effects present in this region are not accurately quantified by fixing the Mach number. Therefore, it is preferable to impose a low Eckert number and calculate the resulting Mach number.

Equation of state

To accurately model the behaviour of the fluid and to close the NSE, an additional equation, the Equation of State (EoS), must be added into the NSE. This law establishes a relationship between pressure, temperature, and density of the fluid, thereby accounting for the effects of compressibility and variations in fluid properties. Among the numerous existing models, this work employs

- Ideal-gas model, (IG):
  The ideal-gas concept obeys a simplified equation of state as

  $$p^* = \rho^* R_g T^* \tag{2.1.10}$$

  where R_g being the specific gas constant. This law assumes that the particles composing the gas do not interact [80]. Nevertheless, at high temperatures or low pressures, the intermolecular forces between gas molecules become less significant as the average distance between molecules increases. This allows many real gases, including CO_2, to exhibit behaviour that is qualitatively similar to that of an ideal gas [81]. Given its simplicity, this model is widely used. The transport properties, μ and κ are calculated using Sutherland's law [82], where both properties are function of the temperature. Those are:

  $$\frac{\mu}{\mu_0} = \left(\frac{T}{T_0}\right)^{3/2} \frac{T_0 + S_\mu}{T + S_\mu}, \tag{2.1.11}$$

  $$\frac{\kappa}{\kappa_0} = \left(\frac{T}{T_0}\right)^{3/2} \frac{T_0 + S_\kappa}{T + S_\kappa}. \tag{2.1.12}$$

  The Sutherland's law coefficients and the different constants in Eqs (2.1.10) taken from REFPROP [61] are shown in the Appendix A in Tab A.1.

- Van der Waals law, (VdW):
  The low value of the compressibility factor given in Fig 1.5 reveals the presence of strong non-ideal effects near the pseudo-critical line. To include the interaction between particles, a more sophisticated model is thus required such that the behaviour of the fluid is better represented in those specific regions. The cubic relation for the VdW equations taken from the work of Brunner [83] and Zappoli *et al.* [84] has been non-dimensionalised using the critical parameter T_r, p_r and ν_r defines as

$$T_r = \frac{T^*}{T_c^*}, \quad p_r = \frac{p^*}{p_c^*}, \quad \nu_r = \frac{\nu^*}{\nu_c^*}. \tag{2.1.13}$$

  The derivation of the Van der Waals equation in reduced form is provided in the Appendix A and gives

$$T_r = \frac{1}{8}\left(3v_r - 1\right)\left[p_r + \frac{3}{v_r^2}\right], \quad Z_c = \frac{p_r^* \nu_r^*}{T_r^* R^*} = \frac{3}{8}, \quad a_r = 3, \quad b_r = \frac{1}{3}, \quad \text{and} \quad R_r = \frac{1}{Z_c}, \tag{2.1.14}$$

  where Z_c, a_r and b_r being the universal compressibility factor and two constants, respectively. The reduced equations eliminates the dependence on substance-specific quantities and make them independent of the particular characteristics of the substance. This universality enables generalisations since it allows for the analysis of fluid behaviour across different substances using the same reduced equations. However, it should be noted that the compressibility factor predicted by the VdW EoS tends to overestimate the observed values found in many gases, where the critical compressibility factor Z_c is typically around 0.28 [85] at the critical point. Despite its usefulness in qualitatively discussing gas properties, those equations do not accurately reproduce the experimentally observed critical compression factor. Regarding the dynamic viscosity and thermal conductivity, the JST model developed by Jossi, Stiel and Thodos [86] is applied.

The variation of different thermodynamic and transport properties of supercritical CO_2, using the ideal-gas law, Van der Waals EoS and REFPROP tables [61] is shown in Fig 2.1. The REFPROP model incorporates extensive thermodynamic and transport property databases compiled from experimental measurements and theoretical models, making it the most accurate model. In the vicinity of the pseudo-critical line, all properties exhibit a large gradient, except of an ideal gas. The peak in amplitude of the specific heat, given in Fig 2.1(b), corresponds to the pseudo-critical point. Other models, such as Peng-Robinson or Redlich-Kwong (not shown here), provide significantlt different amplitude estimations, particularly in determining the peak amplitude and the temperature at which it occurs. Likewise, all models provide different estimates for the density variation in the liquid-like region. Using an ideal-gas model is inappropriate due to the highly non-ideal behaviour of the fluid in the temperature range depicted in Fig 1.5. This highlights the importance of using a real gas EoS when dealing with supercritical fluids.

It is important to acknowledge that the Van der Waals equation of state, for thermodynamic conditions close to the critical point, exhibits a violation of the stability law in thermodynamics [87], which states that pressure P should not increase with volume V. To address this nonphysical behaviour, the Maxwell construction method is employed by connecting the two points corresponding to the coexisting phases (gas and liquid) with a horizontal line on the graph, referred to the Maxwell line (depicted as a dotted line in Fig 2.2). The region below the Maxwell line represents the dissipated heat energy during the phase transition, while the region above it corresponds to the energy used for performing work [88]. The construction of the Maxwell line ensures that the area enclosed between the isotherm curve and the Maxwell line is equal to the area enclosed by the isotherm curve alone.

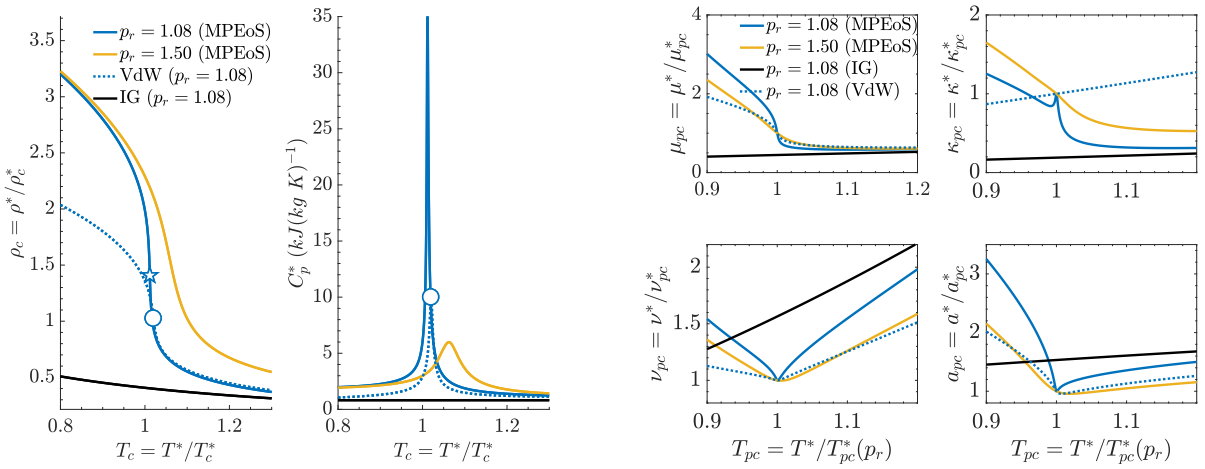

(a) ρ_c and C_p^*.

(b) $\mu_{pc}; \kappa_{pc}; \nu_{pc}$ and a_{pc}.

Figure 2.1: Thermodynamic and transport properties of $C0_2$ at $p_r = 1.08$ and $p_r = 1.5$ using different fluid models. The MPEoS represents REFPROP using the multi-parameters fluid mode, VdW represents the Van der Waals model, and IG represents an ideal gas model. The distributions of (a) density ρ and heat capacity at constant pressure C_p, and (b) viscosity μ_{pc}, thermal conductivity κ_{pc}, kinematic viscosity ν_{pc}, and speed of sound a_{pc} are plotted against the pseudo-critical temperature T_{pc}. The pentagram denotes the pseudo-critical temperature T_{pc} in the REFPROP model.

Fig 2.2(a) illustrates the $(P_r - \nu_r)$ diagram coloured by the reduced pressure. Through the correction of the Van der Waals equation of state, an increase in temperature leads to an increase in pressure or specific volume.

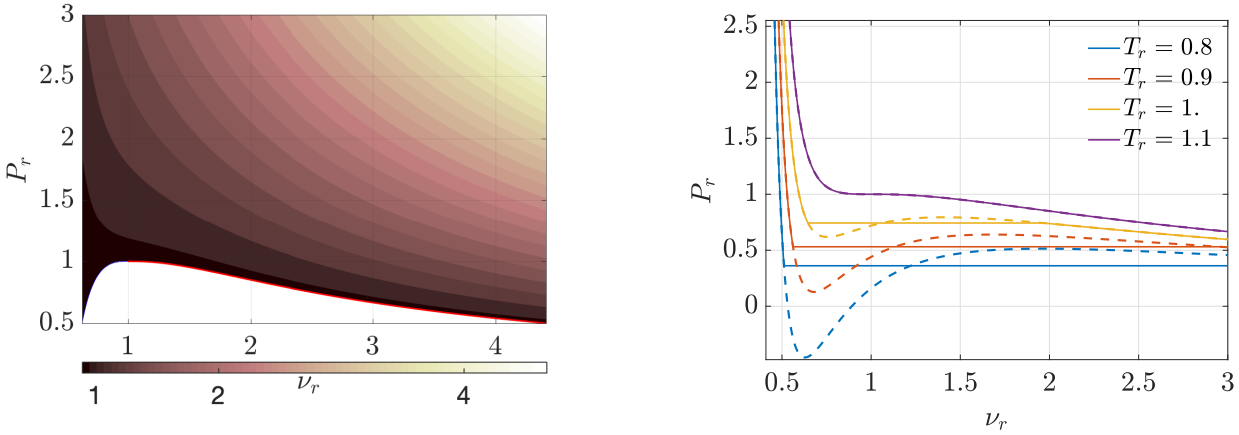

(a) Contour of T_r.

(b) Maxwell construction.

Figure 2.2: $(P_r - \nu_r)$ diagram of CO_2 using the Van der Waals equation of state contoured by the reduced temperature T_r. In (b), the $(P_r - \nu_r)$ diagram showcases various isotherms, with the use of the Maxwell construction depicted as dotted lines and without its application depicted as solid lines.

2.2 Numerical setup

The preceding NSE, coupled with the EoS form a system of nonlinear equations that must be solved numerically. The most commonly used method in industry, called the Reynolds Averaged Navier-Stokes (RANS), solves the averaged NSE equation. The simplifications employed in this method render RANS unsuitable for the study of the transition [89]. A second method, called the Large-Eddy Simulation (LES) resolves the largest turbulent scale that contains the energy while the smallest ones are modelled [90]. This method remains inadequate to study the transition as it does not solve the near-wall region with the smallest length scales. The final method, called the Direct-Numerical simulation (DNS) is the one used in this work: it refers to higher-fidelity techniques that directly solve the governing Navier–Stokes equations without any turbulence models. DNS is a highly suitable tool for studying breakdown phenomena as it resolves the entire range of flow scales, including the physics occurring at small length scales, without any assumptions or simplifications. However, since all the turbulent structures are resolved, it requires a very expensive computational cost such that only simple configurations, as a flat-plate, can be simulated. Additionally, the similarity to the experimental facilities allows for the analysis and comparison of the transition process with experimental results.

2.3 Computational domain

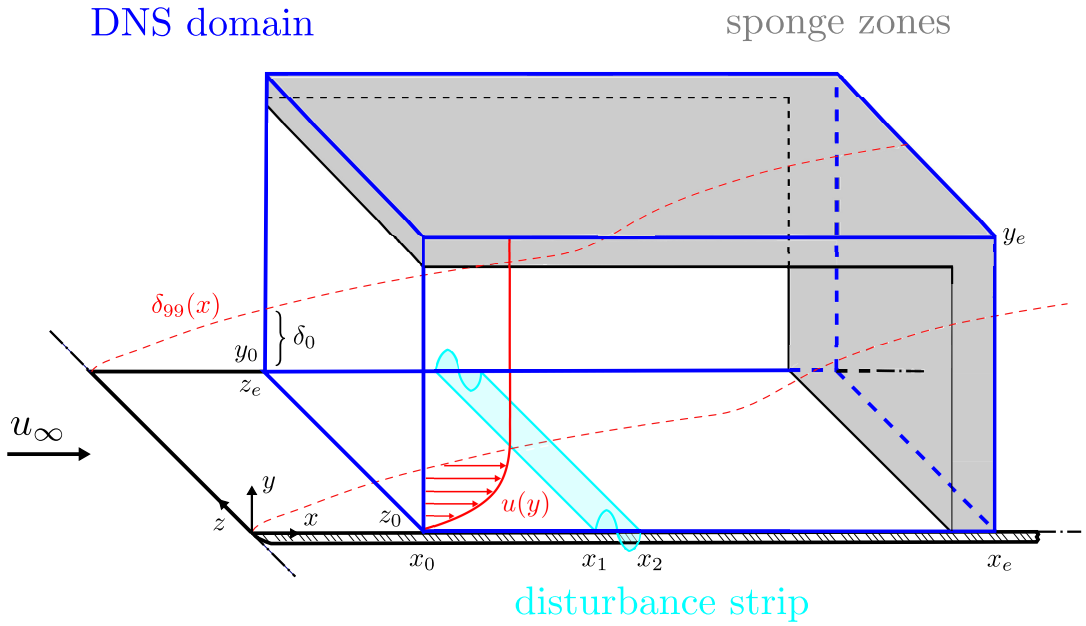

Figure 2.3: Representation of the three-dimensional computational domain that will be used for the DNS. The light blue colour indicates the presence of the sponge zone, while the red line represents the disturbance strip. A sponge zone is also positioned at the inlet but not depicted in the figure for simplification.

For this study, an in-house DNS code written in *modern Fortran* while the FFT and the results will be post-processed on *modern Fortran* and *Matlab*. Fig 2.3 represents the computational domain with:

- x_0 and x_e being the initial and final positions along the streamwise direction, respectively;
- y_0 and y_e being the initial and final positions along the wall-normal direction, respectively;

- z_0 and z_e being the initial and final positions along the spanwise direction, respectively;
- $L_x = x_e - x_0$ being the length along the streamwise direction;
- $L_y = y_e - y_0$ being the length along the wall-normal direction;
- $L_z = z_e - z_0$ being the length along the spanwise direction.

The starting point of the computational domain is attributed to a unit boundary layer thickness, denoted as $\delta_0^{\mathrm{DNS}} = 1$, as the flow at low Reynolds numbers is not the focus of this study. Moreover, the abrupt changes in flow conditions near the starting point due to the no-slip condition can potentially introduce artificial disturbances or spurious oscillations. Hence, this specific region has been excluded. The spanwise and wall-normal lengths are prescribed, while the streamwise is computed.

In order to trigger the transition, disturbances will be introduced within the laminar boundary layer by means of a blowing/suction wave along a disturbance strip whith a length of $l_{pt} = x_2 - x_1$. Additionally, different sponge areas are introduced at the inlet (not present in Fig 2.3), the outlet and the top boundary to effectively absorb outgoing waves and minimise their reflection. Their implementation is discussed in Sec 2.3.3.

2.3.1 Mesh generation

The number of grid points in each direction of space is, denoted with n_x, n_y and n_z. The wall-normal distribution is prescribed using a hyperbolic tangent to correctly capture the boundary layer near the wall. The distribution is

$$y(i) = L_y * \left[C \cdot \eta + (1 - C) \cdot \left(1 + \frac{\tanh\left(S_f(\eta - 1)/2\right)}{\tanh\left(0.5 S_f\right)} \right) \right] \tag{2.3.1}$$

with

$$\eta(i) = \frac{i-1}{n_y - 1}, \quad C = \frac{0.8}{Re_\tau} \frac{n_y - 1}{L_y}, \quad Re_\tau = \delta\left(x_{\text{start}}\right) \sqrt{\frac{\rho_{\text{wall}}}{\mu_{\text{wall}}} \frac{dU}{dy}}. \tag{2.3.2}$$

The stretching factor, S_f, is used to modify the grid distribution and can be adjusted to increase the number of points in the near-wall region. The streamwise distribution will be adjusted, alternating between equidistant and non-equidistant grid spacing when necessary. The non-equidistant grid spacing allows for a reduction in grid spacing along the disturbance strip and in the turbulent region, where physics occur at small scale, without affecting the grid spacing in the laminar region. To achieve this, a new computational streamwise coordinate, ξ, is introduced, and the streamwise distribution is calculated as follows

$$\begin{aligned} z(\xi) = {} & 0.5\delta_1 \left(z_{pt}^+ - z_{\max}^+\right) \log\left[\cosh\left(\tfrac{z_1 - \xi}{\delta_1}\right)\right] + 0.5\delta_2 \left(z_{\max}^+ - z_{pt}^+\right) \log\left[\cosh\left(\tfrac{z_2 - \xi}{\delta_2}\right)\right] \\ & 0.5\delta_3 \left(z_{\min}^+ - z_{\max}^+\right) \log\left[\cosh\left(\tfrac{z_3 - \xi}{\delta_3}\right)\right] + 0.5\delta_4 \left(z_{\max}^+ - z_{\min}^+\right) \log\left[\cosh\left(\tfrac{z_4 - \xi}{\delta_4}\right)\right] + z_{\max}^+ \xi - C \end{aligned}$$

with

$$\begin{aligned} C = {} & 0.5\delta_1 \left(z_{pt}^+ - z_{\max}^+\right) \log\left[\cosh\left(\tfrac{z_1}{\delta_1}\right)\right] + 0.5\delta_2 \left(z_{\max}^+ - z_{pt}^+\right) \log\left[\cosh\left(\tfrac{z_2}{\delta_2}\right)\right] \\ & + 0.5\delta_3 \left(z_{\min}^+ - z_{\max}^+\right) \log\left[\cosh\left(\tfrac{z_3}{\delta_3}\right)\right] + 0.5\delta_4 \left(z_{\max}^+ - z_{\min}^+\right) \log\left[\cosh\left(\tfrac{z_4}{\delta_4}\right)\right] \end{aligned} \tag{2.3.3}$$

$$z^+ = z Re_\tau, \quad Re_\tau = u_\tau \frac{\rho_w}{\mu_w}, \quad u_\tau = \sqrt{\frac{\tau_{xz}}{\rho_w}},$$

with z_{pt}^{+} being the value inside the disturbance strip, z_{min}^{+} in the turbulent region and z_{max}^{+} in the laminar region. The parameters z_1, z_2, z_3 and z_4 are

$$z_1 = f(\text{start of the disturbance strip}),\ z_2 = f(\text{end of the disturbance strip}),$$

$$z_3 = f(\text{start of the turbulent region}),\ z_4 = f(\text{end of the turbulent region})$$

and $\delta_i = z_i w_i$, with w_i the width of the i^{th} transition bumps.

Finally, the spanwise distribution is maintained equidistant throughout this study.

2.3.2 Numerical scheme

To obtain high-fidelity results, it is important to minimise both dissipation and dispersion errors through the appropriate selection of numerical schemes. The use of high-order numerical scheme helps to decrease this dispersion errors [91]. Therefore, in this work, a sixth-order finite difference scheme is employed for the first-order derivatives, and a fourth-order scheme is used for the second-order derivatives. However, reducing the dissipation errors is more challenging. Some existing methods, used in this work, prevent any dispersion errors but potentially induces numerical instability [92]. To enhance numerical stability, Coppola *et al.* [93] revealed the necessity to use numerical schemes for both primary and secondary quantities. The primary quantities refer to the mass, momentum and total energy, while the secondary refers to the kinetic energy and entropy.

The numerical scheme employed in this study for the advection terms is the kinetic energy and entropy preserving (KEEP). The KEEP scheme ensure excellent entropy preservation, which enhances the numerical stability. The non-strictly entropy preservation comes from the fact that the entropy equation is not directly solved. Furthermore, these schemes exhibit improved numerical robustness compared to existing kinetic energy preservation schemes (KEP) of Jameson [94] or Pirozzoli [95]. The KEEP scheme developed by Kuya and Kawai [96] is preferred in this work due to its ability to satisfy analytical relations at the discrete level, which is crucial for accurately solving the energy exchange ([97] and [98]). The discrete pressure-evolution equation for the KEEP scheme is computed based on the internal energy equation (written using second-order spatial scheme for simplicity) as follows

$$\left.\frac{\partial \rho e}{\partial t}\right|_{(m)} + \frac{\left.\tilde{I}\right|_{(m+\frac{1}{2})} - \left.\tilde{I}\right|_{(m-\frac{1}{2})}}{\Delta x} + p|_{(m)}\,\frac{u|_{(m+1)} - u|_{(m-1)}}{2\Delta x} = 0 \tag{2.3.4}$$

where m denotes the cell index and $\tilde{I}$ refers to the internal energy flux

$$\tilde{I}_j|_{(m\pm\frac{1}{2})} = \frac{\rho|_{(m\pm1)} + \rho|_{(m)}}{2}\,\frac{e|_{(m\pm1)} + e|_{(m)}}{2}\,\frac{u_j|_{(m\pm1)} + u_j|_{(m)}}{2} \tag{2.3.5}$$

Using the simple ideal-gas relation $\rho e = p/(\gamma - 1)$ into the discrete internal-energy equation and assuming a constant pressure and velocity distribution, it becomes possible to compute the pressure-evolution equation as follows

$$\left.\frac{\partial p}{\partial t}\right|_{(m)} = -\frac{\frac{\rho|_{(m+1)}+\rho|_{(m)}}{2}\frac{u|_{(m+1)}+u|_{(m)}}{2}\frac{(p/\rho)|_{(m+1)}+(p/\rho)|_{(m)}}{2} - \frac{\rho|_{(m-1)}+\rho|_{(m)}}{2}\frac{u|_{(m-1)}+u|_{(m)}}{2}\frac{(p/\rho)|_{(m-1)}+(p/\rho)|_{(m)}}{2}}{\Delta x}$$
$$- (\gamma-1)p|_{(m)}\,\frac{u|_{(m+1)} - u|_{(m-1)}}{2\Delta x} \neq 0.$$

The pressure equilibrium is thus not discretely satisfied as the latter equation does not cancel out. The absence of pressure equilibrium using from this simple law implies the lack of equilibrium when employing the VdW EoS. Several studies ([99], [17] and [100]) revealed the absence of pressure equilibrium at interfaces,leading to spurious pressure oscillations that spread the physics of the flow. A special attention should, thus, be paid to the analysis of the pressure field. Additional information regarding the pressure-evolution equation is given in Shima's [18] work.
In terms of temporal integration, this code employs a third-order Runge-Kutta scheme. This scheme is chosen for its favourable stability properties, which allow for the use of larger time steps, denoted Δt, compared to lower-order schemes [101]. Throughout the simulation, the Courant–Friedrichs–Lewy (CFL) number remains constant.

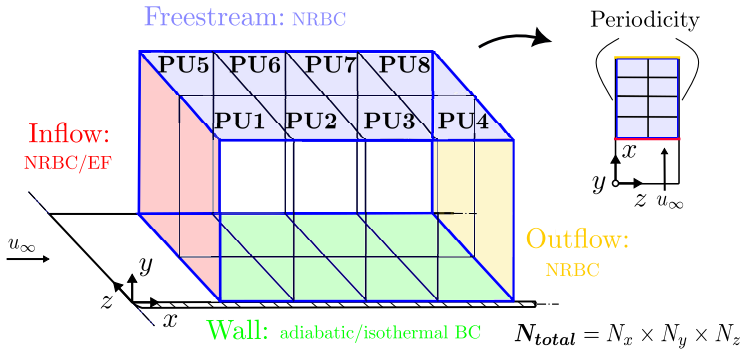

Figure 2.4: The computational domain is discretised into power units (PU) in the streamwise and spanwise directions

The computational domain is partitioned into multiple processing units (PUs) in both the streamwise and spanwise directions, as illustrated in Fig 2.4. The code incorporates the use of Message Passing Interface (MPI) to take advantage of the available computing resources. MPI enables communication and data exchange among multiple processors, allowing for parallelisation of the computation.

2.3.3 Boundary conditions

Boundary conditions (BC) are required at the different edges of the domain to correctly simulate the desired type of flow. BCs play a crucial role in defining the interaction between the fluid and its surroundings and preventing wave reflections. The boundary conditions presented in Tab 2.1 have been chosen based on the work of Poinsot & Pope [102], where they revealed the importance of generating inflow profiles that correspond to the desired flow characteristics.

Boundary	Inlet	Outlet + Top	Wall	Spanwise boundaries
Inviscid condition	$\mathbf{u} \neq \mathbf{0}$ $\rho = \rho_\infty$	$P = P_\infty$	$\mathbf{u} = \mathbf{0}$ $T = T_w$	Periodic
Viscous condition	$\partial\tau_{xx}/\partial x = 0$	$\partial\tau_{xy}/\partial x = 0$ $\partial\tau_{xz}/\partial x = 0$ $\partial q_x/\partial x = 0$	/	/

Table 2.1: The different boundary conditions applied at each boundary of the domain to solve the Direct Numerical Simulation for a viscous flow.

The characteristic wave boundary condition for non-ideal gas [102] is employed to impose the different BC. This method simulates the behaviour of waves propagating through the flow, accurately capturing the wave characteristics at the boundaries, including both incoming and outgoing waves. This method is particularly favoured in DNS as it ensures accurate and realistic simulations by capturing the essential dynamics between waves and boundaries. To accurately represent the flow behaviour at the boundaries, the convective terms of the NSE are computed using the wave method based on the work of Okongo & Bellan [103], which evaluates the convective terms, considering the effects of wave propagation and fluid advection. The computation of characteristic waves involves determining their amplitudes, denoted as $\mathcal{L}$, and their associated characteristic velocities, denoted as λ. Subsequently, the conservative variables, including density, momentum, and energy, are computed. The amplitudes of the incoming waves, $\mathcal{L}$, are determined using the Local One-Dimensional Inviscid (LODI) relations. These relations allows for estimating the amplitude variations by analysing a locally associated one-dimensional inviscid problem [102]. The one-dimensional and inviscid flow assumption, used in the LODI relations, provide an estimate of the variations in incoming wave amplitudes. The present work involves a subsonic flow throughout the entire computational domain, ensuring that both the inlet and outlet regions maintain a subsonic nature. As a result, only one characteristic enters the domain exclusively through the outlet, while all other characteristics enter solely through the inlet.

Furthermore, the unsteadiness of the simulation generates vortices and acoustic waves that propagates through the domain. The capacity to let those waves leave the domain without causing non-physical reflections is crucial to ensure high-quality results as explained by Hirsch [104]. To address this, non-reflecting boundary conditions, from the work of Thompson (1987) [105], are implemented. The study conducted by Christofi [106], demonstrates that the non-reflecting BC implemented in a $2D$ simulation can effectively reduce those spurious reflections. Non-reflective boundary conditions are implemented on all boundaries of the domain except in the spanwise direction. Distinct values are assigned to each boundary:

- Inlet:
  At the subsonic inlet, four characteristic waves enter the domain, necessitating the imposition of four inviscid boundary conditions. Those are the density ρ and the three components on the velocity vector u, v and w. The density and velocity profiles are prescribed from a laminar boundary-layer solution, which serves to prescribe the initial condition in Sec 2.3.4. In addition, the viscous condition imposing that the normal stress in the x direction has zero spatial derivative $\partial\tau_{xx}/\partial x = 0$ is required to consider the viscosity of the fluid.

- Isothermal flat-plate:
  An isothermal flat-plate is modelled by imposing the no slip condition $u_i = 0$ and a constant wall temperature $T(y = 0) = T_w$.

- Outlet and top:
  The same parameters are imposed on these boundaries because they correspond to locations where the flow exits the domain. Unlike the inlet, only one wave enters through the domain, so one inviscid boundary condition is required. Imposing the static pressure to be equal to the free-stream pressure is sufficient as an inviscid condition. To account for the viscosity, the tangential and the normal stresses τ_{xy} and τ_{xz} as well as the normal heat flux q_x are imposed to have zero spatial derivatives along the x direction. The amplitude of the incoming wave, $\mathcal{L}$, is computed from the prescribed free-stream pressure as follows

$$\mathcal{L} = \mathcal{K}(p - p_\infty), \tag{2.3.6}$$

$$\mathcal{K} = \sigma_{BC}\frac{(1 - Ma_\infty^2) \cdot c}{L}, \tag{2.3.7}$$

where $\mathcal{K}$ and σ_{BC} are constants, and L represents the length of the domain in the direction normal to the boundary. At the outlet, a perfectly non-reflecting boundary condition is achieved by setting σ_{BC} to zero. This condition ensures that the amplitude of the reflected wave is eliminated, following the approach described by Thompson [105]. Conversely, at the top boundary, a non-zero value of $\sigma_{BC} = 0.25$ is imposed.

- Spanwise boundaries:
  To hypothetically increase the spanwise length of the computational domain, periodic boundary conditions are applied along the borders. These periodic boundary conditions ensure that the flow seamlessly wraps around from one side of the domain to the other, creating a periodic repetition of the flow pattern without increasing the computational cost.

A summary of the value imposed at the different boundaries are given in Tab 2.1.

To mitigate the spurious waves at the inlet, outlet, and top boundaries, a sponge zone is combined with the non-reflective BC as represented on the computational domain shown in Fig 2.3. In different studies ([106] and [107]), non-reflective BC alone are insufficient to adequately attenuate spurious reflections, requiring an additional sponge zone. The sponge treatment has since been widely adopted for its ease of implementation and use. Each sponge zone has a prescribed length, $L_{sp,in}$, $L_{sp,out}$ and $L_{sp,fs}$, the length at the inlet, the outlet and the top boundaries, respectively, as well as a specified strength, denoted σ. The research conduct by Mani [107] revealed that bigger sponges outperform smaller sponges of equal strength by effectively dampening reflections. However, larger sponges require larger computational domains and incur higher costs, resulting in a trade-off that establishes the ideal sponge design for each simulation. The inlet and outlet sponge lengths have been adjusted based on the analysis conducted by Wang [52]. Her findings verify that the numerical sponge is strong enough to suppress all numerical oscillations without interfering with the results. It remains essential to perform an analysis of the upper sponge zone.

Periodic blowing and suction waves

The disturbances are numerically represented by prescribing a blowing/suction boundary condition on the wall for the wall-normal velocity. This model was originally introduced by Huai, Joslin, and Piomelli [108] as follows

$$f(x,z,t) = A_1 f_x(x)\sin(\omega_1 t) + A_2 f_x(x) g_z(z)\sin(\omega_2 t) \tag{2.3.8}$$

A_1 and A_2 represent the disturbance amplitude of the 2D and oblique waves, respectively, with ω_1 and ω_2 being their corresponding frequencies. Fasel and Konzelmann [109] defined $f(x)$ and $g(z)$ as

$$g_z(z) = \cos(2\pi z/\lambda_0) = \cos(\beta z)$$
$$|f_x(x)| = 15.11875\xi^5 - 35.4375\xi^4 + 20.25\xi^3$$
$$\xi = \begin{cases} \frac{x-x_1}{x_m - x1} & \text{for } x_1 \le x \le x_m \\ \frac{x-x_2}{x_m - x2} & \text{for } x_m \le x \le x_2, \end{cases}$$

where $x_m = (x_1 + x_2)/2$ and $\beta = 2\pi/\lambda_0$ being the spanwise wavenumber. To maintain a general approach regarding the transition, the forcing function will be modified such that additional oblique modes are excited. As a result, the function $g(z)$ is computed as follows

$$g_z(z) = \sum_{i=-3}^{3} \cos(i \cdot 2\pi z/\lambda_0).$$

Several studies, such as the research conducted by Sayadi *et al.* [37], confirmed the validity of this blowing/suction model. The first term in Eq (2.3.8) initiates the $2D$ primary instability with an angular frequency of ω_1 and an amplitude of A_1. Additional three-dimensional disturbances are added at lower amplitudes and at an angular frequency of ω_2. In this study, the controlled transition is achieved by setting the amplitude of A_1 to be two orders of magnitude greater than that of A_2. The selected frequencies are determined by analysing the stability diagram predicted by the LST. The dimensionless form is computed as

$$F = \omega^* \frac{\mu^*}{\rho^* {u^*_\infty}^2} = \frac{\omega}{Re}. \tag{2.3.9}$$

2.3.4 Initial condition

Using initial conditions that closely approximate the final solution is an effective method to reduce the computational cost of DNS. To approximate the final solution, the prescribed wall-normal, streamwise velocity, and density profiles are obtained by solving the compressible boundary-layer equations (CBLE). The boundary condition required to solve this system are provided in Tab 2.2 from Pandey *et al.* [110].

Velocity		Temperature	
Wall	Free-stream	Wall	Free-stream
$y = 0$	$y \longrightarrow \infty$	$y = 0$	$y \longrightarrow \infty$
$u = 0$	$u = 1$	$T = T_w$	$T = 1$
$v = 0$	$v = 0$		

Table 2.2: The non-dimensional boundary conditions on the velocity and the temperature specified to close the compressible boundary-layer equations.

The system is solved numerically by integrating the Ordinary Differential Equations (ODE) with the Runge-Kutta scheme of 4th-order, together with the Newton-Raphson method to iteratively match the BC, as explained by Onyeador *et al.* [111]. The CBLE are initially transformed from the physical space (x, y) to a computational space (ξ, η), where a self-similar solution is obtained. Self-similar solutions offer a significant advantages, as the transformed boundary layer that has an identical velocity profile regardless of the value of ξ, the streamwise position, as represented in Fig 2.5. The self-similar variables are defined as follows

$$\xi^* = \int_0^x \rho^*_\infty u^*_\infty \mu^*_\infty dx, \qquad \eta^* = \frac{u^*_\infty}{\sqrt{2\xi}} \int_0^y \rho^*_\infty dy. \tag{2.3.10}$$

The transformation from the physical space to the computational space, shown in Fig 2.5, is commonly referred to as the Lees-Dorodnitsyn transformation [112]. Solving the system leads to the Blasius solution, and subsequently, the inverse Lees-Dorodnitsyn transformation is used to obtain the solution in the physical domain.

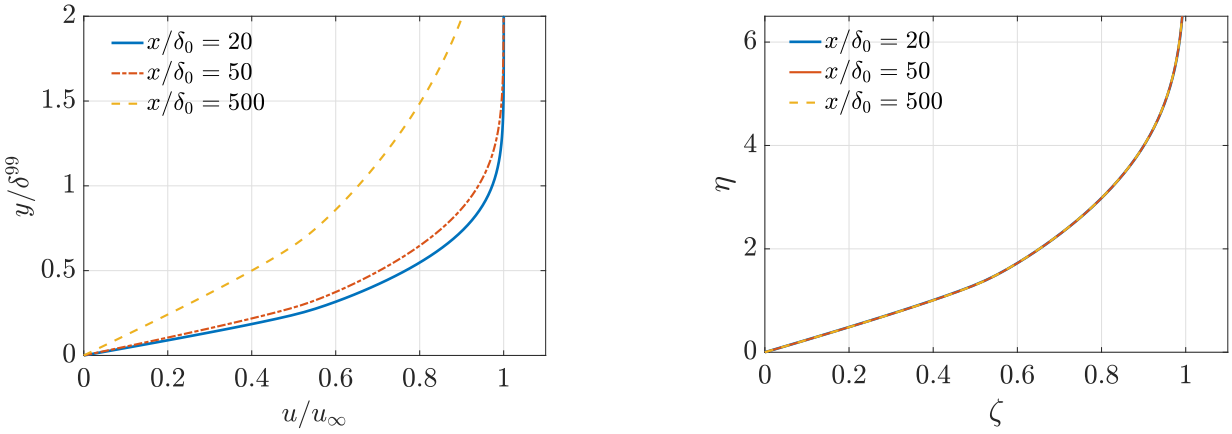

(a) Physical space.

(b) Computational space.

Figure 2.5: Illustration of a self-similar solution of a non-ideal fluid between the physical space (x, y) (a) and the computational space (η, ζ) (b). The transformation from the physical to the computational space is achieved from (a) to (b).

2.4 Direct Numerical Simulations post-processing

The results are extracted when the simulations reach a quasi-periodic state. To ensure that any transient state is suppressed, it is advised ([106] and [52]) to conduct simulations until the first streamwise disturbance has passed the domain twice. Thus, the verification is conducted by visualising the streamwise velocity a specific location within the turbulent region to confirm that the flow has attained a periodic state.

2.4.1 Examination of the perturbation amplification

After achieving the periodic state, the simulation results will undergo a Fast Fourier Transform (FFT) in both time and the spanwise direction to determine the amplitude and growth rate of the perturbation. The FFT requires different input parameters, including the number of disturbance waves and the number of wave samples required. Once the FFT has been conducted, the perturbations can be obtained by subtracting the base flow, determined through time and spanwise averaging, from the total flow. The LST represents the fluctuations as a combination of various modes with a defined frequency ω_n and spanwise wavenumber β. Each mode is denoted by a frequency ω and the spanwise wavenumber β as (ω, β). One should notice that $(\omega_0, 0)$, where ω_0 is the fundamental frequency, correspond to the fundamental $2D$ TS waves. Visualising the amplitude of various eigenmodes at different positions along the streamwise direction facilitates the understanding of the transition mechanism. Two relevant parameters are the growth rate $-\alpha_i$ and the amplitude of the perturbation A introduced as

$$-\alpha_i = \frac{1}{A}\frac{dA}{dx}|_{x0}, \qquad A(x) = A_0 \cdot exp(-\alpha_i(x) \cdot x), \tag{2.4.1}$$

where α_i represents the imaginary part of the streamwise wave number.

The development of the perturbation can be described in terms of various variables. In particular, one needs to select a relevant quantity and investigate its behaviour throughout the domain. According to Wang [52], the best quantity to consider is the streamwise fluctuation u', which is commonly used in current scientific research, such as in Sayadi's [37] and Herbert's [53] work. It is necessary to employ

a method that eliminates the dependency in the wall normal-direction. The different existing methods applied to the streamwise fluctuations are provided in Tab 2.3.

(a)	$\int_0^{L_y} \lvert u' \rvert^2 dy$
(b)	$\lvert u' \rvert$ at a fixed wall normal position
(c)	$\max_y \lvert u' \rvert$

Table 2.3: The different existing method to quantify the growth of the perturbations.

The first method requires numerical integration, which may introduce some loss of accuracy but considers the entire quantity along the wall normal direction, up to a certain limit. The second and third methods are easier to implement numerically and often used in experimental setups as they require only one probe. A comparison of those different criteria was conducted on a simple case. The results given in Appendix B demonstrate that all the criteria provide similar results, assuming that the input parameters are carefully set. Indeed, the use of the second criterion from Tab 2.3 gives results in adequacy with the prediction from the LST provided that the fixed wall normal position remains larger than $y = 0.5/\delta_0$. In this work, the default criterion will be the third one, unless otherwise specified.

The modal analysis consists of decomposing the flow field into different modes based on their frequency and spanwise wavenumber. The required FFT is conducted on two flow periods using 10 samples per period. These parameters have been selected based on the analysis outlined in Appendix B, which investigates their influence on the results.

2.4.2 Examination of the skin-friction coefficient

In addition to the modal analysis, the robustness of the DNS is assessed by analysing of the skin-friction coefficient (C_f). The variation of the skin-friction coefficient in the laminar regime is obtained from the Blasius solution [113]. For the turbulent region, several empirical relationships have been established. In the present study, the 1/7 power-law proposed by White [112] is employed for the subcritical regime. It is important to note that these approximations and empirical relationships are applicable only to fluids operating in the subcritical regime. The Blasius solution assumes a constant pressure throughout the boundary layer [113], which is acceptable for an ideal gas but needs to be modified for non-ideal fluids at supercritical conditions. The mathematical derivation given in Appendix C uses the theoretical definition of the skin-friction coefficient

$$C_f = \frac{\tau_w}{\frac{1}{2}\rho_\infty U_\infty^2}$$

to provide an alternative formula based on dimensionless variables as follows

$$C_f = \frac{2f''(0)C_w}{\sqrt{Re_x}}, \qquad \text{with} \quad C_w = \sqrt{\frac{\rho_w \mu_w}{\rho \mu}}. \tag{2.4.2}$$

The velocity gradient at the wall is denoted as $f''(0)$ and C_w the Chapman-Rubesin factor, which accounts for thermodynamic variations. The evolution of the skin-friction coefficient facilitates the detection of the transition due to its abrupt increase. Different methods exist for defining the location of transition, and they do not always agree (Stetson & Kimmel [114]). In this study, the transition location is determined by identifying the point where C_f reaches its minimum value.

2.4.3 Visualisation of the coherent structures

The coherent structures, Λ and Ω vortices, are emphasised by the Q-criterion. It is defined as the second invariant of the velocity gradient tensor and can be expressed as

$$Q = \frac{1}{2}(|\mathbf{\Omega}^2| - |\mathbf{S}^2|)$$

where $\mathbf{S}$ represents the strain rate tensor and $\mathbf{\Omega}$ the vorticity tensor. Different studies [115] and [116] have employed this criterion to identify regions in the flow where vorticity is concentrated. This criterion enables the differentiation of coherent structures from random fluctuations and background turbulence.

2.4.4 Examination of a fully-turbulent flow

The chaotic behaviour of a turbulent flow requires the analysis of certain averaged quantities. This work uses either the Reynolds averaging [2], which separate the mean flow of a generic variable γ as $\gamma = \bar{\gamma} + \gamma'$ or the Favre-averaging as $\gamma = \tilde{\gamma} + \gamma''$. In the latter method, the mean flow is computed as $\tilde{\gamma} = \overline{\rho\gamma}/\bar{\gamma}$.

Two different scaling approaches are employed in this study. The first scaling method uses plus units, where all quantities are divided by the viscous length scale $\delta_\nu = \mu_w/\rho_w u_\tau$. Here, $u_\tau = \sqrt{\tau_w/\rho_w}$ represents the friction velocity, and μ_w and ρ_w denote the viscosity and density at the wall, respectively. The dimensionless wall coordinate is given by $y^+ = y/\delta_\nu$. However, the plus unit scaling does not account for the large gradients in thermodynamic properties. Therefore, a semi-local scaling, which considers local properties for velocity and the viscous length scale, proposed by Huang *et al.* [117], is introduced as

$$u^*_\tau = \sqrt{\tau_w/\bar{\rho}} \qquad \delta^*_v = \bar{\mu}/\bar{\rho}u^*_\tau.$$

The scaled wall distance is defined as $y^* = y/\delta_v$.

Among the various turbulent statistics, particular focus will be placed on the analysis and comparison of the mean velocity profile, denoted by $u^+ = u/u_\tau$, in the turbulent region. This analysis will include comparing the profile to the theoretical correlation in the log-law region and in the viscous sublayer [2]. In the transcritical boundary layer, the mean velocity profile uses an extra scaling technique, which takes the variation of density into account, known as the Van Driest transformation [118].

$$u^+_{V.D} = \int_0^{\bar{u}} \sqrt{\frac{\bar{\rho}}{\rho_w}} du. \tag{2.4.3}$$

Another important turbulent statistic is the Reynolds stresses, which are computed in wall units, such that they depend only on y^+ as

$$\overline{u'_i u'_j}/u^2_\tau = \overline{u'_i u'_j}^+ \approx f(y^+). \tag{2.4.4}$$

The approximation symbol indicates the absence of a perfect universal scaling, as highlighted by Hoyas & Jimenez [119]. While this scaling is commonly employed in ideal-gas cases, it becomes inadequate in transcritical simulations where the influence of density and viscosity profiles becomes significant. Therefore, the use of the semi-local scaling is required as

$$\overline{\rho u''_i u''_j}/\tau_w = \overline{u''_i u''_j}^* \approx f(y^*, Re^*_\tau). \tag{2.4.5}$$

To determine the amplitude of fluctuations within a transcritical turbulent boundary layer, the Root Mean Square (RMS) value is employed as it provides a meaningful representation of the average magnitude of the fluctuations as

$$\sqrt{\overline{\gamma'\gamma'}}/\bar{\gamma}. \tag{2.4.6}$$

These values are commonly employed in fluid mechanics ([120] and [121]).

Finally, the estimation of coherent structures and their characteristic length can be determined through the two-point correlation analysis of velocity components, as outlined by Moin and Kim [122]. Specifically, they identified a strong correlation between vortical structures and the sharp negative minimum present in the two-point correlation tensor of normal velocity with spanwise separation. The correlation function is defined as

$$R_{ff}(z) = \sum_{k=1}^{N_z-1} \overline{f_k f_{k+k_r}}, \quad k_r = 0, 1, \ldots, k-1, \tag{2.4.7}$$

where $z = k_r \Delta z,\ f = u', v', w'$.

All turbulent statistics have been averaged over 100 different files. Note that in the section discussing turbulent statistics, the superscript $\cdot^*$ indicates the semi-local scaling instead of dimensional properties.

Chapter 3

Ideal-gas simulations

A direct numerical simulation employing the ideal-gas law will be performed to determine the minimum averaging periods required to achieve statistical convergence of the skin-friction coefficient. Additionally, a comparison will be made between the obtained results and those predicted by the linear stability theory (LST) and higher-fidelity data, specifically referencing the work of Herbert [53] and Sayadi *et al.* [37]. This comparative analysis aims to validate the post-processing tools used in this study. Moreover, turbulent flow quantities, encompassing mean flow characteristics and fluctuations, will be presented to illustrate the progression towards a fully turbulent flow.

The physical and numerical parameters correspond to the case *3D IG* in Tab 6.1 with the thermodynamic parameters given in Tab 3.1. The excitation frequencies and amplitudes employed in these simulations have been adjusted to align with the research conducted by Sayadi. Therefore, only the oblique modes with a spanwise wavenumber of $\pm\beta$ are excited. The dimensions in the spanwise and wall-normal directions, along with the number of points in each direction, have been determined based on the study by Wang [52].

p^*_∞	T^*_∞	T_{wall}	Ec
80 Bar	300 K	306 K	0.05

Table 3.1: Thermodynamic parameters used in the ideal-gas simulation.

3.1 Statistical convergence of the skin-friction coefficient

In a turbulent flow, achieving statistical convergence necessitates averaging each quantity over an adequately long time duration. Specifically focusing on the skin-friction coefficient, it is important to assess the impact of the number of samples and the amount of flow periods necessary to reach this statistically converged state.

Influence of the number of periods and samples per period

Fig 3.1(a) presents the skin-friction coefficients obtained by averaging over varying numbers of flow periods using 10 samples per period. The skin-friction coefficient C_f exhibits consistent behaviour for all numbers of periods in the laminar region and prior to the skin-friction overshoot, and are in agreement with the Blasius solution [113] until approximately $Re_x = 5.75 \cdot 10^5$. The minimum in C_f

occur at $Re_x = 4.28 \cdot 10^5$, then the skin-friction rapidly increases and exceeds the value predicted by the turbulent correlation [123]. This overshoot persists from $Re_x = 5.7 \cdot 10^5$ until $Re_x = 8 \cdot 10^5$ after which C_f matches with the turbulent correlation [123]. However, once the flow becomes chaotic, C_f starts to oscillate and the results vary with the number of periods used for averaging. Fig 3.1(a) shows that the statistical convergence is achieved when using 10 periods. Therefore, a 10-period averaging will be used for the skin-friction coefficient throughout this work.

The influence of the discretisation of the perturbing wave shown in Fig 3.1(b) reveals that increasing the number of samples slightly reduces the oscillations. A trade-off between computational cost and accuracy must be made, and in this case, 10 samples seems to be the best compromise as it shows negligible difference with 20 samples. Therefore, 10 samples will be used throughout this work for.

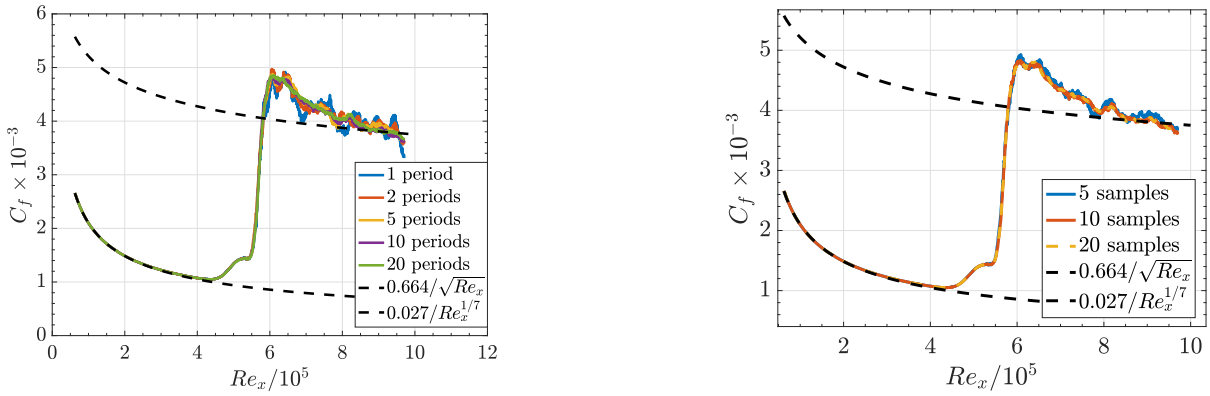

(a) Influence of the number of periods.

(b) Influence of the number of samples.

Figure 3.1: Representation of the evolution of the skin-friction coefficient averaged over the span and the time with (a) different numbers of periods using 10 samples per period, and (b) different numbers of samples per period using 10 periods. The black dotted line represents the Blasius solution [113] in the laminar region and the empirical Prandtl's one-seventh-power law [123] in the turbulent region.

3.2 Validation of the secondary instability

The validation of the results is performed by recovering the results of Herbert [53] and Sayadi [37] for $H-$type secondary instability. The amplitudes of both waves have been carefully established to replicate the growth patterns of the eigenmodes, observed by Sayadi, with the numerical parameters corresponding to case *IG Sayadi* in Tab 6.1.

Fig 3.2(a) represents the evolution of the different FFT modes that were intentionally forced. The TS wave $(\omega_0, 0)$ undergoes linear growth across the domain from $Re_x = 1.72 \cdot 10^5$ to $3.3 \cdot 10^5$, testifying the primary instability, until reaching a saturation amplitude, where a nonlinear behaviour emerges which further decrease the amplitude. The linear behaviour of the TS wave is disrupted when the oblique mode $(\omega_0/2, \beta)$ attains a significant amplitude, providing evidence of the secondary instability. This secondary instability leads to a higher growth rate of the oblique mode after $Re_x = 3.3 \cdot 10^5$. Prior to this Reynolds number, the smaller growth rate is attributed to the primary instability. Subsequently, its interaction with the TS wave occurs around $Re_x = 4 \cdot 10^5$, which corresponds to the minimum value of C_f, indicating the onset of transition. Following these interactions, the flow gradually transitions to a fully turbulent state, indicated by a sudden increase in amplitude of all other oblique modes. Subsequently, at higher Reynolds, all modes start oscillating with the same amplitude. This is indicative

of a turbulent flow, where all modes are present at the same intensity. A good correlation with the prediction of the LST of Herbert [53] and with the higher-fidelity data of Sayadi [37] can be observed for both modes. The variation of the skin-friction coefficient shows a good correlation with the Blasius and the empirical 1/7 power law. Compared to Sayadi's, the growth rate and the amplitude of the overshoot shows negligible difference. However, the location of the transition appears earlier, resulting from discrepancy in perturbation amplitude and the introduction of two oblique waves with $+\beta$ and $-\beta$ while Sayadi only uses $+\beta$.

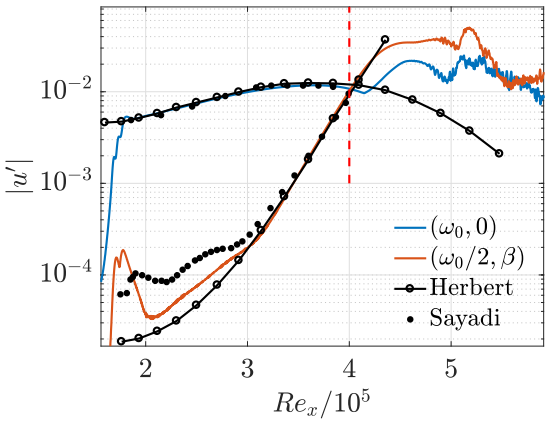

(a) FFT modes.

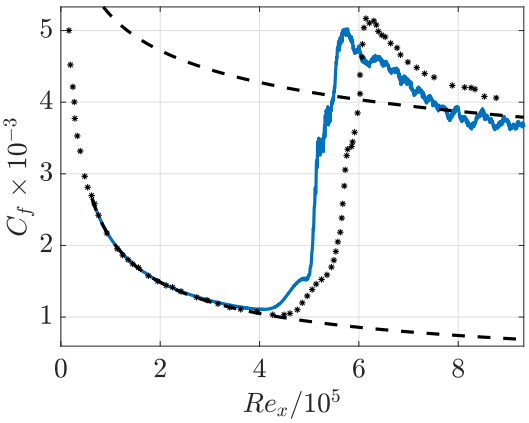

(b) C_f.

Figure 3.2: (a) Representation of the growth of the fundamental two-dimensional mode $(\omega_0, 0)$ and the oblique mode $(\omega_0/2, \beta)$. $(-o)$ LST from Herbert [53]; $*$ DNS from Sayadi [37]. The red dotted line represents the location where C_f reaches its minimum. (b) Evolution of the skin-friction coefficient; the black dotted line represents the Blasius solution [113] in the laminar region and the 1/7 power law [123] in the turbulent region.

3.3 Visualisation of the transition

The transition from laminar to turbulent flow is characterised by the emergence of coherent structures, resulting from the secondary instability, illustrated in Fig 3.3. The presented figure depicts the emergence of Λ-vortices and their staggered alignment, in agreement with the $H-$type transition and the experimental observations by Berlin *et al.* [124]. Moreover, this figure also reveals the formation of the $\Omega-$vortices in the late stage of transition. Those latter vortices breakdown at $x = 420 \cdot \delta_0$, which is the position of the overshoot in C_f. It can be concluded that the breakdown of these vortices leads to high shear stress, consistent with the observations of Nishioka [125].
The transition from a laminar to a turbulent flow can also be observed in Fig 3.4, which presents a snapshot of the streamwise vorticity, velocity, and the skin-friction coefficient in the $(y - z)$ planes at $y \approx 0.35\delta_0$. The emergence of the Λ-vortices is evident from the formation of pairs of positive-negative vorticity regions around $x = 250\delta_0$ in Fig 3.4(a).

In the fully laminar region, a smooth and controlled flow exhibits zero streamwise vorticity. The staggered alignment of the Λ-vortices in the streamwise velocity shown in Fig 3.4(b) are in close agreement with the particle image velocimetry measurement of Berlin *et al.* [124] and the DNS simulation of Sayadi *et al.* [37]. It reveals the numerous amounts of vortices whose length increases from $x = 250\delta_0$ to $350\delta_0$ before the breakdown to turbulence. Overall, the analysis of the skin-friction coefficient depicted in Fig 3.4(c) reveals that the presence of Λ-vortices leads to an increase in the friction coefficient. These

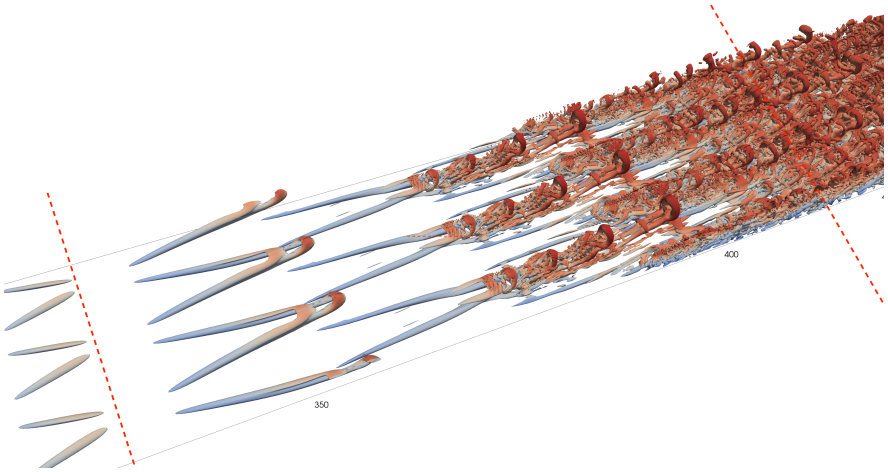

Figure 3.3: Instantaneous isosurfaces of the second invariant of the velocity gradient tensor, Q, coloured by the streamwise velocity. The red dotted lines indicate the positions where the skin-friction coefficient reaches its minimum and maximum values.

vortices are generated in close proximity to the transition location and interact along the span and eventually break down, promoting enhanced mixing within the flow and resulting in a higher value of the skin-friction. The higher values of C_f along the span in the transition region correspond to the region where the Λ-vortices transform into Ω-vortices, characterised by high streamwise and spanwise vorticity.

3.4 Turbulent statistics of a turbulent flow

The mean velocity profile at different Reynolds numbers, presented in Fig 3.5(a), reveals the development from a laminar to a turbulent flow. Previously, the skin-friction coefficient reveals a fully laminar flow for Re_x smaller than $4.5 \cdot 10^5$. The mean profile has therefore the expected laminar flow shape [126] in those regions. The mean velocity profile at a Reynolds of 5.04 and $5.68 \cdot 10^5$, located inside the transition region, shows a large decrease in amplitude, indicating a change in the flow behaviour. However, the mean velocity profile does not yet exhibit the logarithmic profile testifying a fully turbulent flow [2]. This logarithmic velocity profile in the log-law region ($y^+ > 30$) is attained for $Re_x = 7 \cdot 10^5$ and $8.68 \cdot 10^5$. It should be noted that all profiles match the theoretical correlation $y^+ = u^+$ in the viscous sublayer region ($y^+ < 5$), predicted by Pope [2].
The estimation of the coherent structure's characteristic length, obtained from the two-point autocorrelation tensor, shown in Fig 3.5(b), reveals a minimum at $\Delta z^+ = 23.4$ for both $y = 0.067\delta_0$ and $0.15\delta_0$. This finding is consistent with the size of streamwise vortical structures in the near-wall region, found by Sayadi [37]. As the wall-normal height increases, Δz^+ increases, indicating the growth of vortical structures in the wall-normal direction. It is worth mentioning that these curves could appear smoother with a larger number of samples used for averaging.

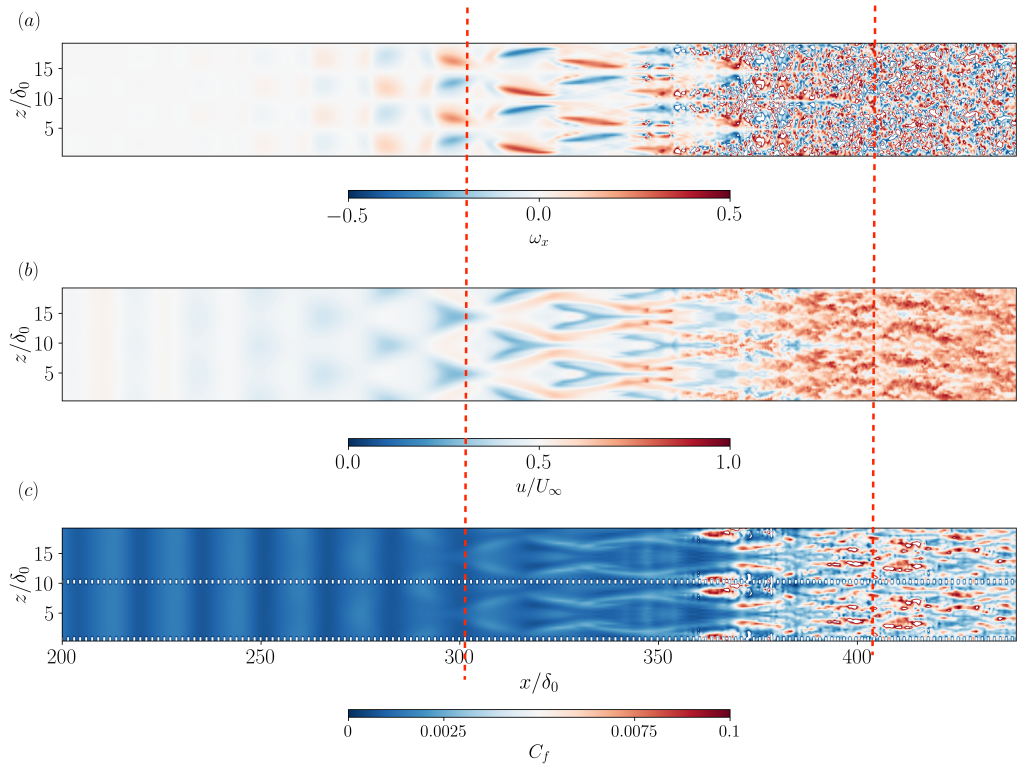

Figure 3.4: The evolution of streamwise vorticity ω_x, streamwise velocity u/U_∞, and skin-friction coefficient C_f, along the flat-plate at $y \approx 0.5\delta_0$ is presented. The location where the skin-friction coefficient reaches its minimum and maximum is indicated by a red line.

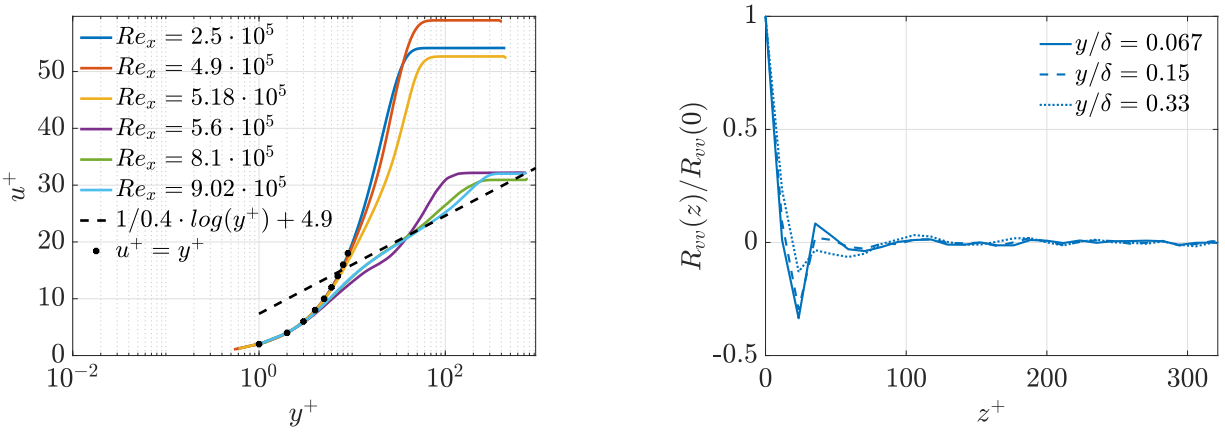

(a) $u^+ - y^+$.

(b) R_{vv}.

Figure 3.5: (a) Wall-scaled turbulent mean velocity at different Reynolds numbers using the dimensionless velocity u^+. The theoretical mean profile in the log law region and in the viscous sublayer [2] (have been scaled to correspond to our non-dimensionalisation). Similar behaviour has been obtained by [37]. (b) Two-point correlations of R_{vv} computed at $Re_x = 8.68 \cdot 10^5$ with varying spanwise separations.

Fig 3.6(b) illustrates the component of the Reynolds stress tensor $-\overline{u'v'}$, which represents the transport of turbulent momentum caused by fluctuations in the streamwise and wall-normal directions. At the lowest Reynolds number, it was expected to obtain zero stresses as the flow is fully laminar.

However, these stresses start to grow at $Re_x = 4.6 \cdot 10^5$, which corresponds to the region where the Λ-vortices form inside the boundary layer. The increase in mean turbulent quantities between $Re_x = 4.6$ to $5.68 \cdot 10^5$ can be observed in Fig 3.6. Between those Reynolds, the skin-friction coefficient increases due to the growth of shear stress exerted by the fluid on the surface caused by the breakdown of the early coherent structure, which increases the turbulence intensity. $Re_x = 5.68 \cdot 10^5$ is located very close to the peak overshoot such that it is not abnormal to obtain such high values. As the Reynolds number increases further downstream, the flow transitions to fully turbulent and the viscous effects start to reduce. This leads to a decrease in the C_f, also evident in the turbulent intensities, which decrease between $Re_x = 5.68$ to $8.68 \cdot 10^5$, as the fully turbulent flow is less influenced by viscous effects. The Reynolds stress distribution at $Re_x = 8.68 \cdot 10^5$ given Fig 3.6(b) reveals that the energy is produced by the streamwise velocity fluctuation from the mean flow in the buffer region (peak at $y^+ = 9$). Moreover, the inhomogeneous nature of the wall-bounded flow results in non-isotropic redistribution of energy. Specifically, the magnitude of $\overline{w'w'}$ is considerably larger than that of $\overline{v'v'}$.

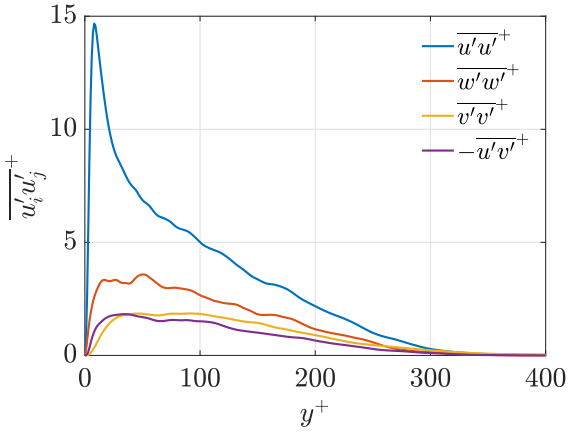

(a) $\overline{u_i'u_j'}^+$.

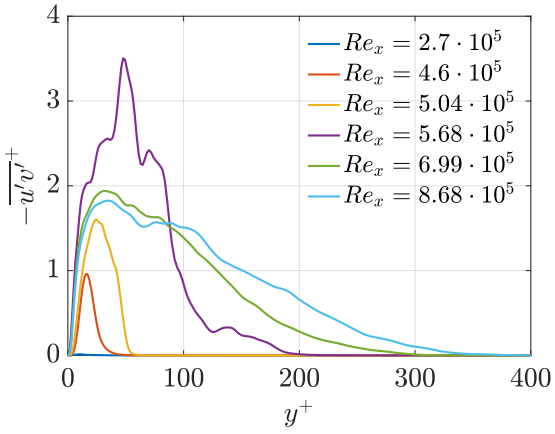

(b) Zoom on $\overline{u'v'}^+$.

Figure 3.6: (a)Distribution of the Reynolds stress at $Re_x = 8.68 \cdot 10^5$ corresponding to a fully turbulent region. (b)Evolution of Reynolds shear stress $-\overline{u'v'}$ along the flat-plate. The results are consistent with the results from Sayadi [37].

Chapter 4

Non-ideal gas simulations

The consistency between the results obtained using theoretical correlations and other higher-fidelity data (Sayadi [37] and Franko [127]) enables to validate our post-processing methods. This simulation also determines the minimum averaged periods required to ensure statistical convergence of the C_f. However, the focus on this thesis is to deepen the understanding of the transition in a transcritical boundary layer, where a real gas equation must be used. The free-stream reduced properties used in the transcritical simulations are listed in Tab 4.1.

parameter	definiton	value
$p_r = p^*_\infty/p^*_c$	Reduced free-stream pressure	1.08
$T_r = T^*_\infty/T^*_c$	Reduced free-stream temperature	0.92
$T_{wall;r} = T^*_w/T^*_c$	Reduced wall temperature	1.08
$T_{wall} = T^*_w/T^*_\infty$	Dimensionless wall temperature	1.18
Ec	Free-stream Eckert number	0.05
M	Free-stream Mach number	0.4
c_v/R	Specific heat/gas constant proportion	9

Table 4.1: Thermodynamic parameters used in the different transcritical simulations.

The fluid is introduced at a supercritical pressure but subcritical temperature. The reduced pseudo-critical temperature at this pressure [61], $T^*_{pc}/T^*_c = 1.011$, can be made dimensionless with respect to the free-stream temperature, resulting in a dimensionless pseudo-critical temperature of $Tpc = T^*_{pc}/T^*_\infty = 1.1$. This implies that when the dimensionless wall temperature exceeds 1.1, as in our case, a transcritical boundary layer is formed, which may result in the appearance of an additional Mode II, as discussed in Sec 1.1.

Transcritical skin-friction coefficient

The theoretical Blasius solution [113] has been modified to account for the large variations of properties across the boundary layer and the different velocity profiles for flows under subcritical or transcritical conditions. These profiles are represented in dimensionless quantities in Fig 4.1(a), using $\eta = y/\delta(x)$ and the velocity ratio $f' = u/u_\infty$. The relative difference between the velocity gradients at the wall between the two cases is approximately 38%, indicating a fuller velocity profile for the transcritical

case. However, the Chapman-Rubesin factor takes into account the strong property gradient in a transcritical fluid, resulting in a higher friction coefficient, as shown in Fig 4.1(b) for a subcritical boundary layer. This analysis produces a novel theoretical skin-friction coefficient profile for a laminar transcritical flow.

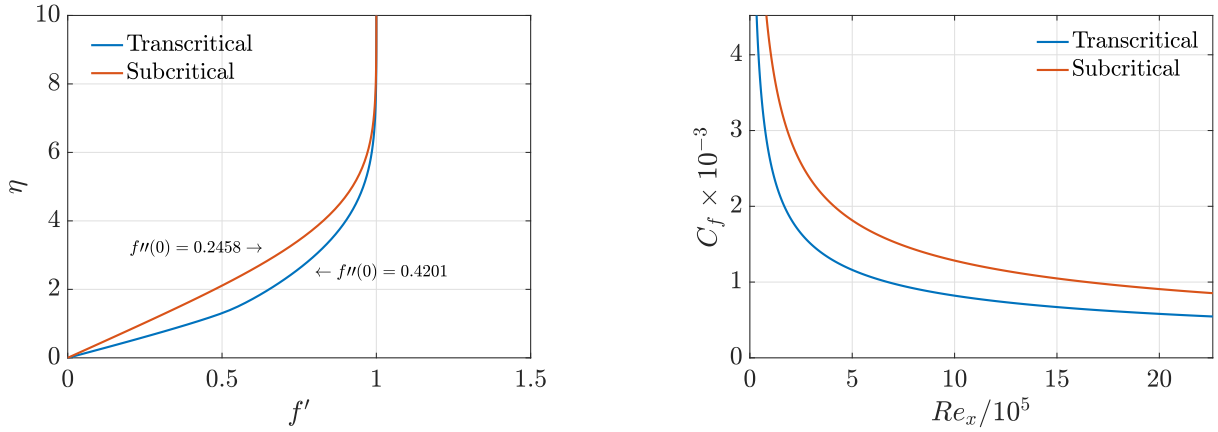

(a) Velocity profile.

(b) Skin-friction coefficient.

Figure 4.1: The different velocity profile for non ideal gas using Van der Waals equation of state for a transcritical and a subcritical simulation. The subcrtical simulations has been conducted with $T_w/T_{cr} = 0.95$.

4.1 Blowing/suction parameters

The reference amplitudes are selected to be sufficiently large to initiate transition and the secondary instability, yet still remain low enough to facilitate early linear growth, based on Wang [52], with

$$A_1 = 2.25 \cdot 10^{-3}, \qquad A_2 = 7.5 \cdot 10^{-5}.$$

Since this work focuses on the H-type transition, it necessitates the excitation of one fundamental frequency and its sub-harmonics. The $2D$ linear stability diagram for the thermodynamic parameters listed in Tab 4.1, assuming a parallel flow, is depicted in Fig 4.2. Both modes are present in the figure, with Mode I located inside Mode II exhibiting a lower growth rate and narrower unstable range. The frequencies should be selected in such a way that only Mode II is excited within the computational domain, without extending the domain excessively leading to a higher computational costs. Therefore, a trade-off is made, and the excitation frequencies are chosen as

$$F_1 = 110 \cdot 10^{-6}, \qquad F_2 = \frac{F_1}{2} = 55 \cdot 10^{-6}. \tag{4.1.1}$$

These frequencies generate unstable two-dimensional waves solely from Mode II within the Reynolds number range of 500 to 1000 and are sufficiently low, considering the errors introduced by the parallel flow assumption [128].
In the following section, for the sake of simplicity, only the fundamental mode $(\omega_0, 0)$ and the oblique mode $(\omega_0/2, \beta)$ will be presented. These modes are chosen because the fundamental mode interacts firstly with this oblique mode. Hence, there is no need to include additional oblique modes in the figures. Further analysis, as presented in Appendix D.3, conducted on a refined domain that only excites $\pm\beta$, demonstrates that the first oblique mode remains unaffected by the presence or absence of other oblique modes.

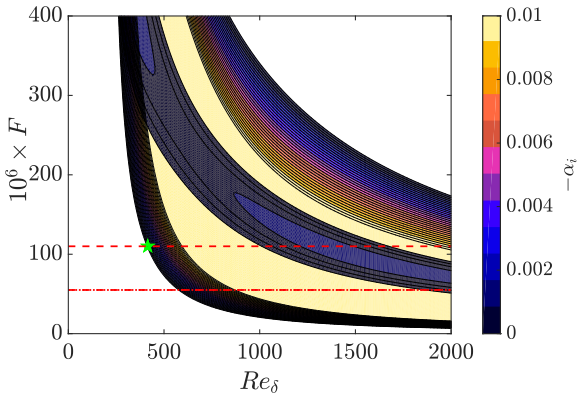

Figure 4.2: $F - Re_\delta$ stability diagram with the thermodynamic properties from Tab 4.1. The red dotted line represents the fundamental frequency F_1 and the subharmonic is represented by a dashed line denoted as F_2. The pentagram shows the middle of the disturbance strip.

4.2 Parameter sensitivity analysis

This study begins by analysing the impact of different numerical parameters on the eigenmodes and the skin-friction coefficient. Specifically, the influence of the top boundaries and the sponge zone is first investigated. This is followed by an examination of the grid quality in all three spatial directions to ensure a mesh fine enough to capture the steep variations of thermodynamic properties close to the Widom line and to capture the Kolmogorov's scale.

4.2.1 Influence of the domain height

To mitigate the blockage effect resulting from the finite height of the domain, which can potentially influence the results, a sufficiently large domain size is required. When designing the computational domain, it is crucial to account for the growth of the boundary layer thickness along the flat-plate and ensure that the domain height remains adequately large to prevent the blockage effect. The grid spacing in the wall-normal direction is maintained as uniform as possible by adjusting the number of grid points and the grid stretching between the simulations. Three simulations were conducted with the numerical and physical parameters corresponding to the case *3D Height Influence* in Tab 6.1. To maintain consistency, the length of the sponge zone on the top boundaries was kept at a ratio of 1/3 with the height of the domain in all simulations, with a constant strength of $\sigma = 1$. The subsequent section demonstrates that this strength is the optimal choice.

Fig 4.3(b) illustrates the skin-friction coefficient, which shows negligible discrepancies among all simulations in the laminar region and agrees with the theoretical C_f represented as a black dotted line. The minimum values observed at $Re_x = 4.58 \cdot 10^5$, $Re_\delta = 676$ indicate the onset of transition, after which the results begin to deviate from each other. A slight delay in C_f can be observed in the simulation with $L_y = 20$. However, notable differences become apparent among all simulations after $Re_x = 5 \cdot 10^5$, possibly due to an excessively coarse streamwise mesh in those quasi-turbulent regions.

To measure the disparities, the relative error based on the area under the curve is used, as

$$\varepsilon = \frac{\int_{Re_{\text{start}}}^{Re_{\text{end}}} C_{f;Ref} - \int_{Re_{\text{start}}}^{Re_{\text{end}}} C_f}{\int_{Re_{\text{start}}}^{Re_{\text{end}}} C_{f;Ref}}, \tag{4.2.1}$$

where $C_{f;Ref}$ the skin-friction coefficient taken as reference. Note that Eq (4.2.1) can also be adapted

to compute the relative error for the different FFT modes.
Taking the curves obtained with $L_y = 60$ as the reference, which should induce the least amount of reflection, the absolute relative error of the skin-friction coefficient can be computed for the different domains. The error is about 1.89% for the smallest domain and decreases to 0.14% when using $L_y = 40$ between $Re_{\text{start}} = 1 \cdot 10^5$ and $Re_{\text{end}} = 5.5 \cdot 10^5$.

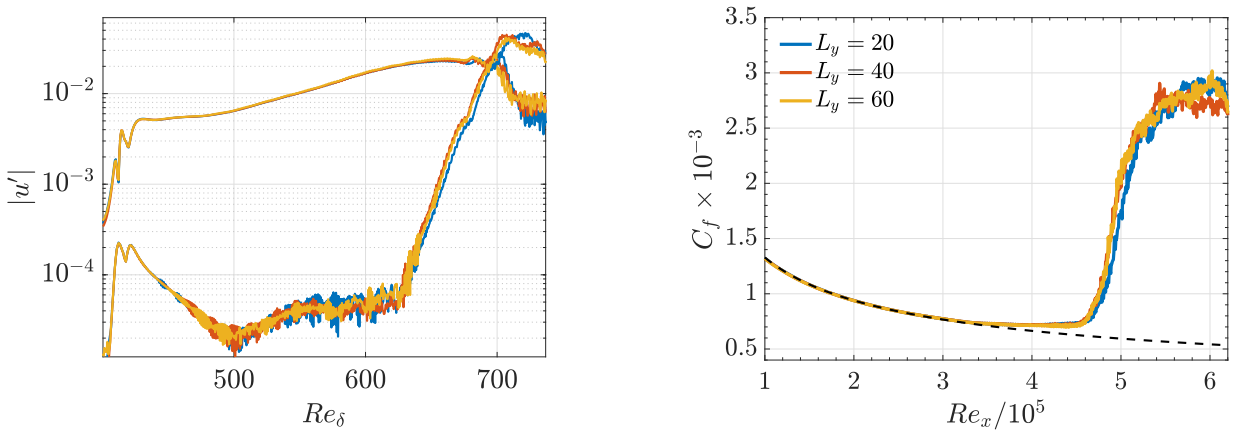

(a) FFT modes.

(b) C_f.

Figure 4.3: (a) Representation of the different eigenmodes $(\omega_0, 0)$ and $(\omega_0/2, \beta)$ corresponding to the higher, average, and lower modes, respectively, on the figure. (b) Representation of the friction coefficient for a domain with varying heights, averaged over 10 periods of the disturbing wave. The black dotted line corresponds to the theoretical skin-friction coefficient. The colour code is indicated in (b).

The influence on the different eigenmodes can be observed in Fig 4.3(a). The fundamental two-dimensional mode shows to be almost insensitive to the domain height, with a relative error below 1% between $Re_\delta = 450$ to 650 for all simulations. However, the oblique mode $(\omega_0/2, \beta)$ appears to be more affected by the domain height, as oscillations with small wavelengths exhibit varying amplitudes with respect to the wall-normal height. Increasing the height of the domain, along with the sponge height, slighlty reduces the magnitude of these oscillations. The remaining non-physical oscillations arise due to a coarse grid in the streamwise direction. Despite these oscillations, the oblique waves exhibit similarities until $Re_\delta = 620$. However, the growth of these eigenmodes beyond this value differs as the oblique mode computed with the smallest domain increases, at the same growth rate as the other modes but, later. This delay is likely due to the blockage effect, which is also responsible for the delay in the skin-friction coefficient. Therefore, these results support the selection of $L_y = 40$. An examination of the boundary layer growth along the domain reveals that the boundary layer thickness at the outlet of the domain is roughly 3.5 times larger than that at the inlet, resulting in an 11-fold difference between L_y and $\delta^{99}_{\text{outlet}}$.

4.2.2 Influence of the sponge

The sponge region, located at the top, must eliminate any undesired wave reflections caused by the boundary conditions. Lengthening and/or strengthening the sponge can enhance attenuation, but it also constrains the computational domain. Based on the previous results, the domain height has been set to $L_y = 40$. The influence of sponge length is examined, while keeping the sponge strength constant at $\sigma = 0.5$. Then, the influence of sponge strength will be evaluated by varying σ while maintaining

	$L_{\text{sponge}} = 1$	$L_{\text{sponge}} = 5$	$L_{\text{sponge}} = 10$
$\varepsilon[\%]$	12.3	1.9	1.8

Table 4.2: Relative errors in the skin-friction coefficient for different sponge lengths using C_f with $L_{\text{sponge}} = 15$ as reference between $Re_{x;\text{start}} = 1 \cdot 10^5$ and $Re_{x;\text{end}} = 6 \cdot 10^5$.

a constant sponge length of $L_{\text{sponge}} = 10$. The physical and numerical parameters correspond to case *3D Sponge Influence* as presented in Tab 6.1.

Fig 4.4 illustrates the effect of the sponge on the skin-friction coefficient. A unit sponge length appears to be inadequate as it accelerates the transition while all curves are very similar to the other simulations until reaching the overshoot and entering the turbulent state, where the results differ. These differences arise from either the streamwise grid spacing, an inadequate number of time steps for averaging, or a combination of both factors. To evaluate the differences, the relative errors based on the area under the curves, using $L_{\text{sponge}} = 15$ as a reference, are presented in Tab 4.2. The incremental improvement in accuracy between $L_{\text{sponge}} = 5$ and $L_{\text{sponge}} = 1$ diminishes significantly as the sponge length increases from $L_{\text{sponge}} = 5$ to $L_{\text{sponge}} = 10$, indicating that a sponge length greater than 5 is necessary. However, the proportional gain does not mandate the use of a larger sponge length.
The C_f for various sponge strength, σ, depicted in Fig 4.4(b), shows good agreement between simulations using $\sigma = 0.5$ and $\sigma = 1$. However, some differences are observed with $\sigma = 5$ because large strength causes the sponge area to function as a wall rather than a sponge [106]. This study reveals that the sponge area must be larger than 5 and the strength should not exceed 1.

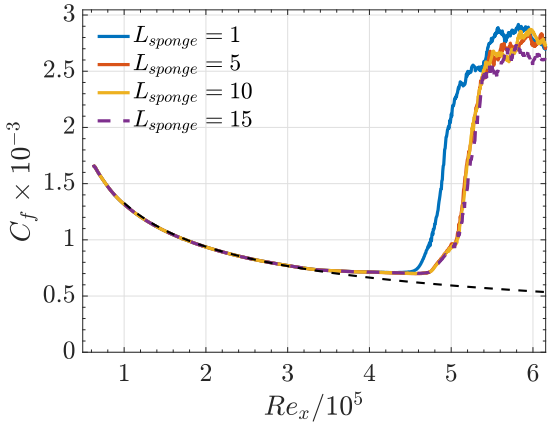

(a) C_f.

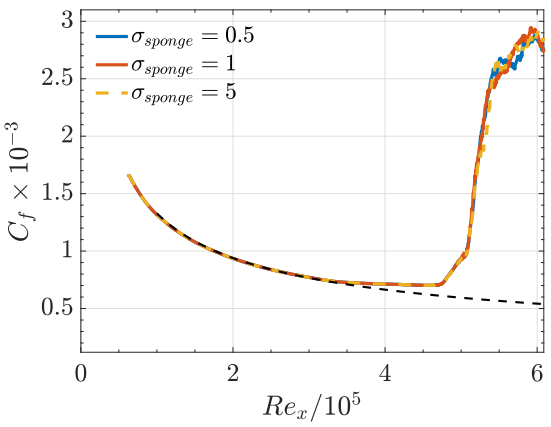

(b) C_f.

Figure 4.4: (a) Representation of the skin-friction coefficient for different lengths of the top sponge with a sponge strength of $\sigma = 0.5$, and (b) for different strengths of the sponge with $L_{\text{sponge}} = 10$. The wall-normal height is fixed at $L_y = 40$. The black dotted line corresponds to the theoretical skin-friction coefficient.

The impact of the sponge length on the FFT modes is shown in Fig 4.5. The oblique mode responsible for the breakdown $(\omega_0/2, \beta)$, exhibits a significant difference when computed with a unit sponge length. Although noticeable variations are apparent in the oblique modes $(\omega_0/2, \beta)$ for sponge lengths larger than 5 at Re_δ ranging from 450 to 650, the growth rate, which serves as evidence of the secondary instability, remains fairly consistent. Given that the minor differences before $Re_\delta = 650$ are inconsequential. This observation is consistent with the friction coefficient depicted in Fig 4.4

confirming that a unit sponge length is not appropriate.
The presence of non-physical oscillations with small wavelengths seems to be unaffected by the length of the sponge reinforcing the impact of the streamwise grid spacing rather than any sponge-related factors. To avoid overburdening the report, the figures illustrating the behaviour of modes $(\omega_0/2, 2\beta)$ and $(\omega_0/2, 0)$ for various sponge lengths, as well as the modal analysis for different sponge strengths, are provided in Appendix D.5. These figures lead to similar conclusions. The findings of this study demonstrate that the sponge length must be larger 5, while the strength should not surpass 1. The sponge length and strength at the domain's inlet and outlet were adopted from previous research ([52] and [106]).

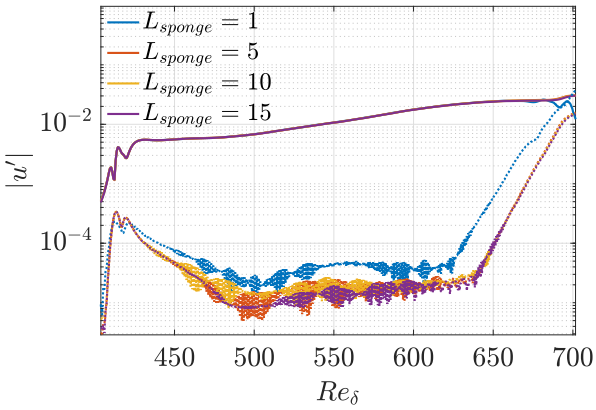

Figure 4.5: Representation of $2D$ FFT mode $(-)(\omega_0, 0)$ and one oblique mode $(--)(\omega_0/2, \beta)$ for different sponge lengths with $\sigma_{\text{sponge}} = 0.5$.

4.3 Effect of the grid resolution

The influence of grid spacing in each spatial direction needs to be evaluated in order to accurately capture the physics at different length scales and reduce the oscillations present in the oblique modes. Initially, simulations are conducted with a constant distribution in the streamwise and spanwise directions with the numerical parameters corresponding to case *3D Study-Grid-1* in Tab 6.1 where the sponge has been fixed based on the previous study.

Fig 4.6 shows notable differences in both the growth of the different eigenmodes and the skin-friction coefficient after the transition when the streamwise grid spacing is slightly decreased. It appears that a coarse mesh overestimates the skin-friction coefficient and advances the transition. For instance, the peak amplitude with $\Delta x = 0.68$ occurs at $Re_x = 5.62 \cdot 10^5$ with an amplitude of $3.13 \cdot 10^{-3}$, while using $\Delta x = 0.40$ gives the peak at $Re_x = 6.04 \cdot 10^5$ with an amplitude of $2.72 \cdot 10^{-3}$. This phenomenon can be understood from Fig 4.6(a) as the oblique mode are significantly different between all simulations. Furthermore, in contrast to previous studies, the fundamental two-dimensional wave also exhibits significant differences. This is unexpected since the forcing parameters are identical in all simulations. Since this $2D$ mode is responsible for driving the secondary instability, and thus the transition, it is crucial to ensure that the same amplitude is obtained in all simulations.
The reason behind this phenomenon is the insufficient discretisation of the forcing wave. As the number of points along the disturbance strip is low, it results in poor wave capture. The physical maximum amplitude of the disturbing wave is not accurately captured, making it impossible to compare the results since the numerical forcing is not the same. Therefore, it is crucial to investigate the minimum number of grid points required to accurately capture the waves. Note that increasing the number

of points decreases the amplitude of the oscillations present in the oblique mode during the primary instability.

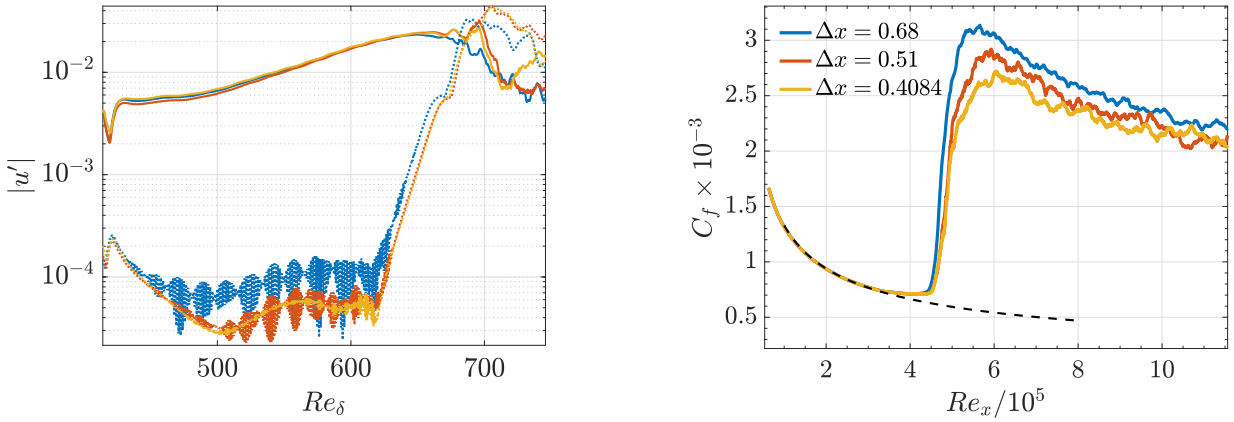

(a) FFT modes. (b) C_f.

Figure 4.6: (a) Representation of the FFT mode $(-)(\omega_0, 0)$, $(--)(\omega_0/2, \beta)$ with different streamwise grid spacing. (b) Representation of the skin-friction coefficient for different numbers of points in the streamwise direction. The black dotted line corresponds to the theoretical skin-friction coefficient.

4.3.1 Capture of the forcing wave

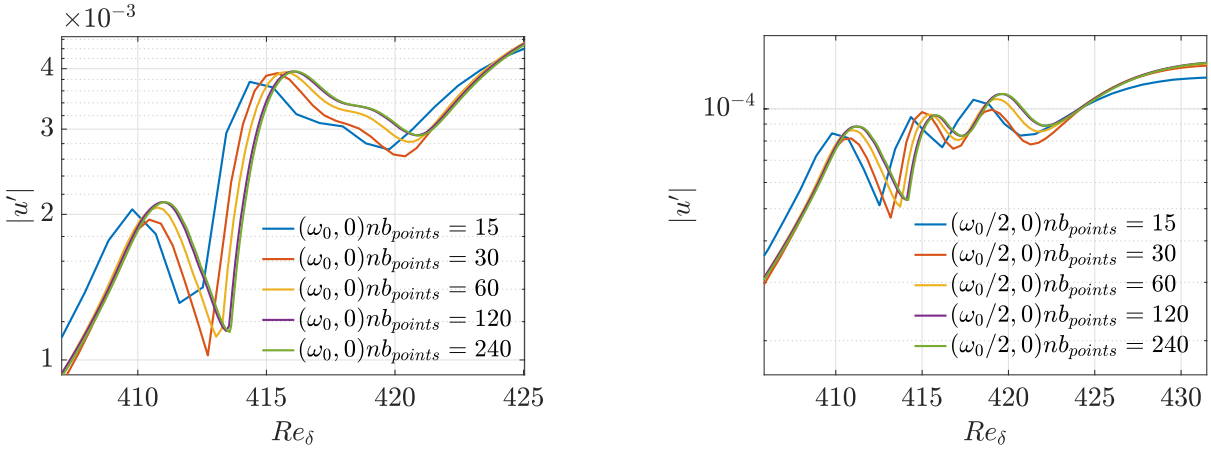

(a) $(\omega_0, 0)$. (b) $(\omega_0/2, 0)$.

Figure 4.7: Representation of the FFT modes $(\omega_0, 0)$ and the subharmonic $(\omega_0/2, 0)$ for different numbers of grid points in the disturbance strip.

The determination of the optimal number of points along the disturbance strip, which has a length of $10\delta_0$ will be performed on a smaller domain to accelerate the simulation. The numerical and physical parameters correspond to case *2D-Resolution* in Tab 6.1. Initially, 10 samples per period were used, and the number of grid points in the streamwise direction was increased to examine the impact on the different modes. Fig 4.7 reveals that 120 grid points in the disturbance strip begin to discretise the forcing waves properly, resulting in similar amplitudes of the various modes near the disturbance zone. The same results were obtained for other modes, presented in Appendix D.5.
However, if 120 points are used in the disturbance strip, maintaining the same level of refinement in

the other direction would require over 150 million grid points, leading to a computationally expensive simulation. Therefore, it is essential to find a cost-effective approach to obtain consistent amplitudes in the forcing zone without increasing too much the computational cost. The impact of the number of samples employed to discretise the forcing wave is discussed in Appendix D.5. The results indicate that, for a fixed number of points, increasing the number of samples enhances the amplitude associated with each mode along the disturbance strip and displays a collapse using 40 samples. However, considering the computational cost, a choice of 10 samples is retained, which still yields satisfactory outcomes.

4.3.2 Modification of the streamwise distribution

In order to decrease the grid spacing solely along the disturbance strip and in the turbulent region, the suggested approach involves employing a non-equidistant streamwise distribution. In all subsequent simulations employing non-equidistant streamwise distribution, 120 points along the disturbance strip have been used to model the same forcing wave in an efficient way. Based on previous analyses, the starting point of the transition starts around $Re_\delta \approx 620$, such that the second refinement region starts at $Re_\delta \approx 610$. To visualise the effect of a smaller grid spacing, the mesh in the turbulent region will be refined from $\Delta x_{\text{turb}} = 0.25$ to 0.05, while the grid spacing in the laminar region is kept constant at $\Delta x = 0.3$, based on Wang [52], to reduce computational cost. The numerical and physical parameters correspond to case *3D Study-Grid 2* in Tab 6.1.

The growth of the different eigenmodes, shown in Fig 4.8(a), reveals that the fundamental $2D$ mode remains insensitive to the refinement in the turbulent region before the interaction with the oblique mode. On the other hand, the oblique mode is significantly affected by the grid spacing during the transition region. The growth of the modes computed with $\Delta x_{\text{turb}} = 0.15$ and 0.10 starts earlier than the one obtained with $\Delta x_{\text{turb}} = 0.25$, resulting in an earlier transition. This explains the similar decrease in amplitude for the $2D$ mode at $Re_\delta = 685$ using $\Delta x_{turb} = 0.15$ and 0.10 which appears later, at $Re_\delta = 692$, with $\Delta x_{turb} = 0.25$. The oblique mode computed with the finest grid $\Delta x_{\text{turb}} = 0.05$ has a surprisingly lower growth, leading to an interaction with the $2D$ modes further downstream. Despite their similarity in growth rates across all simulations, their distinctive starting points result in variations in the location of the transition. This variation is evident from the friction coefficient presented in Fig 4.8(b).

The trend observed by refining the grid is unusual, as the initial refinement accelerates the transition, but further refinement delays it. There are several possible reasons that can explain this phenomenon: the use of a grid spacing of 0.05 enables the capture of a phenomenon at smaller length scales not captured previously, or a numerical issue caused by the strong variation of the grid spacing near $Re_\delta = 600$. It is also important to note that simulations conducted with $\Delta x_{\text{turb}} = 0.10$ and 0.05 crashed multiple times, which supports the idea of a numerical issue being responsible for the abnormal behaviour of the oblique modes. Initially, it was hypothesised that crashes occurring in simulations conducted with $\Delta x = 0.10$ and 0.05 were due to a large aspect ratio between the streamwise and spanwise grid spacing. Refining the mesh in the turbulent region creates rectangular cells with very large aspect ratios, given in Tab 4.3, which can cause numerical errors. Jiménez *et al.* [129] investigated the influence of the ratio between the streamwise and spanwise direction, in a subcritical boundary layer, and found that the use of an aspect ratio smaller than 0.25 results in spurious secondary flows and an artificially enhanced level of turbulence, which may cause simulation crashes. Regarding the current thermodynamic properties of the flow, additional investigations are required to assess its suitability for supercritical flows.

Aspect ratio:	$\Delta x_{\text{turb}} = 0.25$	$\Delta x_{\text{turb}} = 0.15$	$\Delta x_{\text{turb}} = 0.10$	$\Delta x_{\text{turb}} = 0.05$
$\Delta x_{\text{turb}}/\Delta z$	0.7576	0.4545	0.3030	0.1515

Table 4.3: The aspect ratio between the streamwise and spanwise directions of the grid cells found in the turbulent region.

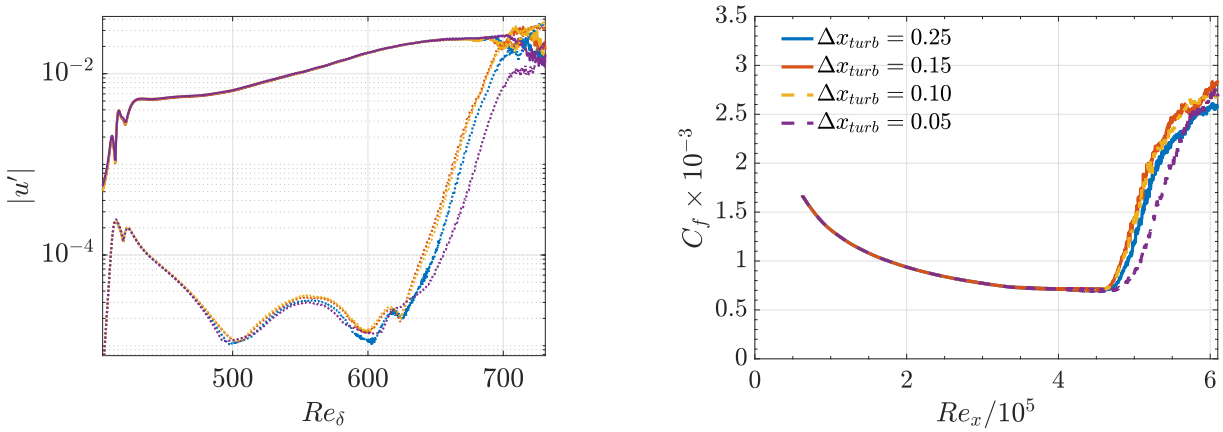

(a) FFT modes.

(b) C_f.

Figure 4.8: (a) Representation of different FFT modes obtained with different mesh refinements in the turbulent region. $(-)$ represents the mode $(\omega_0, 0)$, $(..)$ represents the mode $(\omega_0/2, \beta)$. The colour code is given in the skin-friction coefficient. (b) Representation of the skin-friction coefficient obtained with different mesh refinements in the turbulent region.

4.3.3 Effect of the grid ratio

The influence of the spanwise grid spacing was initially examined on the mesh with the coarsest grid spacing of $\Delta x_{\text{turb}} = 0.25$. The analysis, presented in Appendix D.1, indicates that the ratio of the streamwise and spanwise grid spacing should be at least 0.75 to ensure the stability of the simulation. Furthermore, this preliminary investigation shows that the grid aspect ratio has minimal impact on the growth of the different FFT modes.

Then, additional simulations were performed on a finer mesh with a ratio of $\Delta x_{\text{turb}}/\Delta z = 1$ and 2 to validate these findings. The modal representation, given in Fig 4.9(a), indicates that the impact of the ratio $\Delta x_{\text{turb}}/\Delta z$ on the different FFT modes remains negligible. The friction coefficient, shown in Fig 4.9(b) indicates that the transition location and the growth of the C_f are very similar, irrespective of the value of the ratio. However, this observation does not hold for the amplitude of the peak overshoot at $Re_x = 6 \cdot 10^5$, as it varies depending on the aspect ratio, but only for the two coarser grids. Two important observations were made. Firstly, while the modes obtained with Δx_{turb} and an aspect ratio of 1 or 2 are relatively similar in the transition region, there is a noticeable difference in the amplitude of the overshoot on the friction coefficient. Secondly, the disparity in the starting point at which the first oblique mode begins to grow, as observed previously, between $\Delta x_{\text{turb}} = 0.25$ and 0.10, is not caused by the spanwise grid spacing.

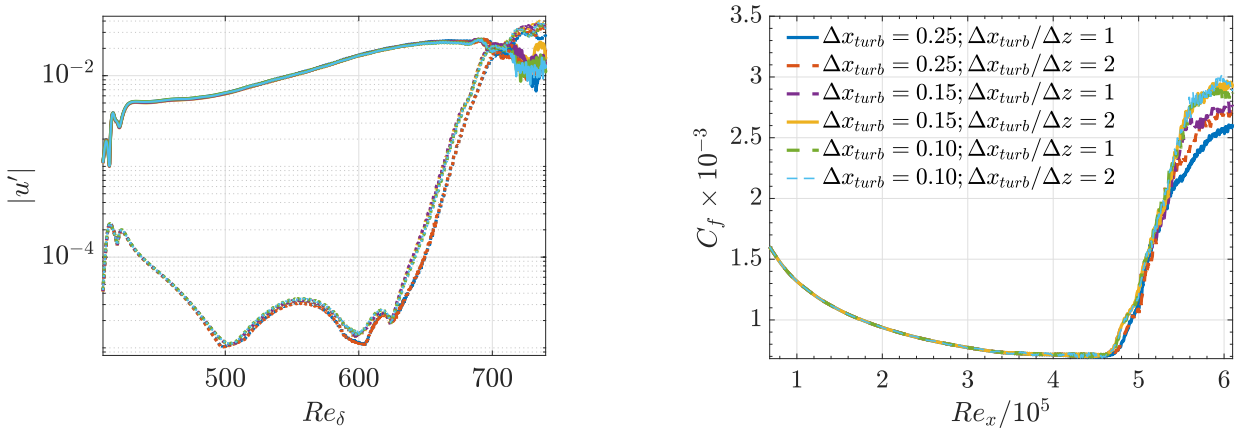

(a) FFT modes.

(b) C_f.

Figure 4.9: (a) Representation of different FFT modes obtained for different refinement of Δx_{turb} in the turbulent region, as well as various refinements in the spanwise direction. $(-)$ Represents the mode $(\omega_0, 0)$, (..) represents the mode $(\omega_0/2, \beta)$. (b) Representation of the friction coefficient obtained for different refinements of Δx_{turb} in the turbulent region and various refinements in the spanwise direction. The colour code is indicated in (b).

Based on these findings, a ratio of 1 between the streamwise and spanwise grid spacing will be imposed to ensure stability in the simulations. Increasing the ratio beyond this point would considerably increase the computational costs without significantly improving the quality of the results. This choice aligns with other studies such as Kim *et al.* [130]. Nevertheless, the use of a streamwise grid spacing of $\Delta x = 0.1$, which corresponds to $\Delta x^+ = \Delta x \cdot Re_\tau = 5.4$ in wall units is in accordance to other DNS simulations, such as Sayadi [37] with $\Delta x^+ = 10.3$ and Kawai [120] with $\Delta x^+ = 5.1$ and a ratio $\Delta x/\Delta z = 1$. However, in the transcritical simulation, Kawai [120] used a streamwise grid spacing of $\Delta x^+ = 3$. Therefore, to ensure that all the smallest length scales are accurately captured, two additional simulations with a streamwise grid spacing of $\Delta x^+ = 4$ and 2.6, which correspond to $\Delta x_{\text{turb}} = 0.075$ and 0.05, respectively, are conducted.

Remarkably, it has been observed that further grid refinement unexpectedly delays the transition, as illustrated in Fig 4.10(b). The friction coefficient computed on the two finest grids reaches its minimum value at $Re_x = 4.75 \cdot 10^5$, whereas it occurs at $Re_x = 4.6 \cdot 10^5$ with $\Delta x_{\text{turb}} = 0.1$. The most significant discrepancies are observed in the oblique mode $(\omega_0/2, \beta)$, shown in in Fig 4.10(a). In the laminar region, this mode has a relatively similar shape, although there is an offset in amplitude. However, close to $Re_\delta = 600$, the shape abruptly changes with the presence of a sharp minimum, when $\Delta x_{\text{turb}} = 0.10$, not visible on the finer meshes. After this extremum, the oblique mode increases until it crosses the fundamental $2D$ mode at $Re_\delta = 695$. However, on the finer meshes, this minimum does not appear, resulting in a delayed increase. Subsequently, the interaction occurs at $Re_\delta \approx 715$ instead of 695, which explains the delay in the skin-friction coefficient.

The analysis has brought to light a convergence issue. Moreover, due to computational constraints, it is not feasible to continue increasing the number of points in the streamwise direction. A significant alteration in the presented oblique mode is observed at around $Re_\delta = 620$, which is in close proximity to the region where the mesh begins to be refined. Consequently, the numerical error is possible, and in order to eliminate this possibility, three distinct simulations will be performed on a mesh with an equidistant distribution in the streamwise direction.

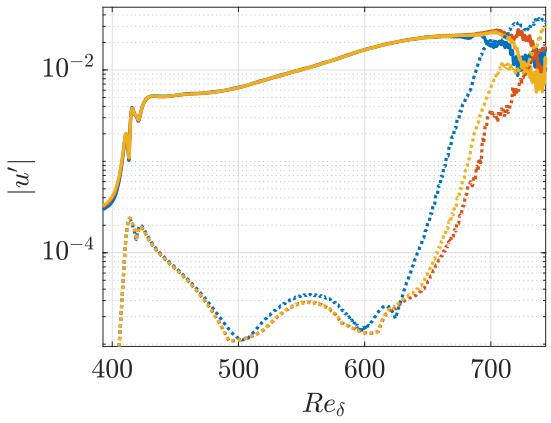

(a) FFT modes.

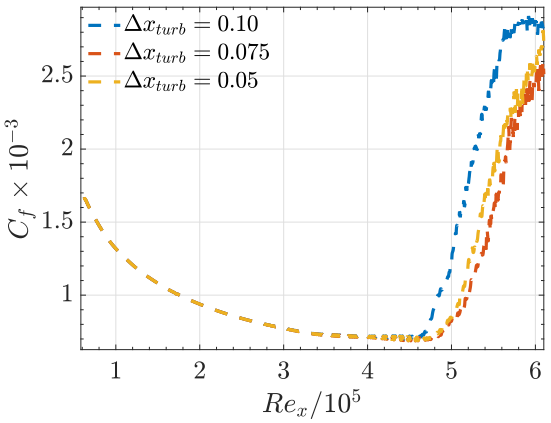

(b) C_f.

Figure 4.10: (a) Representation of different Fast-Fourier transform modes obtained using different mesh refinements in the turbulent region while maintaining a unit ratio between the streamwise and spanwise directions. $(-)$ represents the mode $(\omega_0, 0)$,$(-.)$ represents the mode $(\omega_0/2, 0)$, $(..)$ represents the mode $(\omega_0/2, \beta)$. (b) Representation of the skin-friction coefficient. The colour code is indicated in (b).

4.3.4 Validation using equidistant distribution

Three simulations are conducted with a streamwise equidistant distribution with the physical and numerical parameters corresponding to case *3D Study Grid Equid* in Tab 6.1.

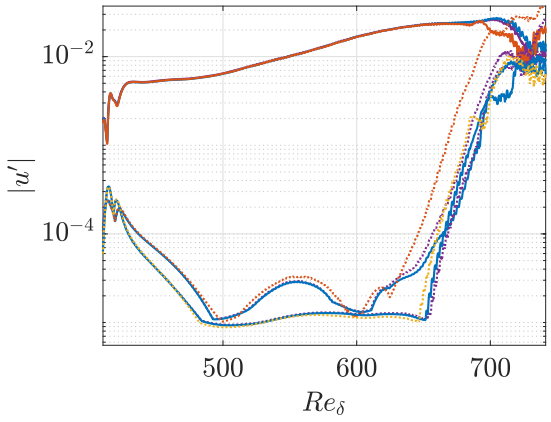

(a) FFT modes.

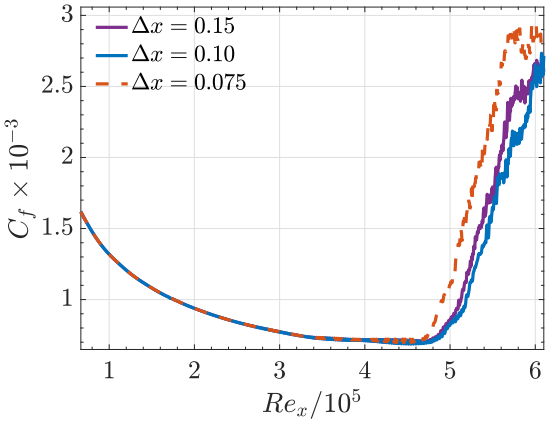

(b) C_f.

Figure 4.11: (a) Representation of different Fast-Fourier transform modes obtained using different equidistant mesh. $(-)$ represents the mode $(\omega_0, 0)$,$(-.)$ represents the mode $(\omega_0/2, 0)$, $(..)$ represents the mode $(\omega_0/2, \beta)$, $(--)$ represents the mode $(\omega_0/2, 2\beta)$. (b) Representation of the skin-friction coefficient computed on different meshes. The colour code is indicated in (b).

The behaviour of the C_f using a non-equidistant mesh, presented in Fig 4.10(b), exhibits a reversal behaviour compared to the simulations performed on an equidistant mesh in Fig 4.11(b). When using a non-equidistant mesh shows a delayed transition as the grid spacing decreases. In contrast, when using a finer equidistant mesh, the transition occurs earlier. For instance, the location of the transition

using the non-equidistant mesh with $\Delta x_{\text{turb}} = 0.075$ occurs at $Re_x = 4.78 \cdot 10^5$, while the equidistant mesh with the same grid spacing indicates a transition at $Re_x = 4.67 \cdot 10^5$. The reason behind this opposite behaviour becomes evident from the evolution of the eigenmodes depicted in Fig 4.11(a). On the equidistant mesh, the mode $(\omega_0/2, \beta)$ exhibits a distinct sharp minimum followed by a rapid increase, resulting in an earlier transition. However, when using the same grid spacing on a non-equidistant basis (Fig 4.10), this minimum disappears, and a delayed growth similar to the finest non-equidistant grids is observed. This is counter-intuitive from a numerical standpoint. It appears that there is an extremely sensitive additional parameter that determines whether the transition path.

To investigate this unusual behaviour and eliminate the possibility of other modes affecting the transition path, the amplitudes of all modes on two equidistant grids will be presented at different Reynolds numbers ranging from $Re_\delta = 600$ to $Re_\delta = 680$, covering the extremum of $(\omega_0/2, \beta)$. The amplitudes of these modes using both the coarser and finest equidistant grids are presented in a matrix form in Fig D.2 in the Appendix D.2 for space savings. Notably, that the high amplitudes observed for the harmonics of the $2D$ waves persist consistently across all Reynolds numbers and for both simulations, suggesting a potential influence on the transition process. These harmonics were present in the ideal gas simulation but had amplitudes two orders of magnitude lower than that of the fundamental mode, making them negligible. However, in this study, the non-linearity present in the system due to the transcritical conditions and the use of the Van der Waals EoS, seems to generate higher-amplitude harmonics, as represented in Fig 4.12(a). The existence of these harmonics has been previously reported in Lee's work [131] and Marxen's study [132]. They discovered that these higher harmonics can have significant amplitudes for the prediction of the transition. The following section Sec 4.4 will present an analysis of these harmonics and the introduction of a method aiming to mitigate their amplitudes.

The amplitude analysis of oblique modes at increasing Reynolds numbers, specifically $Re_\delta = 670$ and 690, reveals some surprising behaviour. On the finest grid, two non-excited oblique modes, namely $(3\omega_0/2, \beta)$ and $(5\omega_0/2, \beta)$, have significant amplitudes comparable to the excited mode $(\omega_0/2, \beta)$, but solely on the finest grid. This increase in amplitude of these non-excited oblique modes is attributed to the presence of nonlinearity, which lead to this mode capture. It is worth noting that the mode with a higher spanwise wavenumber (2β and 3β) shows lower amplitudes in both simulations. The modal representation of these two oblique modes, $(3\omega_0/2, \beta)$ and $(5\omega_0/2, \beta)$, shown in Fig 4.12, indicates the presence of nonlinear interactions. These modes exhibit growth rates comparable to the excited mode $(\omega_0/2, \beta)$. This mode coupling phenomenon is observed on both grids, but it occurs later on the coarser grid, which explains the difference observed in the matrices. At the highest Reynolds number, it is expected to observe significant differences between the two grids since the oblique mode on the finer mesh has already interacted with other modes, resulting in a relatively turbulent flow. It should be noted that in all simulations with a minimum occurring in the oblique mode $(\omega_0/2, \beta)$ at $Re_\delta = 620$, a consistent behaviour is observed. Similarly, simulations that do not demonstrate this minimum exhibit the opposite behaviour.
At this stage, it remains unclear which parameters influence the path to turbulence. Since both grids exhibit similar behaviour with respect to the different harmonics, the fundamental mode and three oblique modes with 1β, it is unlikely that these harmonics alone are responsible for the different transition. This investigation highlights the nonlinearity that exist in the system. Nonetheless, the precise mechanism that leads to the modification of the transition remains unclear.

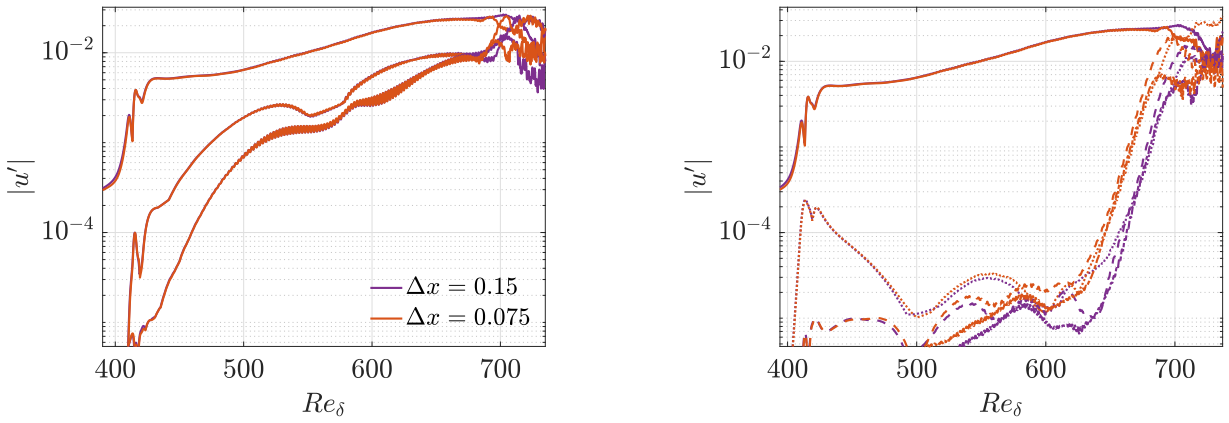

(a) Harmonic.

(b) FFT modes.

Figure 4.12: (a) Representation of different harmonic modes $(\omega_0, 0)$,$(2\omega_0, 0)$ and $(3\omega_0, 0)$ obtained with different equidistant meshes. (b) Representation of different Fast-Fourier transform modes obtained with different equidistant meshes. $(-)$ represents the mode $(\omega_0, 0)$; $(..)$ represents the mode $(\omega_0/2, \beta)$; $(--)$ represents the mode $(3\omega_0/2, \beta)$; $(-.)$ represents the mode $(5\omega_0/2, 0)$.

In order to gain further insights into the system and understand the differences between the two simulations, the profiles of the streamwise velocity fluctuations and density fluctuations profiles, for the fundamental mode $(\omega_0, 0)$ and two oblique modes $(\omega_0/2, \beta)$ and $(\omega_0/2, 2\beta)$, will be analysed at various Reynolds numbers to understand the difference between both simulations. To prevent overloading the report, only two density profiles at two Reynolds numbers are presented in Fig 4.13, normalised by the maximum amplitude, while the remaining streamwise velocity and density profiles can be found in Appendix D.4.

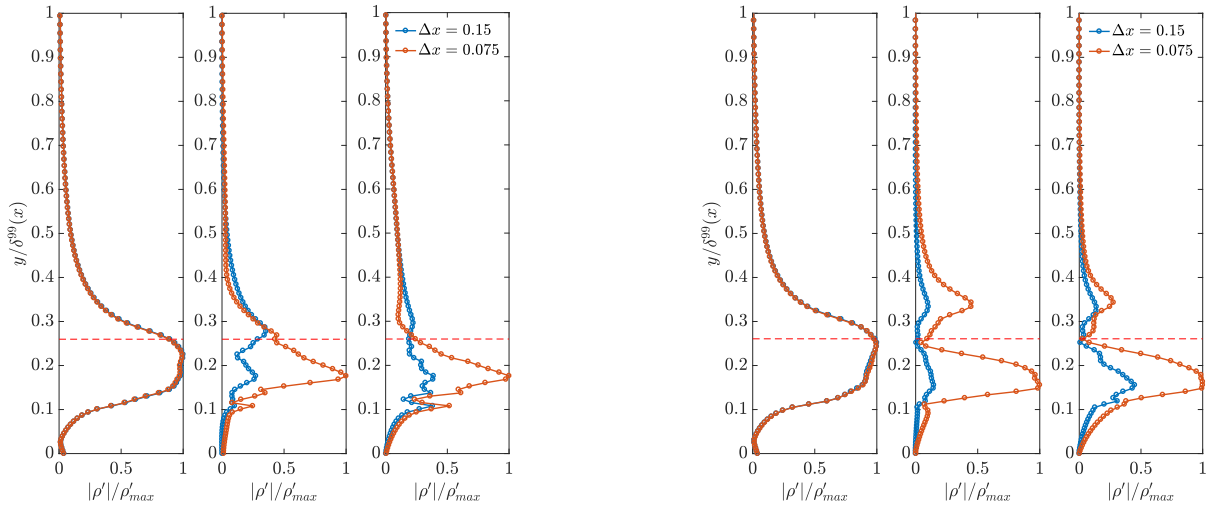

(a) $Re_\delta = 650$.

(b) $Re_\delta = 670$.

Figure 4.13: Representation the density fluctuation profile for the fundamental mode (left) $(\omega_0, 0)$ and the oblique modes (middle) $(\omega_0/2, \beta)$ and (right) $(\omega_0/2, 2\beta)$. The red lines indicate the location of the pseudo-critical temperature.

The analysis of the fundamental streamwise velocity and fluctuation profiles reveals negligible differences in shape but exhibit significant differences in amplitude across all Reynolds numbers. These differences in amplitudes are particularly noticeable in the oblique density fluctuation profiles, where a factors larger than 2 are observed between the simulations at $Re_\delta = 650$ and 670. The larger amplitudes observed on the finest grid may potentially account for their earlier growth. Regarding the wall-normal discretisation, it appears to accurately capture the different peaks present in the streamwise velocity fluctuation profiles at all Reynolds numbers. However, the presence of sharp gradients in the density profiles, close to the Widom line, highlights the limitations of the present discretisation. Indeed, the numerous peaks present in the oblique modes at lower Reynolds numbers, which decrease across the domain, are not accurately captured. The resolution used in the simulations could potentially miss the true maximum of the different eigenmodes, leading to a discrepancy in amplitude between the two simulations. This discrepancy, in turn, may generate a different pathways to turbulence. This study reveals the limitations of the wall-normal grid spacing in capturing the different peaks present in the fluctuating density profiles of the various oblique modes potentially leading to the difference in amplitude in the other profiles.

The instantaneous vortical structures observed in both grids, shown in Fig 4.14 where the spanwise length of the computational domain has been replicated three times, reveals the distinct paths taken to achieve a turbulent flow. The simulation computed with a grid spacing of $\Delta x = 0.15$, reveals the significance of the second oblique mode $(\omega_0/2, 2\beta)$, as indicated by the presence of six complete, like Ω-vortices during the early stages of transition. The growth of this mode is observed to be delayed compared to $(\omega_0/2, \beta)$, but interacts with the $2D$ mode at nearly the same. This explains the visualisation of successive arrangements of six and three Ω-vortices. In contrast, the finer grid is more influenced by the first oblique mode, resulting in the presence of only three Ω-vortices.

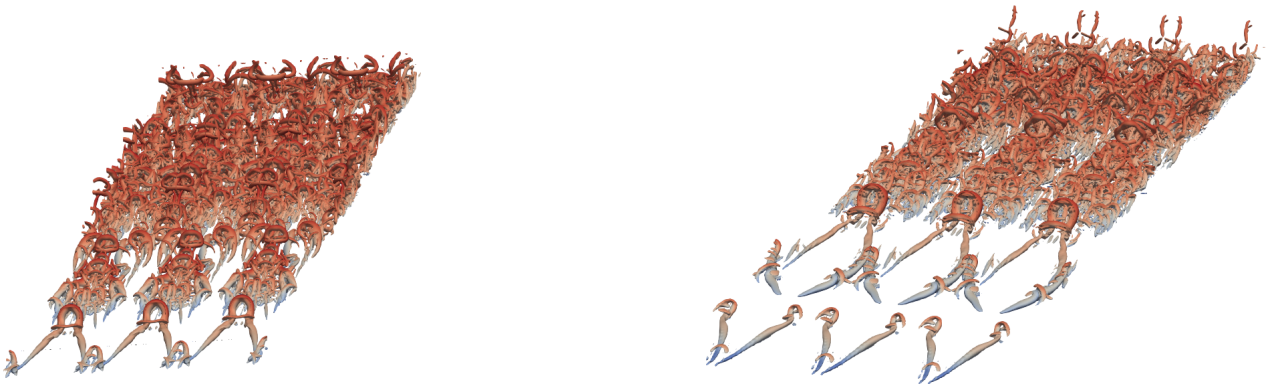

(a) $\Delta x = 0.075$. (b) $\Delta x = 0.15$.

Figure 4.14: Representation of the second invariant of the velocity gradient tensor, Q, coloured by the streamwise velocity. The spanwise length of the computational domain has been replicated three times.

4.4 Additional frequency components

The amplitude of the second and third harmonics is at least one order of magnitude smaller than the amplitude of the fundamental harmonic when using an ideal gas law. However, this difference in amplitudes is not observed when using the Van der Waals EoS with a transcritical boundary layer, where the amplitudes of the higher harmonics become comparable to the fundamental harmonic. As

shown on the stability diagram in Fig 4.15, the higher harmonics $F_2 = 220 \cdot 10^{-6}$ and $F_3 = 330 \cdot 10^{-6}$ excite both Mode I and Mode II in the study area. These harmonics play, thus, a significant role in the development of turbulence. It is therefore essential to find a method that reduces their amplitudes to a negligible level.

To investigate the origin of these harmonics and rule out the possibility of numerical parameters on their nonlinear growth, a comprehensive analysis is conducted. The study examined the impact of various factors, including the sampling frequency, mesh quality, amplitude of the blowing/suction wave, and the influence of the sponge area at different boundaries. To expedite computational time, the analysis of these harmonics will be performed on a two-dimensional domain using the numerical parameters of case *2D Harmonics Study* in Tab 6.1. The complete analysis and convergence study are presented in Appendix E, with the main results summarised here. Then, an implementation of a modified method for introducing these disturbances is carried out to determine if the forcing wave is responsible for the observed high amplitudes.

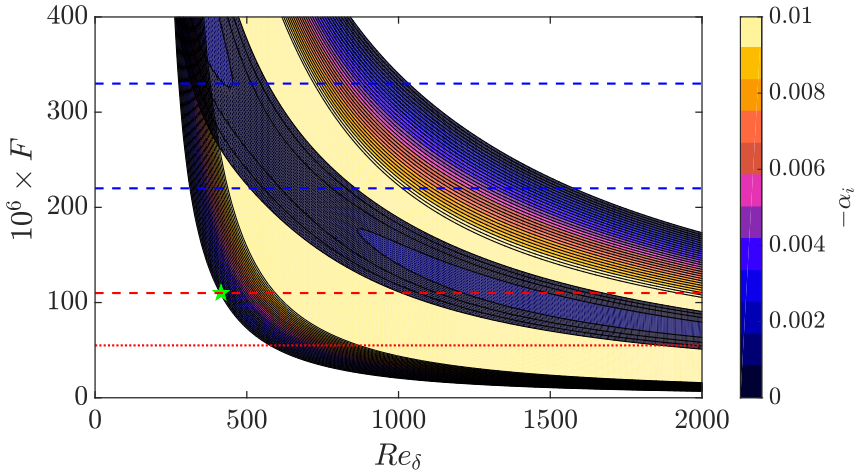

Figure 4.15: Linear stability curve for the transcritical simulations, where the red lines represent the fundamental and subharmonics, and the blue lines represent the second and third harmonics.

The analysis indicates that using 10 samples per wave is sufficient to capture the fundamental harmonic but not the second and third harmonics, while using 15 samples can capture the second harmonic, and at least 20 samples are required to capture both the second and third harmonics. Since this study focuses on the first three harmonics, 20 samples will be used. Increasing the number of samples to capture these harmonics was expected from the Nyquist-Shannon theorem [133].
Similarly, the study of mesh quality reveals that a relatively coarse mesh in the streamwise direction is sufficient to accurately capture the fundamental harmonics, but as the number of higher harmonics to be captured increases, the number of grid points must also increase. This is evident, as the frequency of the phenomenon being studied increases, it becomes necessary to use a grid with smaller spacing in order to properly capture the higher frequency components. Furthermore, an investigation of the top sponge area shows that the sponge length and strength have minimal effect on the amplitude of the second and third harmonics. This finding suggests that the sponge area does not contribute to the nonlinear growth of these harmonics. The determination of the optimal computational domain with minimal error resulting from the grid, domain size, and other parameters corresponds to the case *2D Harmonics* in Tab 6.1.

The amplitude of the forcing wave remains the most crucial parameter in this study. To assess its effect on the harmonics present in the response, the amplitude is increased from $A = 10^{-8}$ to 10^{-2}. The amplitude of the various harmonics using 10^{-4} and 10^{-6}, normalised by the forcing amplitude depicted in Fig 4.16, reveals that in the initial region of the domain, the amplitude of the second harmonic is three orders of magnitude smaller than the fundamental harmonic when using 10^{-4}, whereas it is five orders of magnitude smaller when using 10^{-6}. However, when the amplitude of the forcing wave is increased to $A = 10^{-2}$, the response of the system is highly nonlinear and unsatisfactory. The large difference, in Fig 4.16, quickly decreases through the domain such that the amplitude of those harmonics becomes not lower than two orders of magnitude at $Re_\delta = 475$ using 10^{-4} and at $Re_\delta = 650$ using 10^{-6}. Further investigation into the impact of the streamwise grid spacing during a transcritical simulation, while maintaining the same forcing amplitude, would be required as the outcomes obtained using 10^{-6} display a noticeable amount of noise, indicating the requirement for a greater number of points. While reducing the amplitude of the forcing leads to a decrease in the amplitude of the different harmonics, it necessitates an increase in the number of points and, consequently, computational cost. Despite this, the harmonics persistently retain their significance even with 10^{-6} for Reynolds numbers larger than $Re_\delta = 700$.

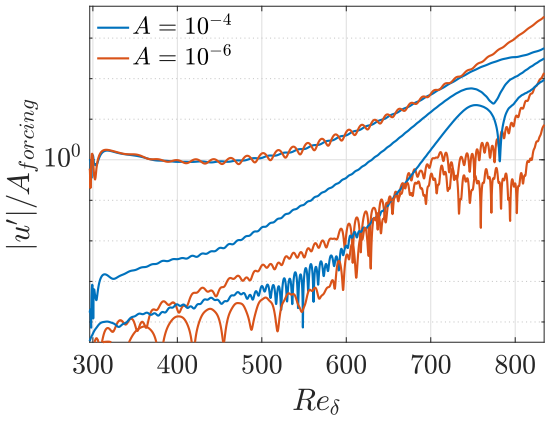

Figure 4.16: Representation of the first three harmonics present in the response for an amplitude of 10^{-6} ans 10^{-4} during a $2D$ transcritical simulation normalised by the forcing amplitude.

In conclusion, the studies conducted in this analysis reveal that the large amplitude of the different harmonics is not influenced by the mesh quality or sponge configuration. While the forcing has some effect on the initial amplitude of these harmonics, they quickly become non-negligible. A recently discovered technique will be introduced to replace the blowing/suction wave.

Modification of the perturbations

This method, proposed by Wasisto *et al.* [134], replaces the blowing/suction waves by adding the eigenfunction of the perturbation, computed from the LST, to the velocity and temperature profiles at the inflow boundary as represented in Fig 4.17.
For a $2D$ domain using the parallel flow assumption, the perturbation takes the form

$$q'(0, y, t) = \tilde{q}(y) \cdot e^{i(\alpha x - \omega t)},$$

where α and ω represent the prescribed wavenumber and frequency, respectively. This perturbation vector is added to the base flow, $\bar{q}$, as

$$q = \bar{q} + \varepsilon q'$$

where ε is a weighting factor which monitors the amplitude of the disturbances induced in the flow.

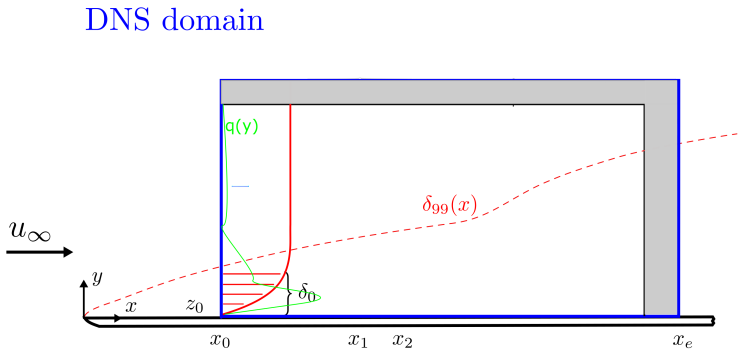

Figure 4.17: Representation of the 2D computational domain with the eigenmode of the perturbation (in green) introduced in the base flow at the inlet. Note that the scaling is not preserved and that no sponge is located at the inlet.

The LST, using the physical parameters stated in case *2D Harmonics* in Tab 6.1, with $Re_{\delta;start} = 250$ and $F_1 = 100 \cdot 10^{-6}$ gives

$$\alpha = \alpha_r + i\alpha_i = 0.075216 + i0.012919.$$

To determine the optimal amplitude of disturbances in the flow field, the weighting factor ε was varied. The results are shown in Fig 4.18(a). At low Reynolds numbers, the amplitude of the prescribed perturbations at the inlet, when ε is set to 10^{-2}, is too high, causing a quicker increase of the second harmonic. When the value of ε is decreased, a more typical behaviour is observed, with the amplitude of the second harmonic remaining at least one order of magnitude below that of the fundamental harmonics. The most promising results were obtained using $\varepsilon = 10^{-3}$, as the relative difference in amplitude between the fundamental and the second harmonics was found to be the largest.

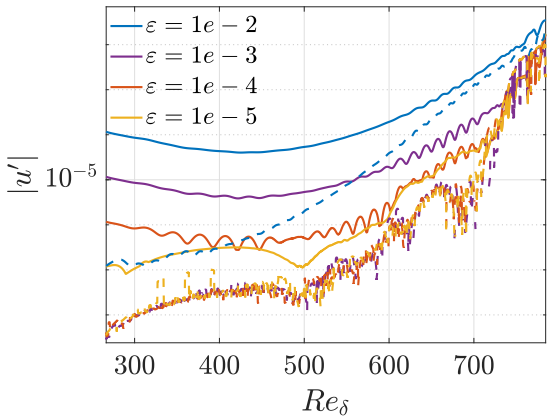

(a) Influence ε.

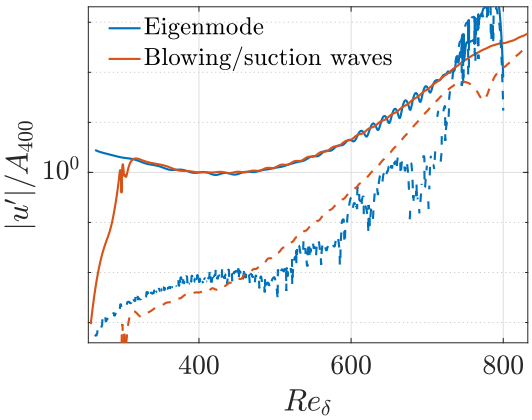

(b) Comparison forcing.

Figure 4.18: (a) Representation of the first two harmonic for various weighting factors ε, $(-)$ represents the fundamental harmonics, while $(--)$ represents the second harmonics. (b) Comparison of the results obtained using blowing/suction waves with an amplitude of 10^{-4} compared to the case using eigenmodes of the perturbation at the inlet. These results have been scaled by their amplitudes at $Re_\delta = 400$.

Fig 4.18(b) compares the results obtained with $\varepsilon = 10^{-3}$ with those obtained using a blowing/suction wave with an amplitude of 10^{-4} rescaled by the value at $Re_\delta = 400$. Both methods show negligible differences in the fundamental wave, except minor oscillations present in the blowing/suction wave method. Surprisingly, the amplitude of the second harmonic obtained with the new technique is very similar to the previous method. The intention was to achieve smaller amplitudes for the different harmonics. This clearly demonstrates that prescribing the eigenfunction of the perturbation rather than a blowing/suction wave does not achieve the objective.

This investigation revealed the presence of unwanted high harmonics that could potentially influence the transition process. To determine whether the blowing/suction wave is responsible for generating these harmonics, the silent inflow condition method was implemented. The results suggest that the presence of these harmonics is independent of the method used to introduce perturbations in the system. This observation is corroborated by the fact that modifying the blowing/suction wave to match the form proposed by Franko & Lele [127] generates harmonics with the same amplitude. However, since these harmonics were equivalent between the different simulations conducted on an equidistant mesh, they should not be responsible for the observed differences in the path to transition.

4.5 Presence of spurious oscillation

The previous simulation exhibited spurious oscillations within the transition region, as shown in Fig 4.19(a). These oscillations have the potential to disrupt the physical transition and contribute to the observed variations. The presence of the Widom line plays a significant role, as these oscillations were not observed in a subcritical simulation or when an ideal-gas law was employed. The observed spurious oscillations is believed to be generated as a result of the numerical schemes used, as explained in Sec 2.3.2, which do not maintain pressure equilibrium ([18] and [17]). Their amplitude decreases when simultaneously refining the grid in the wall-normal and streamwise directions, indicating their nonphysical nature.

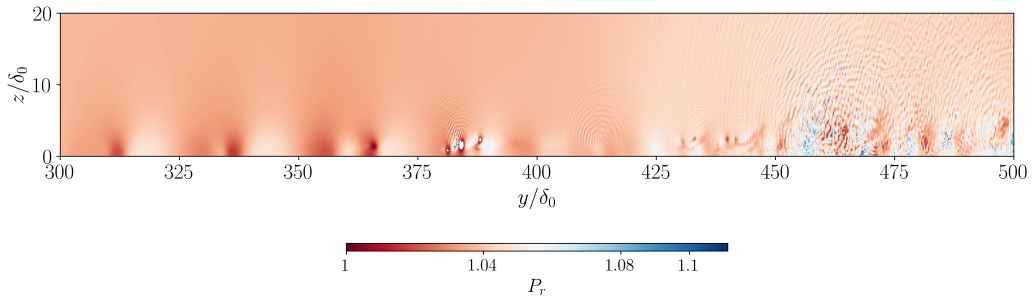

Figure 4.19: Snapshot of the pressure, density, and streamwise velocity fields in the $(x - z)$ planes at $y \approx 0.4\delta_0$

Modification of the numerical scheme

In order to eliminate these spurious oscillations, the numerical KEEP scheme will be modified to ensure the maintenance of pressure equilibrium. The new proposed KEEP scheme, proposed by Shima *et al.* [18], introduces an alternative approach to discretise the numerical flux of internal energy. Instead of splitting the density ρ and the internal energy e as in Eq 2.3.5, their product is discretised as

$$\tilde{I}_j\Big|_{(m\pm\frac{1}{2})} \equiv \frac{(\rho e)|_{(m\pm1)} + (\rho e)|_{(m)}}{2} \frac{u_j|_{(m\pm1)} + u_j|_{(m)}}{2} = \frac{p|_{(m\pm1)} + p|_{(m)}}{2(\gamma-1)} \frac{u_j|_{(m\pm1)} + u_j|_{(m)}}{2}. \quad (4.5.1)$$

The new discrete pressure-evolution equation, derived by substituting Eq (4.5.1) into Eq (2.3.4), cancels out using the ideal-gas law and the assumption of constant pressure and velocity distribution. This new KEEP schemes in a compressible problem using a real-gas EoS, demonstrates superior numerical stability property without introducing any numerical dissipation compared to the previous KEEP schem [18]. A more detailed explanation of the proposed KEEP schemes can be found in [18], which has also demonstrated its efficiency during a 1D advection test under transcritical conditions in the recent study conducted by Capuano [135]. However, even with the use of the new KEEP scheme, the fluctuations are not completely eliminated, but their amplitude is significantly reduced, as shown in Fig **??**. Therefore, this updated method is employed for all subsequent simulations.

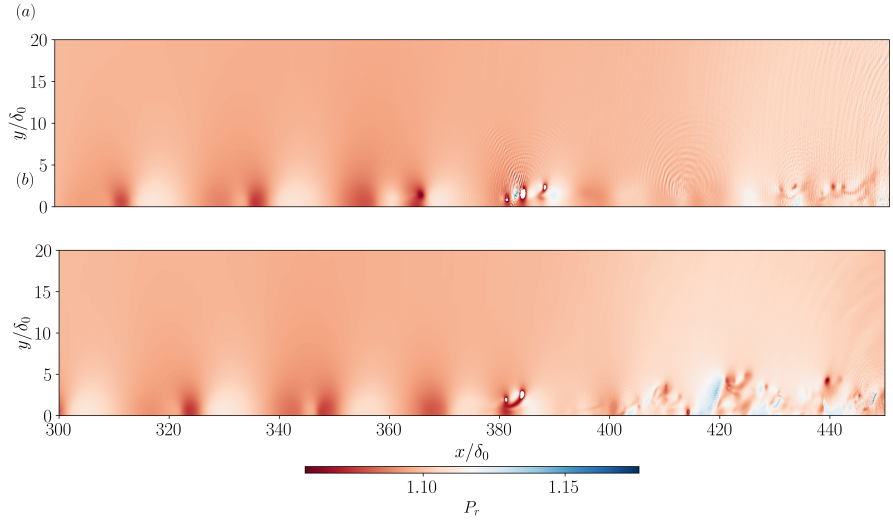

Figure 4.20: Representation of a snapshot of the pressure field throughout the domain using (a) the previous KEEP scheme and (b) the new KEEP scheme.

4.6 Modification of the wall-normal distribution

The lack of convergence when refining only the streamwise direction highlights the importance of analysing the wall-normal distribution. Refining this direction is challenging due to the steep thermodynamic property gradient at the pseudo-critical line, which increases throughout the domain, making it difficult to maintain a consistent level of refinement. This grid distribution is designed to accurately capture the Widom line from the inlet to the outlet of the domain. It is worth noting that in a previous study where a streamwise grid spacing of $\Delta x = 0.3$ was used, a wall-normal grid with $n_y = 250$ points and a stretching factor of 5.8 was found to be sufficient to converge the FFT modes. However, this previous study did not consider the effects of a smaller streamwise grid spacing and therefore was not presented.

Fig 4.21(a) illustrates the position of the pseudo-critical temperature along the flat-plate, normalised by the boundary layer thickness at the inlet δ_0 or the 99^{th} thickness. As the flow progresses through the domain, the location of the pseudo-critical temperature increases with a maximum at $Re_\delta = 700$. However, when the flow transitions to turbulence due to increased mixing, the location

of the pseudo-critical temperature sharply decreases. It is interesting to note that the growth of the pseudo-critical temperature is smaller than the growth of the 99^{th} boundary layer, as evidenced by the negative slope.
Fig 4.21 (b) presents the grid spacing close to the pseudo-critical temperature at different Reynolds numbers using both the previous and the proposed wall-normal distribution. The previous mesh, with 250 points and a stretching factor of 5.8 showed that the grid spacing increased through the domain. For instance, at $Re_\delta = 400$, a grid spacing of $\Delta y = 0.020$ was used, whereas it increased to 0.024 for $Re_\delta = 700$. A new proposed mesh with 420 points and a stretching factor of 10 was suggested, effectively doubling the number of points in the near-wall region (below $y/\delta_0 = 1$). This distribution ensured the accurate capture of the pseudo-critical line, maintaining a uniform grid spacing of $\Delta y = 0.01$ across the entire domain. To address the previously encountered issue, various simulations will be conducted using equidistant grids of 0.15, 0.10, and 0.075 with the numerical and physical parameters of case *3D Study Wall normal* in Tab 6.1.

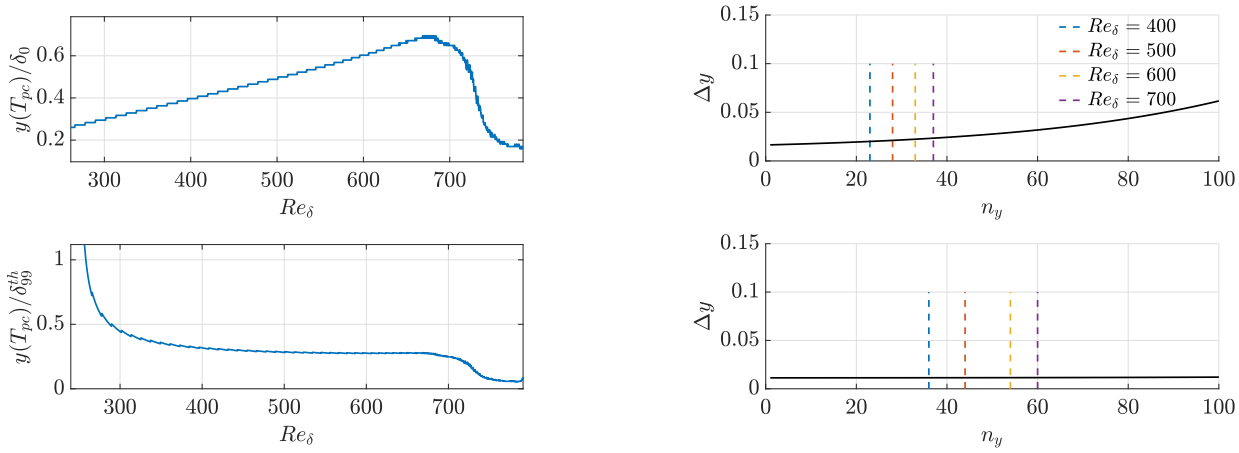

(a) Pseudo-critical temperature.

(b) $n_y - \Delta y$.

Figure 4.21: (a) Evolution of the position of the pseudo-critical temperature in the wall-normal direction normalised by δ_0 or $\delta^{99}(x)$. (b) Representation of the grid spacing in the wall-normal direction for the two wall-normal distribution (*3D Study Grid Equid* and *3D Study Wall normal*) in Tab 6.1. The dotted lines correspond to the position of T_{pc} along the wall-normal distribution for the specified Reynolds numbers.

Fig 4.22 illustrates the development of various eigenmodes and their corresponding skin-friction coefficients using both the previous and the new wall-normal distributions. The additional refinement, which ensures having 100 grid points within $y/\delta_0 < 1$, accelerates the increase of the oblique mode for both meshes with $\Delta x = 0.15$ and 0.10. The similarity in the results is further confirmed by the close match observed in the C_f computed on those meshes. The friction coefficient is almost identical regarding the location of the transition, the growth rate and the amplitude of the overshoot. These findings indicate that the additional near-wall refinement has a significant impact on the oblique modes. However, further refinement with a grid spacing of $\Delta x = 0.075$ leads, once again, to abnormal behaviour as the closest match is observed with 50 points in the near-wall region compared to 100. It is very intriguing that the results with the finer meshes in all directions give similar results as the two coarser meshes in the wall-normal direction.

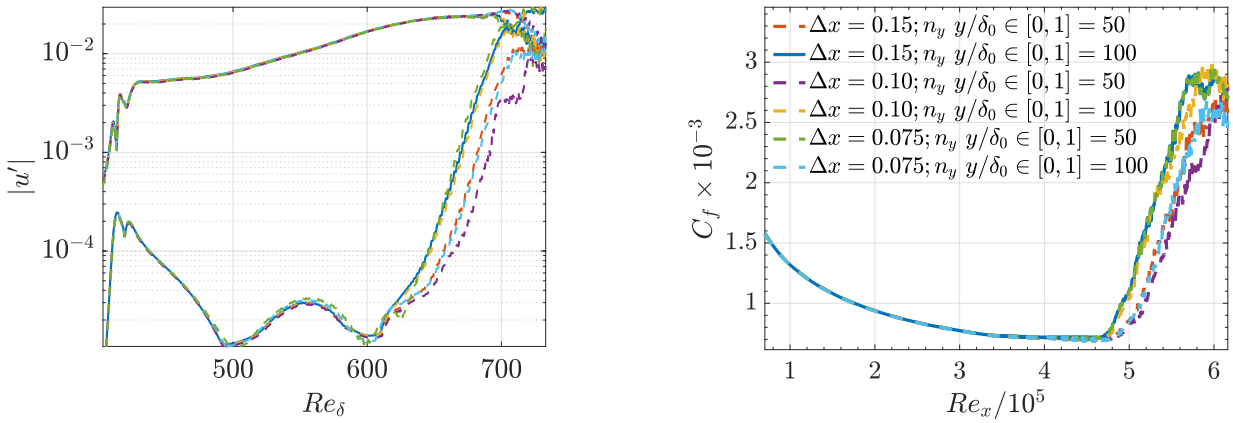

(a) FFT modes. (b) C_f.

Figure 4.22: (a) Representation of the fundamental $2D$ mode $(\omega_0, 0)$ and the oblique mode $(\omega_0/2, \beta)$. (b) Representation of the corresponding skin-friction coefficient.

4.7 Modifications solving the convergence issue

Due to the limited available computational resources, further refinement of the grid in all spatial directions is not feasible. As a result, alternative approaches need to be explored to bypass the convergence issue. Either increasing the reduced pressure to mitigate the significant gradients in thermodynamic properties at the pseudo-critical point or decreasing the Mach number to eliminate any impacts arising from acoustics of compressibility effects.

4.7.1 Increase of the pressure

The variation of the thermodynamic properties reveals a smoother gradient in the vicinity of the pseudo-critical temperature when the pressure increases, as shown in Fig A.2. The convergence analysis will be performed using the thermodynamic quantities corresponding to case *Transcritical 1* in Tab 4.4.

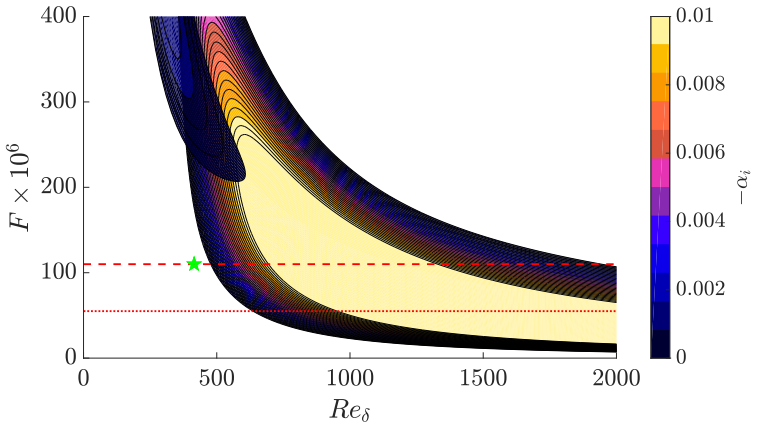

Figure 4.23: Representation of the linear stability curve for the reduced pressure $P_r = 1.1$. The red dotted line in the linear stability curves represents the fundamental frequency $F_1 = 110$ and the subharmonic frequency $F_2 = 55$. The pentagram shows the middle of the disturbance strip.

Additionally, modifying the reduced pressure leads to a change in the pseudo-critical temperature. At $p^*/p_c^* = 1.1$, the pseudo-critical temperature is $T_{pc}^*/T_c^* = T_{pc} = 1.014$ [61]. After non-dimensionalisation by T_∞^*, it reveals that the wall temperature must exceed $T_{pc} = 1.102$, to obtain a transcritical boundary layer, which is the case. The increase in the free-stream reduced pressure results in a modification of the stability curve, shown in Fig 4.23. The main difference is the introduction of perturbations (represented by the green pentagrams) located in a stable region. Additionally, using this pressure while keeping the same fundamental and subharmonic frequencies enables exclusive excitation of Mode II across the entire domain.

parameter	Transcritical 1
$p_r = \frac{p_\infty^*}{p_c^*}$	1.1
$T_r = \frac{T_\infty^*}{T_c^*}$	0.92
$T_{w;r} = \frac{T_w^*}{T_c^*}$	1.08
$T_w = \frac{T_w^*}{T_\infty^*}$	1.18

Table 4.4: Thermodynamic parameters used in the different transcritical simulations with an increasing reduced pressure.

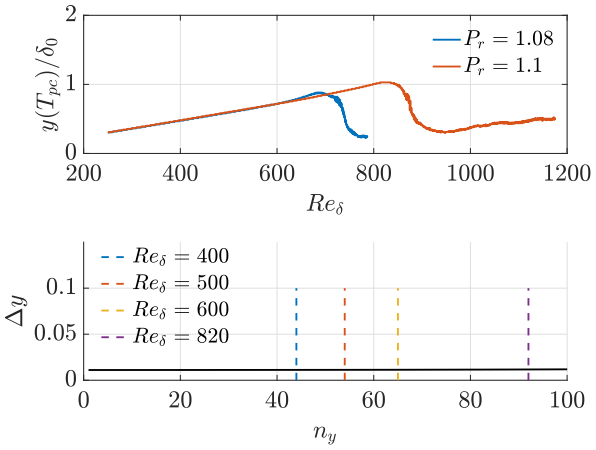

Figure 4.24: The position of the pseudo-critical temperature in the wall-normal direction for various reduced pressures and the grid spacing used at those positions at different Reynolds.

The positions of the pseudo-critical temperatures in the wall-normal direction are shown in Fig 4.24. With the higher reduced pressure, the slope exhibits a prolonged growth, indicating a delayed onset of the unstable region. Consequently, the transition to turbulence will occur further downstream. Fig 4.24(b) demonstrates that the same wall-normal distribution is sufficient to accurately capture the Widom lines, even for the maximum located at $Re_\delta = 820$. A brief investigation will be carried out to examine the impact of different streamwise grid spacings ($\Delta x = 0.25$, 0.15, and 0.075) using an equidistant distribution. The simulations will be conducted with the numerical and physical parameters specified in case *3D Pr1 1* in Tab 6.1.

Δx	ε [%] $(\omega_0, 0)$	ε [%] $(\omega_0/2, \beta)$	ε [%] $(\omega_0/2, 2\beta)$
0.25	0.19	4.7	6.9
0.15	0.02	0.05	0.72

Table 4.5: Relative errors of the different FFT modes for Re_δ ranging from 450 to 850.

The obtained FFT modes, depicted in Fig 4.25, reveal the convergence of the two finest equidistant grids by the overlap of all modes. To confirm the convergence, the relative errors of the fundamental and two oblique modes were calculated with respect to the finest grid, and the results are presented in Tab 4.5. The significant decrease in relative error observed for both oblique modes when using $\Delta x = 0.25$ to $\Delta x = 0.15$ indicates that convergence has been achieved. Subsequently, the skin-friction coefficient in Fig 4.25 exhibits a nearly perfect collapse for the transition location, the growth rate, and the amplitude of the overshoot. Through this study, it is revealed that increasing the free-

stream pressure smoothes the gradients in thermodynamic quantities, which, in turn, leads to improved convergence in the simulations.

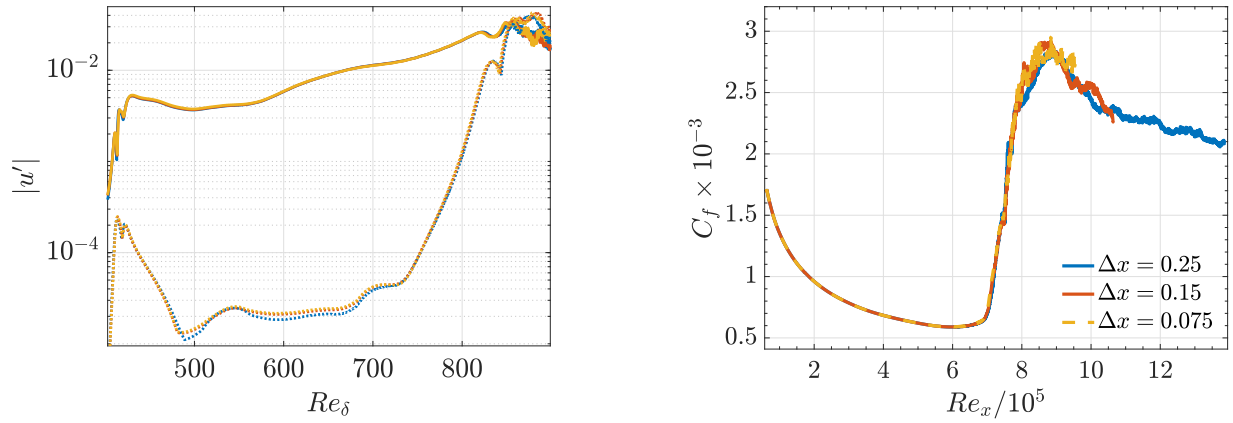

(a) FFT modes. (b) C_f.

Figure 4.25: (a) Representation of different FFT modes obtained with different streamwise mesh refinements. $(-)$ represents the mode $(\omega_0, 0)$, $(..)$ represents the mode $(\omega_0/2, \beta)$, $(--)$ represents the mode $(\omega_0/2, 2\beta)$. (b) Representation of the skin-friction coefficient.

4.7.2 Decrease of the Mach number

To ensure that the convergence issue with the use of $P_r = 1.08$, is not resulting from compressibility or acoustic effects, the free stream Mach number will be reduced to 0.1, resulting in an Eckert number of 2.8×10^{-3}. Previous studies have shown that employing a small Mach number enhances the numerical stability of simulations, leading to accurate and dependable results [136]. The same grid analysis used for the case referred to as *3D Study Wall normal* will be employed. Also, note that decreasing the Mach number does not lead to a modification of the temperature, density or viscosity profile. Note that, when the free-stream Mach number is decreased, it becomes necessary to reduce the time step in order to maintain compliance with the CFL condition [137].

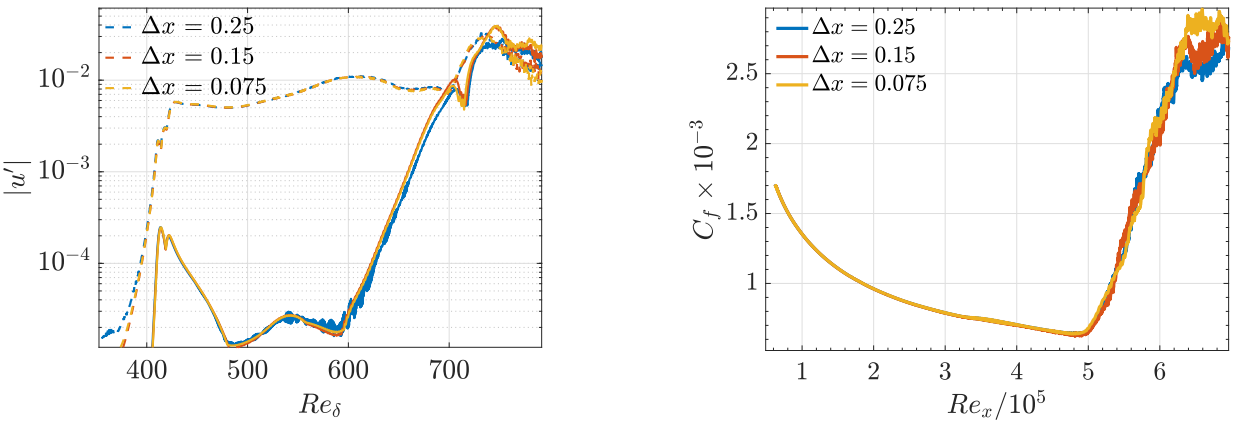

(a) FFT modes. (b) C_f.

Figure 4.26: (a) Representation of different FFY modes obtained with different mesh refined in the streamwise direction. $(--)$ represents the mode $(\omega_0, 0)(-)$ represents the mode $(\omega_0/2, \beta)$. (b) Representation of the skin-friction coefficient.

The different FFT modes for various refinements in the streamwise direction are shown in Fig 4.26(a). By reducing the free stream Mach number, it becomes possible to achieve a collapse of the oblique mode in the two finer meshes, which was not attainable with $M = 0.4$. The coarser mesh exhibits slight variations in the location where the oblique mode initiates growth. However, this mesh is inadequate, as evidenced by the presence of oscillations in this low amplitude mode. To highlight the convergence of the mesh, the relative errors for both excited modes with respect to the finer grid are presented in Tab 4.6. The reduction of the error on the oblique mode from 3% to 0.3% indicates convergence. The skin-friction coefficient presented in Fig 4.26(b), exhibits, therefore, a similar behaviour for all meshes. They all predict a transition at $Re_x = 5 \cdot 10^5$ with an equal growth rate for the C_f (which comes from an equal growth rate of $(\omega_0/2, \beta)$). Minor differences in the amplitude of the overshoot can be observed, along with the presence of oscillations in the curves as the flow intermittency increases. These discrepancies are attributed to the averaging process conducted over only five periods, whereas it appears that a larger number of periods is necessary for a more accurate representation.

Δx	ε [%] $(\omega_0, 0)$	ε [%] $(\omega_0/2, \beta)$
0.25	0.33	3.12
0.15	0.2	0.34

Table 4.6: Relative errors of the different FFT modes computed on a mesh refined in the streamwise direction for Mach = 0.1. The errors are computed with respect to the finest grid for Re_δ ranging from 400 to 650.

4.8 Numerical settings

The sensitivity analysis of the parameters reveals the challenges in achieving a simulation that is entirely free from numerical errors. The lack of convergence observed when using a reduced pressure of $P_r = 1.08$ necessitates either increasing the free-stream pressure or decreasing the Mach number. The final numerical settings, which will be utilised in the subsequent section analysing the influence of various physical parameters, are provided in Tab 4.7.

$L_{\text{sp;inlet}}$	$L_{\text{sp;outlet}}$	$L_{\text{sp;top}}$	σ	L_z	Δz	L_y	S_f	n_y	Δx
20	20	13.33	1	9.63	0.15	40	10	420	0.15

Table 4.7: Values of the numerical parameters, determined from the parameter analysis, used in Chapter 5.

Chapter 5

Investigation of flow conditions on the breakdown

The preceding chapter provides the means to identify the optimal numerical parameters that guarantee a simulation with negligible numerical errors when employing a free-stream reduced pressure of 1.1 or a Mach number of 0.1. The numerical parameters determined in Tab 4.7 will be employed throughout this chapter to analyse the influence exerted by various physical parameters on the transition behaviour and turbulent statistics of a boundary layer. These parameters include the wall temperature, free-stream pressure, and Mach number.

5.1 Subcritical and transcritical boundary layer

To analyse the difference between a transcritical and subcritical boundary layer transition, three simulations are performed using the numerical and physical parameters corresponding to case *3D Grid Study Grid Equid* in Tab 6.1 and the thermodynamic properties given in Tab 5.1. In the simulation labelled as *sub 1*, the fluid experiences cooling from the plate. In contrast, the simulation *sub 2* has a wall temperature similar to the free-stream, while the third one, *transcritical*, has a wall temperature to generate a transcritical boundary layer. The mean density profile in the laminar region is represented in Fig 5.1. This figure reveals the small density gradients in a subcritical boundary layer compared to the transcritical simulation. It should be noted that the mean density $\bar{\rho}$, calculated using a wall temperature equal to the dimensionless free-stream temperature, does not remain exactly equal to 1 due to the higher Mach number and the resulting compression of the flow.

The different linear stability curves shown in Fig 5.2 reveal that the perturbations are introduced within the unstable regions for all simulations but with a different growth rate, which is of the order of 10^{-4} in the transcritical simulation. The two stability curves observed in both subcritical simulations show that the unstable Mode I is stronger and broader for a lower wall temperature. In particular, for the fundamental frequency, the unstable range is slightly broader using a cold wall, spanning from $Re_\delta = 380$ to 680 compared to $Re_\delta = 400$ to 660 for $T_w = T_{cr}$. The LST predicted a delayed transition for the subcritical boundary layer as the wall temperature increased. It is important to note that the presented linear stability curve is $2D$, but an instability curve computed in $3D$ would have shown a similar curve. The growth of different FFT modes, presented in Fig 5.3, supports this prediction. For Reynolds numbers between 500 and 600, the $(\omega_0, 0)$ mode exhibits a mean growth rate of $-\alpha_i = 3.8 \cdot 10^{-3}$ for $T_w/T_\infty = 0.95$ and $3.3 \cdot 10^{-3}$ for $T_w/T_\infty = 1$. This growth rate, during the primary instability, increases to $-\alpha_i = 7.7 \cdot 10^{-3}$ when it results from Mode II.

	sub 1	sub 2	transcritical
$p_r = \frac{p^*_\infty}{p^*_c}$	1.08	1.08	1.08
$T_r = \frac{T^*_\infty}{T^*_c}$	0.92	0.92	0.92
$T_{wall;r} = \frac{T^*_w}{T^*_c}$	0.87	0.92	1.08
$T_{wall} = \frac{T^*_w}{T^*_\infty}$	0.95	1	1.18

Table 5.1: Thermodynamic parameters used in the different simulations.

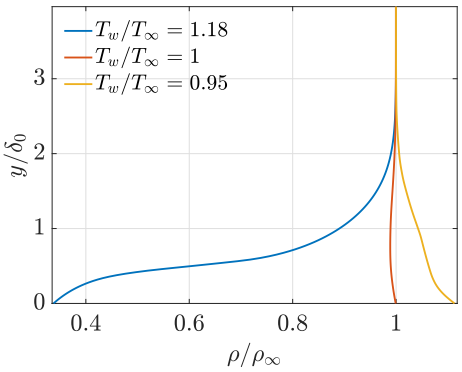

Figure 5.1: Evolution of the mean density along the wall-normal direction for various wall temperatures.

This observation confirms the stronger instability of Mode II, but it occurs at higher Reynolds numbers as a plateau is first observed ranging from $Re_\delta = 420$ to 500. These different growth rates of the fundamental mode result in a delayed secondary instability. Specifically, the oblique modes start to exhibit the highest growth at Reynolds numbers of 575, 580, and 610 for $T_w/T_\infty = 0.95$, 1, and 1.18, respectively. This analysis reveals that increasing the wall temperature delays the transition, as observed in the work of Ren *et al.* [138]. Notably, the slope in the exponential growth of this mode during the secondary instability exhibits a comparable pattern to that of the fundamental mode, with a decrease observed in the subharmonic simulation. Specifically, the values decrease from 0.0633 to 0.054 for $T_w/T_\infty = 0.95$ and $T_w/T_\infty = 1$, respectively. While, the rate increases to 0.097 in the transcritical simulation.

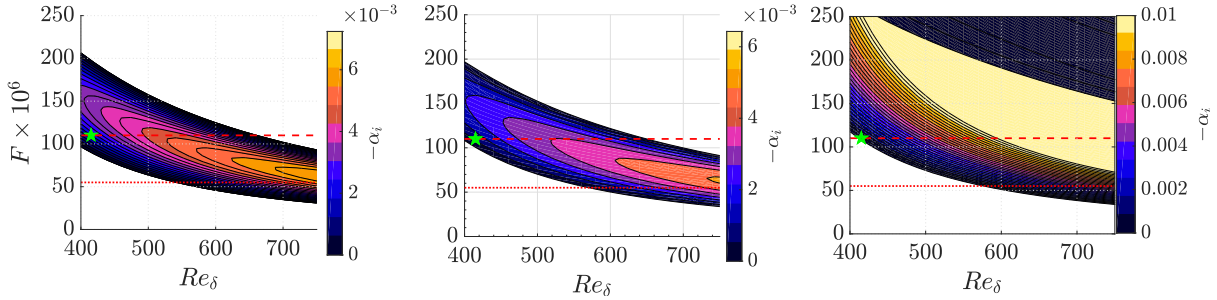

(a) $T_w/T_\infty = 0.95$. (b) $T_w/T_\infty = 1$. (c) $T_w/T_\infty = 1.18$.

Figure 5.2: Representation of the linear stability curve for different wall temperature. The red dotted lines show the fundamental frequency $F_1 = 110 \cdot 10^{-6}$ and the subharmonics frequency $F_2 = F_1/2 = 55 \cdot 10^{-6}$. The green pentagram represents the middle of the disturbance strip.

The evolution of the skin-friction coefficient, shown in Fig 5.4, shows a good correlation between the results of the subcritical simulations and the Blasius solution [113] in the laminar region, and with 1/7 power law in the turbulent region. Furthermore, the skin-friction coefficient resulting from the transcritical simulation also demonstrates good agreement with the theoretical correlation. The transition location, indicated by a dashed line in Fig 5.3, represents the position where the amplitude of the oblique mode reaches a critical threshold triggering spanwise interaction. The ratio between these amplitudes at this position ranges from 15% to 20% for all simulations. This ratio signifies a critical point where the shear stress at the wall begins to increase due to the breakdown of coherent structures. The growth rate of the skin-friction coefficient in the transition region decreases from $\Delta C_f/\Delta Re_x = 3.95 \cdot 10^{-8}$ to $1.95 \cdot 10^{-8}$ for $T_w/T_\infty = 0.95$ and $T_w/T_\infty = 1.18$, respectively. However,

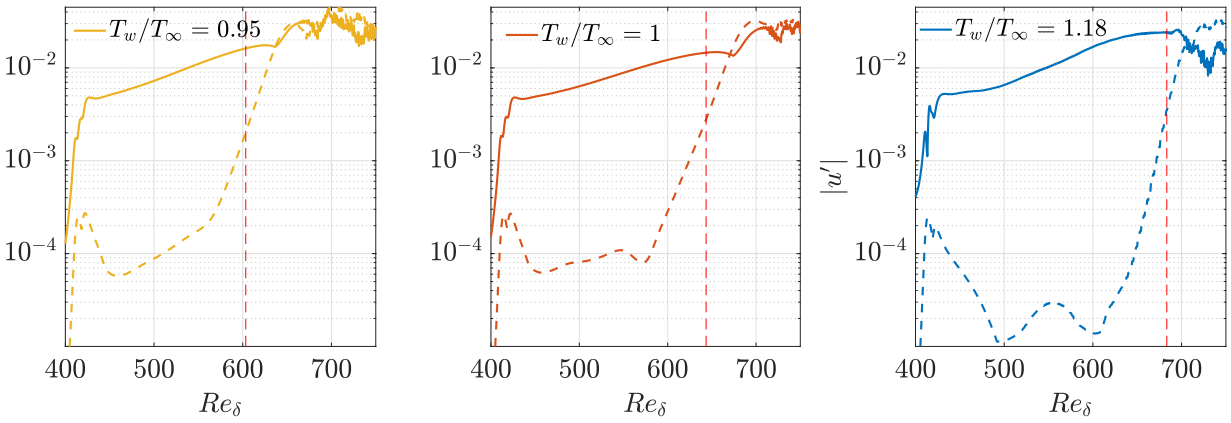

Figure 5.3: Representation of the FFT modes $(\omega_0, 0)$ and $(\omega_0/2, \beta)$. The red dotted line represents the position where the C_f reaches the minimum value.

despite the larger growth rate for the fundamental and oblique modes, the growth rate of the skin-friction coefficient is much smaller in a transcritical boundary layer. This disparity in growth rates is believed to be the cause of the reduced overshoot observed in the transcritical simulation, in contrast to the prominent overshoot observed in a subcritical boundary layer. It is worth noting that the slope of C_f in the turbulent region remains similar with respect to a given factor.

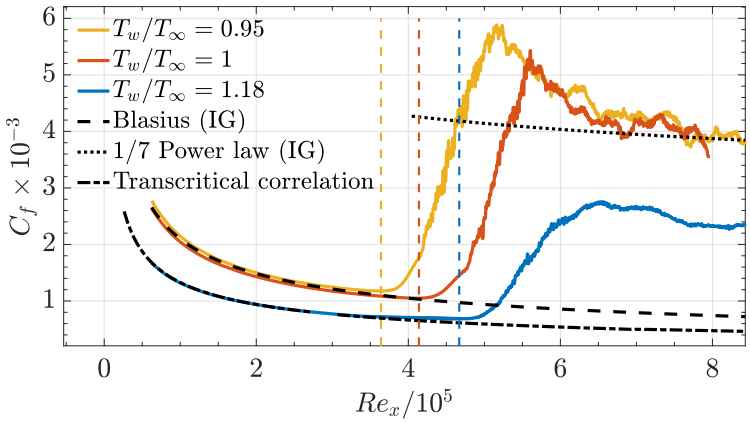

Figure 5.4: Representation of the skin-friction for the subcritical simulations with thermodynamic quantities given in Tab 5.1. The theoretical and empirical correlation for the ideal-gas correspond to the Blasius and 1/7 power law. The correlation for the transcritical simulations is explained Sec C.0.7.

A comparison of the streamwise velocity and density fluctuation profiles, shown in Fig 5.5 and Fig 5.6, extracted at various Reynolds numbers is conducted to highlight the differences between the profiles resulting from Mode I and Mode II. These Reynolds numbers are adjusted to ensure consistency between the subcritical and transcritical simulations. The first profile is taken before the subharmonic mode becomes unstable, at $Re_\delta = 500$ for all simulations. Subsequently, profiles are extracted at $Re_\delta = 600$ in the subcritical simulations and $Re_\delta = 660$ in the transcritical simulation, where the subharmonic modes exhibit the highest growth rate. Finally, the profiles are extracted close to the interaction of both modes, specifically $Re_\delta = 650$ for the subcritical case and $Re_\delta = 700$ for the

transcritical case.
The profiles taken at $Re_\delta = 500$ demonstrate the differences between the fundamental profiles resulting from the primary instability of Mode I or Mode II. The main disparities are observed in the peak positions and the width of the profiles. At the lowest Reynolds number, the profiles extracted from the transcritical simulation exhibit a maximum close to the wall, at $y/\delta_{99} = 0.17$, whereas in the subcritical cases, the peaks occur at $y/\delta_{99} = 0.24$ and $y/\delta_{99} = 0.26$, for T_w/T_∞ values of 0.95 and 1, respectively. The fuller fluctuation profiles in a transcritical boundary layer result from the fuller mean velocity profiles. Another difference is the broader peak observed in the subcritical profiles, characterised by a constant decreasing slope until reaching the minimum at $y/\delta_{99} = 0.9$ and 0.92. In contrast, the profile obtained from the transcritical simulations is much sharper and exhibits a change in the slope, as observed by Wang [52]. This profile shows a shift from a high to low slopes but reaches zero fluctuations at approximately the same location, $y/\delta_{99} = 0.88$, as the other profiles.

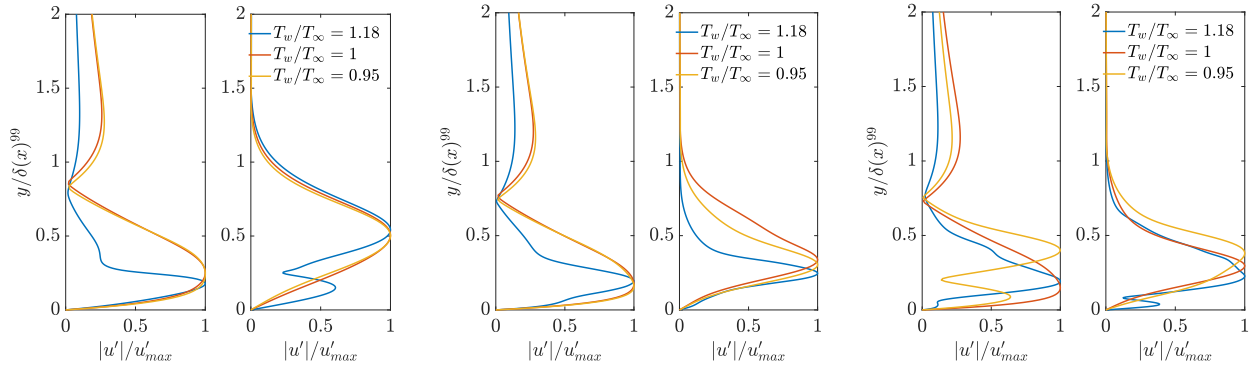

(a) $Re_{\delta;sub} = 500; Re_{\delta;trans} = 500$. (b) $Re_{\delta;sub} = 600; Re_{\delta;trans} = 660$. (c) $Re_{\delta;sub} = 650; Re_{\delta;trans} = 700$.

Figure 5.5: Representation of the streamwise velocity fluctuation profiles of the $2D$ fundamental eigenmode $(\omega_0, 0)$ (left) and the oblique mode $(\omega_0/2, \beta)$ (right) at various Reynolds numbers. All these profiles have been normalised by their maximum values.

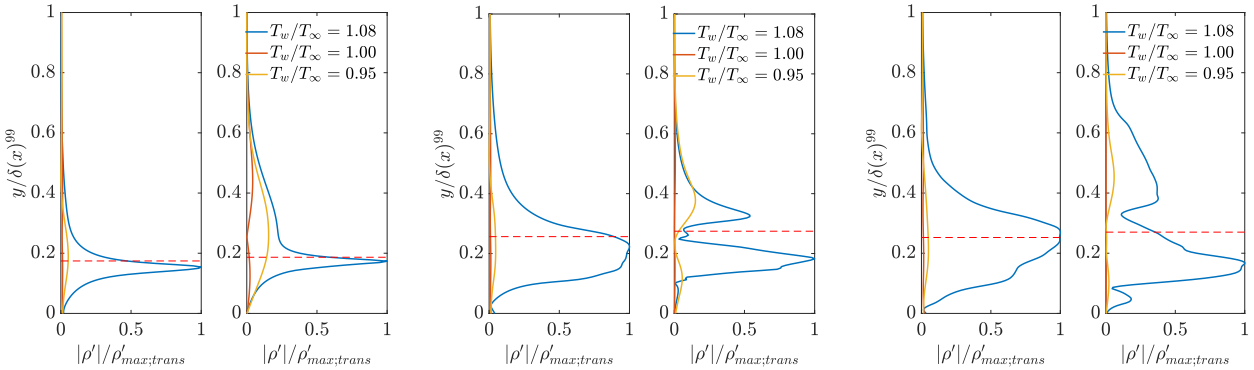

(a) $Re_{\delta;sub} = 500; Re_{\delta;trans} = 500$. (b) $Re_{\delta;sub} = 600; Re_{\delta;trans} = 660$. (c) $Re_{\delta;sub} = 650; Re_{\delta;trans} = 700$.

Figure 5.6: Representation of the density fluctuation profiles of the $2D$ fundamental eigenmode $(\omega_0, 0)$ (left) and the oblique mode $(\omega_0/2, \beta)$ (right) at various Reynolds numbers. All these profiles have been divided by the maximum value in the transcritical boundary layer.

During the secondary instability, in Fig 5.5(b), the position of the maxima in the subharmonic profiles, initially around $y/\delta_{99} = 0.5$, decreases considerably. However, the width of the peak remains broader in a subcritical boundary layer. These differences are believed to result from the sharper

peak observed in the density fluctuation profiles, shown in Fig 5.6, close to the pseudo-critical temperature (red dotted lines), for both modes in the transcritical simulation. It is believed that these density fluctuations influence the streamwise velocity profiles, resulting in peaks with a narrower width. Moreover, it is interesting to note that the density fluctuation profiles in the transcritical case show earlier modifications compared to the streamwise velocity profiles. The profiles extracted during the secondary instability at $Re_\delta = 600/660$ have already undergone significant changes compared to the profiles taken during the primary instability at $Re_\delta = 500$. This suggests that the density undergoes an earlier interaction. The streamwise velocity profiles computed near the modal interactions, shown in Fig 5.5(c), show the modification of those profiles due to their interaction. These include the absence of a zero velocity in the near-wall regions and significantly more undulations in the profile. On the other hand, it can be inferred that the simulations with $T_w = T_\infty$ do not exhibit a transition at this higher Reynolds number, which is consistent with the modal analysis in Fig 5.3.

Fig 5.7 shows instantaneous snapshots of the density in a wall-parallel plane at $y^* \approx 10$. As anticipated based on the C_f and the eigenmodes, the formation of Λ-vortices, indicating the onset of transition, takes place near $x = 300\delta_0$, corresponding to $Re_x = 3.9 \times 10^5$, where C_f is minimal, in the subcritical boundary layer. In contrast, in the transcritical boundary layer, the first vortices are observed closer to $x = 550\delta_0$. The formation of these vortices is thus responsible for the growth of the skin-friction coefficient. The breakdown of the Λ-vortices, which arises from spanwise interactions, seems to occur quicker in the subcritical simulation. In this case, the interaction between vortices, accompanied by their shape deformation, takes approximately $70/\delta_0$ to reach a fully turbulent flow. Conversely, under transcritical conditions, the interaction that leads to the transition into fully turbulent flow takes place around $120\delta_0$. This discrepancy is likely the cause of the smaller growth of the skin-friction coefficient.

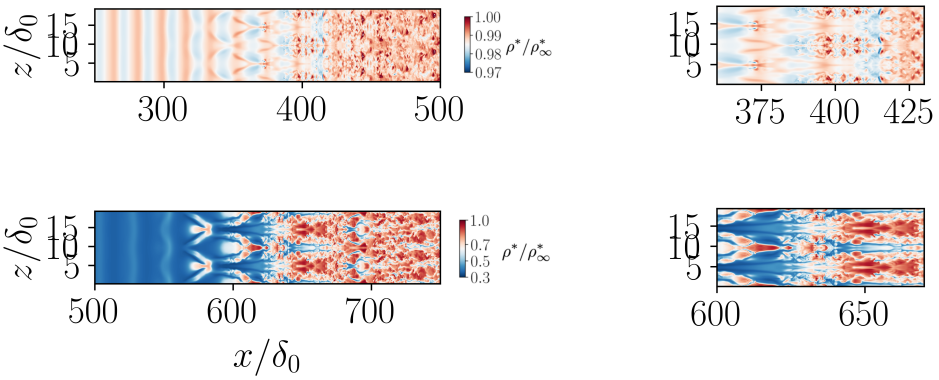

Figure 5.7: Representation of the density fields in the subcritical boundary layer with $T_w/T_{cr} = 1$ (top) and the transcritical boundary layer (bottom).

The density patterns within the transition region, specifically between $x = [600 - 670]\delta_0$ in the transcritical case and $[360 - 430]\delta_0$ in the subcritical case, exhibit notable differences. The variation of density in the spanwise direction is relatively important as it ranges from 1 to 0.3 within the transcritical boundary layer. At $x = 600\delta_0$ and $y = 10\delta_0$, a triangular structure becomes apparent, with a leading edge exhibiting a region of high density (depicted in red). This structure subsequently undergoes breakdown, resulting in the emergence of two high-density regions at $y = 5\delta_0$ and $y = 15\delta_0$, where the fluid exhibits liquid-like behaviour. These regions are separated by a zone of extremely low density at $x = 650\delta_0$, where the fluid exhibits gas-like behaviour. A similar structure is observed in the ideal-gas simulation, appearing at $x = 300\delta_0$ and at $y = 5\delta_0$ and $y = 15\delta_0$. However, the leading edge of this structure exhibits a less pronounced separation between the higher and lower density regions,

and its breakdown occurs more quickly.
Analysing the streamwise velocity fields in the Appendix D.6 reveals that the regions of high density correspond to zones of high streamwise velocity and their breakdown generates two regions of high velocity. These streaks persist for approximately $100\delta_0$ before reaching a fully turbulent flow in the transcritical boundary layer. In contrast, in the ideal-gas case, their separation is maintained for only about $25\delta_0$, highlighting the much faster transition to a turbulent flow when the spanwise interaction begins to occur.

A cross view $(y - z)$ plane representation of the streamwise velocity, density, and temperature fields, along with their respective fluctuations at $x = 650\delta_0$, at the same time as Fig 5.7, is provided in Fig 5.8.

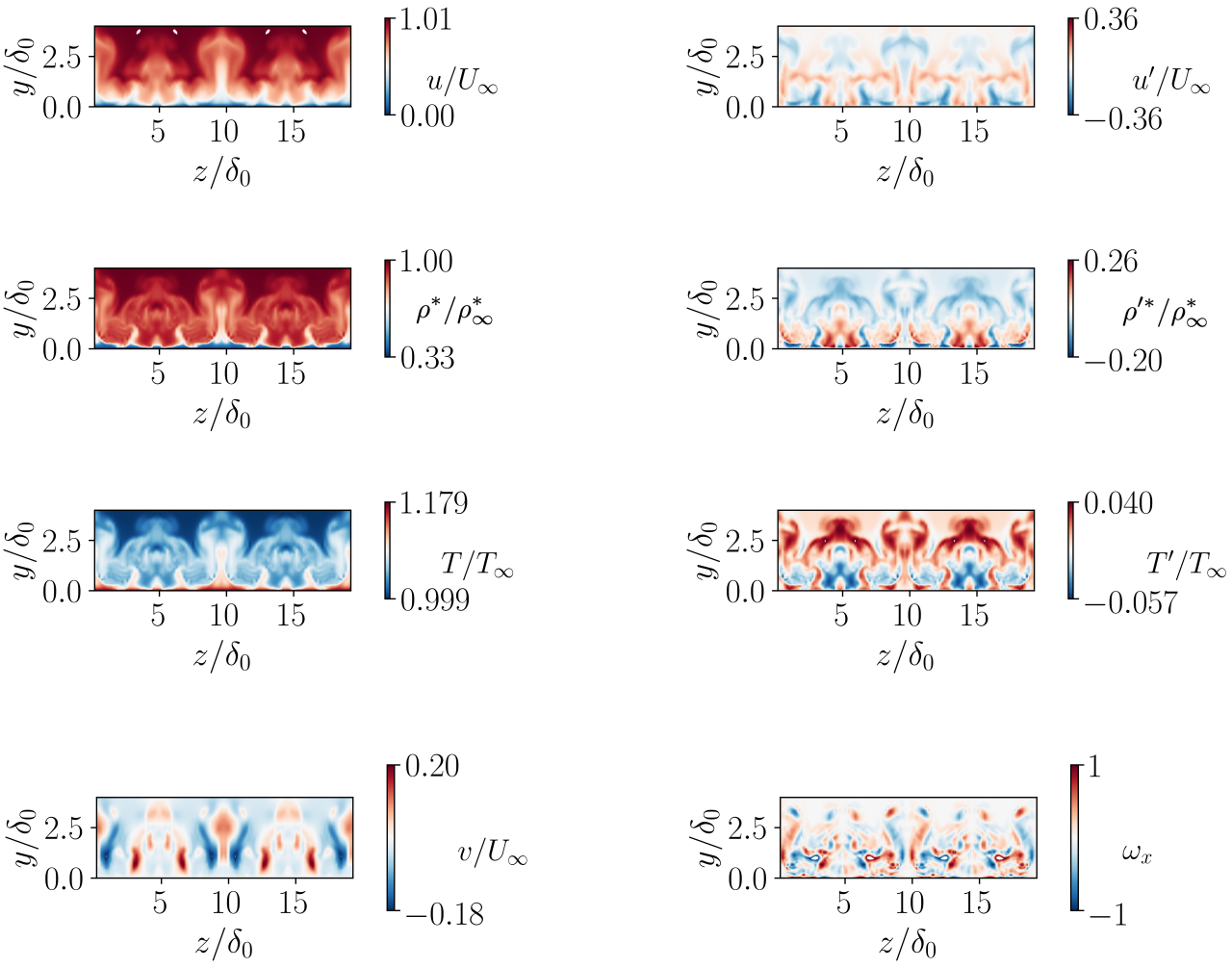

Figure 5.8: Instantaneous cross-view (y-z plane) snapshots of the heated transcritical turbulent boundary layer at $x = 650\delta_0$ in the region of $0 < y/\delta_0 < 3$ and $0 < z/\delta_0 < 19.2$. (a) Streamwise velocity and the fluctuations, (b) density and the fluctuations , (c) temperature and the fluctuations, (d) wall-normal velocity and streamwise vorticity.

In the flow fields, areas of high density correspond to regions of low temperature, indicating a liquid-like behaviour of the flow, and vice versa. The coherent structures can be visualised in the streamwise velocity fields, where regions of lower velocity compared to the surroundings at $z = 10\delta_0$ and $y = 2.5\delta_0$ represent the Ω-vortices. The center of these vortices is associated with zero streamwise vorticity but a high spanwise vorticity, as predicted by theory [2]. The wall-normal velocity fields reveal

the presence of four maxima at $z = 4$, 6, 14, and $13\delta_0$, which correspond to the positions where the two legs of each Λ-vortex lift up. These regions are characterised by a high amplitude of streamwise vorticity, as shown in Fig 5.8(d), attributed to the large velocity gradient around their legs.

The two streaks corresponding to a region of high density and low temperature at $z = 5\delta_0$ and $15\delta_0$ shown in Fig 5.7, exhibit significant fluctuations in temperature and density along the wall-normal direction. These fluctuations result from the spanwise interactions, which enhance the mixing of the flow. However, there is a zone of zero fluctuations located between the two streaks at $z = 10\delta_0$, which separates them. This zone is characterised by a higher temperature and wall-normal velocity compared to its surroundings, but a lower streamwise velocity, as it corresponds to the lifting of the Ω-vortices. From each part of this area, a specific pattern can be observed with positive and negative fluctuations of temperature and density, respectively. In the fluctuation temperature profile, this pattern is characterised by a negative fluctuation amplitude and a two-legged structure. In those legs, the amplitude of the fluctuations increases as one gets closer to the wall. This is due to the large gradient of properties at the pseudo-critical temperature, which is observed in the mean profiles. The combination of the high streamwise vorticity structures, the Λ-vortices, along with the interactions between near-wall turbulence and the Widom line, appears to increase the amplitude of the fluctuations. This phenomenon leads to enhanced flow mixing. These high fluctuations and patterns were not observed in the ideal-gas simulations [139].

5.2 Fluctuations of thermodynamic quantities

The evolution of the Root Mean Square (RMS) value of various thermodynamic quantities in a transcritical boundary layer along the flat-plate is presented in Fig 5.9. An increase in the different quantities is observed along the domain, reaching their maximum amplitude at $Re_x = 5.9 \cdot 10^5$, which coincides with the transition region and corresponds to the skin-friction coefficient becomes larger, in Fig 4.22(b). Those fluctuations were negligible $\approx 2\%$ in the subcritical boundary layer and thus not presented. Subsequently, The maximum amplitudes decrease but remain constant in the fully turbulent flow at $Re_x = 8.1$ and $9.2 \cdot 10^5$ respectively. The maximum RMS values for density and kinematic viscosity are approximately $\sqrt{\overline{\rho'\rho'}}/\bar{\rho}$ and $\sqrt{\overline{\mu'\mu'}}/\bar{\mu} \approx 30$. Regarding specific heat C_p, the variations are even larger and exceed 80%, while the variations in thermal conductivity are negligible, remaining below 10%. These findings highlight the significant fluctuations in these thermodynamic quantities in the transition of a transcritical boundary layer. These fluctuations in density, viscosity, and specific heat are thought to be the cause of the convergence problem. Additionally, the non-negligible density fluctuations invalidate Morkovin's hypothesis [15]. Consequently, the effects of these fluctuations on the log-law and turbulent statistics will be further investigated.

5.3 Influence of the pressure

This section focuses on investigating the influence of free-stream pressure on the transition behaviour of a supercritical boundary layer. Three simulations were conducted, varying the free-stream pressure at values of $P_r = 1.08$, 1.1, and 1.15, while referring to the corresponding wall temperatures specified in Tab 4.4. One should note that the simulation conducted with a free-stream pressure of $P_r = 1.15$ necessitates the modification of various parameters. The linear stability curve shows that this increase of pressure leads to a delay and weakening of the unstable Mode II, and the complete separation of the two modes. Mode I manifest at higher frequencies and lower Reynolds numbers, while Mode II is observed at higher Reynolds numbers and lower frequencies. Consequently, adjustments have been

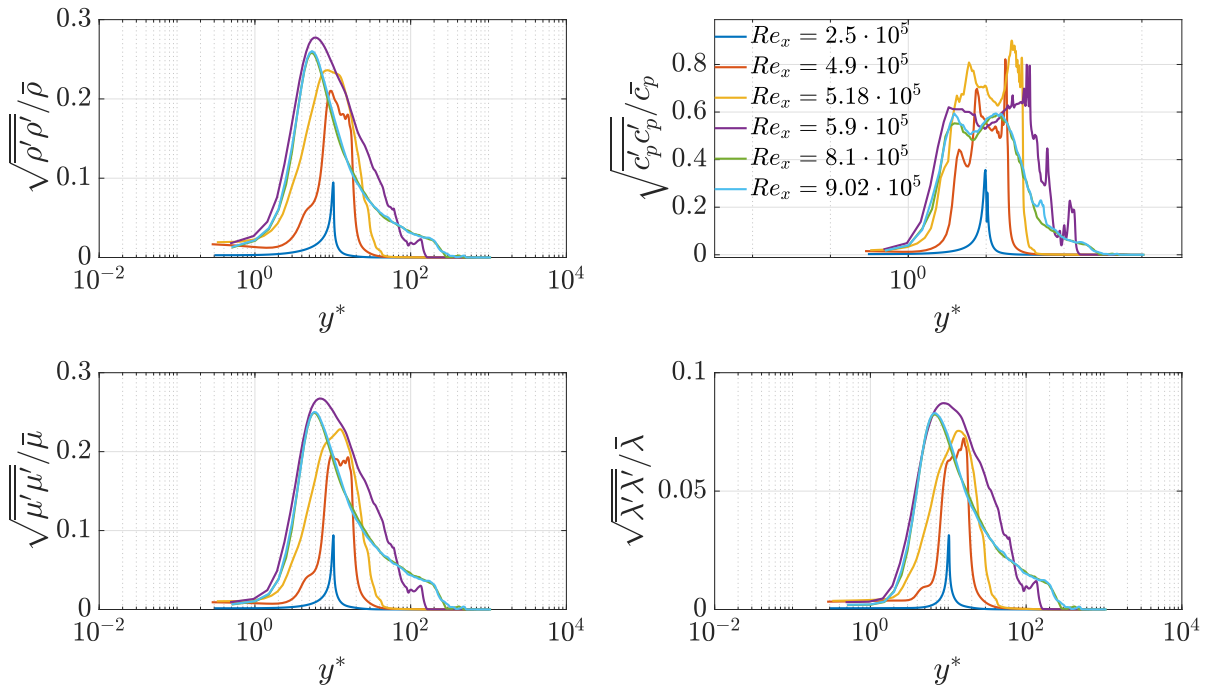

Figure 5.9: Variance of thermodynamic properties in heated transcritical turbulent boundary layers at a supercritical pressure of $p_r = 1.08$.

made to the domain range and excitation frequencies, while maintaining consistent grid spacing in each direction. A detailed explanation and the modal analysis can be found in Appendix F. The numerical parameters used for these simulations are denoted as *3D case Grid wall normal*, *3D Pr 1.1*, and *3D Pr 1.5*, based on Tab 4.7. The primary focus of this analysis is to evaluate the impact of free-stream pressure on fluctuation profiles and the skin-friction coefficient. Furthermore, the study aims to quantify the influence of pressure on root mean square values and their subsequent effects on the mean statistics of a fully turbulent flow.

To ensure consistency among the various fluctuation profiles, the profiles were extracted at different Reynolds numbers. Specifically, these profiles were obtained at $Re_\delta = 550$ for $P_r = 1.08$ or 1.1, and $Re_\delta = 1350$ for the higher pressure case. This selection ensures that each profile is obtained at a position where the amplitude of the oblique mode remains small and negligible compared to the fundamental mode. The fundamental profiles are depicted in Fig 5.10(a), the subharmonic profiles in Fig 5.10(b), and a comparison of the amplitude of the density fluctuation is presented in Fig 5.10(c).

An increase in the free-stream pressure leads to in a broader and elevated position of the peak. For instance, in the fundamental density profile the maximum occurs at $y/\delta^{99} = 0.22$ for $P_r = 1.1$, while for $P_r = 1.15$, it is located at $y/\delta^{99} = 0.37$. This indicates a ratio of 1.6 between the two, which also holds true for the oblique profile. The increase in the maximum position along the wall-normal direction is associated with the rise in the location of the pseudo-critical temperature (depicted with the dotted line) as the simulations conducted with $P_r = 1.15$ operate at larger Reynolds numbers. Furthermore, Fig 5.10(c), where the profiles are normalised by the maximum amplitude using $P_r = 1.08$, reveals that the amplitude of the peak decreases with increasing pressure. In summary, increasing the reduced pressure leads to a decrease in the sharpness and amplitude of the peak. The increased width and

amplitude of the peak can be attributed to smoother variations in property distribution along the wall-normal direction, as illustrated in Fig 2.1. It should also be noted that the peaks differ with the position of the pseudo-critical temperature, and these differences become more pronounced with increasing pressure. When examining the fundamental streamwise velocity fluctuations, it becomes evident that increasing the reduced pressure results in a broader profile. In fact, when $P_r = 1.15$, the minima disappear from the near-wall region below $y = 3\delta^{99}(x)$. However, the maxima are relatively unaffected by this modification. The interpretation of the oblique modes shown in Fig 5.10 is more challenging due to the varying Reynolds numbers. Nevertheless, it is clear that a wider peak is present in these modes as the reduced pressure increases.

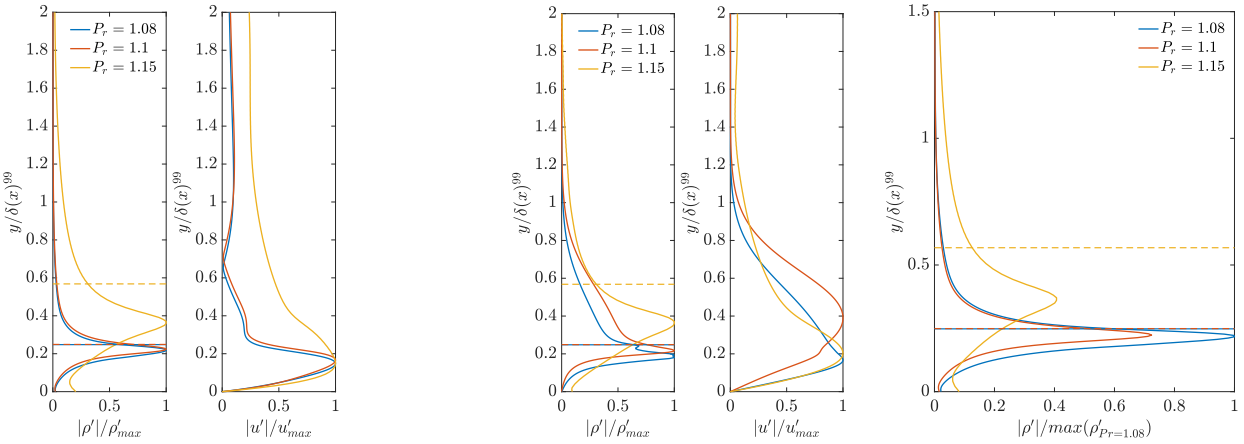

(a) $(\omega_0, 0)$. (b) $(\omega_0/2, \beta)$. (c) $(\omega_0, 0)$ $|\rho'|/\rho'_{max(Pr;1.08)}$.

Figure 5.10: Representation of the fundamental $(\omega_0, 0)$ and oblique $(\omega_0/2, \beta)$ streamwise velocity and density fluctuation profiles at various Reynolds numbers. (a) and (b) are normalised by their maximum value while (c) is normalised by the maximum value using $P_r = 1.08$. The dotted line represents the position of the pseudo-critical temperature.

The delayed transition resulting from an increase in pressure, predicted from the linear stability curves, can be observed in the skin-friction coefficient, as shown in Fig 5.11, as well as in the snapshot of the streamwise velocity in Fig 5.12. The overshoot of the skin-friction coefficient for $P_r = 1.08$ and $P_r = 1.1$ is very similar, with a difference of less than 1%, although slightly higher for $P_r = 1.1$. Both simulations reach their maximum skin-friction coefficient with a relative difference in amplitude of 2%. However, at higher pressures, the growth rate becomes significantly smaller, exhibiting a relative difference of 30% compared to $P_r = 1.1$. Consequently, the amplitude of the overshoot in the skin-friction coefficient is much smaller, with a difference of 12%. This overshoot is, however, small compared to the one obtained during the transition of a subcritical boundary layer. Physically, the increase of the pressure induces the compaction of the fluid, making it more challenging for small perturbations to destabilise and requiring a higher amount of energy.

The formation of Λ-vortices, which are pairs of positive and negative streamwise vorticity, serves as an indicator of the transition process, and their appearance is noticeably delayed with increasing free-stream pressure. For the two presented pressures, the streamwise velocity fields exhibit similarities in terms of the shorter distance it takes for the vortices to interact along the span and undergo breakdown, resulting in a higher level of turbulence within the flow. The amplitude of streamwise vorticity within the Λ-vortices demonstrates similar magnitudes, and the length of these vortices is also relatively comparable, leading to the same flow pattern. For example, a triangular structure is observed twice in the case of $P_r = 1.08$ at $x/\delta_0 = 425$, and once in the case of $P_r = 1.1$ at $x/\delta_0 = 600$. These structures have been previously analysed and found to correspond to a region characterised by high density but

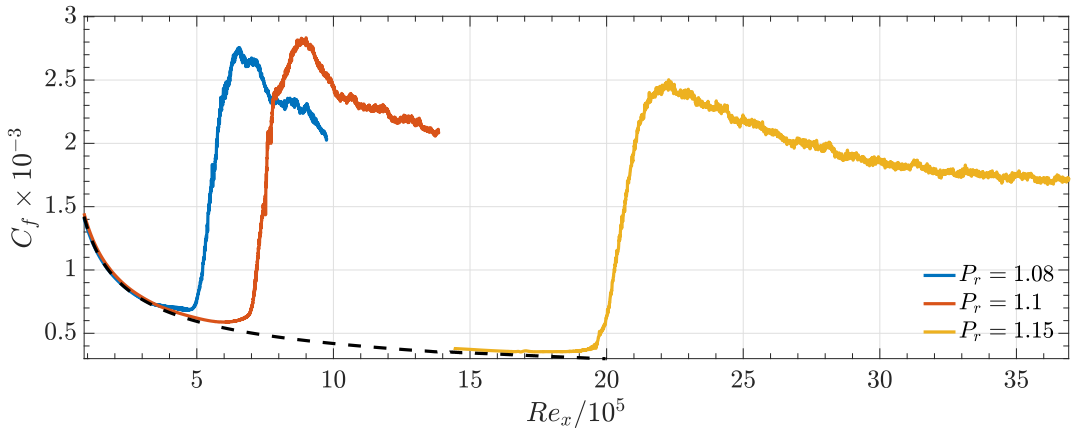

Figure 5.11: Representation of the skin-friction coefficient for different free-stream reduced pressures.

low internal energy, exhibiting behaviour similar to that of a liquid surrounded by a gas-like flow. The result for the highest pressure is not presented as it undergoes transition much later. This observation highlights that as the pressure increases, the flow follows a similar path towards transition, with the same structures appearing. The main difference lies in the position at which the perturbations become unstable and trigger the transition process.

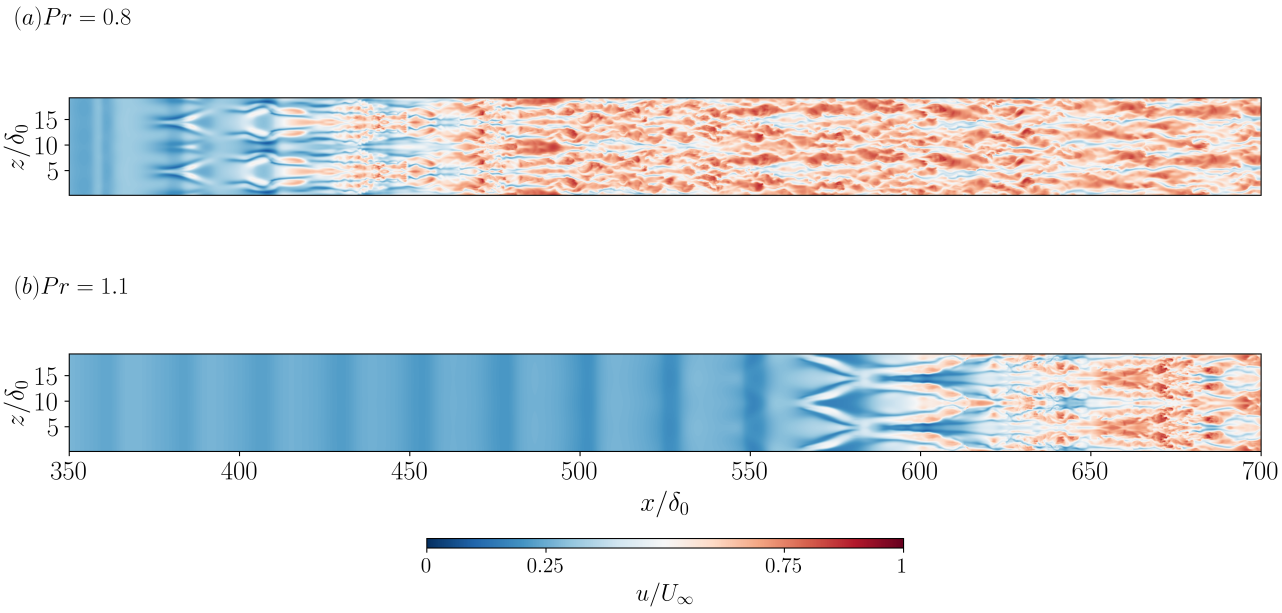

Figure 5.12: Snapshots of the streamwise velocity throughout the domain for various reduced pressures.

Mean turbulent statistics at different pressure

The smoothing effect observed in the sharpness of property variations at the Widom line causes the root mean squared amplitude of density fluctuations to decrease with reduced pressure, as illustrated in Fig 5.13. The maximal value of 0.26 obtained at the lower pressure drops to 0.2 using $P_r = 1.15$. Therefore, higher pressure serves to attenuate these fluctuations. Notably, when using the ideal gas law, the amplitude of density fluctuations becomes negligible. This observation aligns with the expectation

that ideal gas behaviour leads to minimal density fluctuations. The influence of these non-negligible density fluctuations, which render Morkovin's hypothesis [15] ineffective, on the mean velocity profile is shown in Fig 5.13(b) using Van Driest scaling. All profiles exhibit a collapse with the theoretical correlation $u^+ = y^+$ in the viscous sublayer, which highlights the minimal impact of fluctuations in this region. The deviation with the log-law profile, represented by the IG curve, starts from the pseudo-critical temperature (indicated by the dotted lines). In the log-law region ($y^* > 30$), increasing the reduced pressure tends to collapse with the log-law profile of the ideal-gas case. The smaller reduced pressure gives the biggest difference compared to the ideal-gas case, and it tends to increase the log-law region. This can be explained as an increase of the reduced pressure tends to decrease the density fluctuations, it is understandable to tend to the reference case as fluctuations decrease. Moreover, this is interesting as both mean profiles do not exhibit important differences compared to the IG while Van Driest scaling only accounts for the mean density variation within the boundary layer but still works for a transcritical boundary layer where the effect of density fluctuations is not negligible.

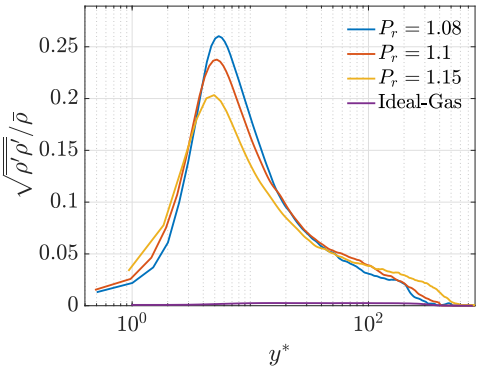

(a) $\sqrt{\overline{\rho'\rho'}/\bar{\rho}}$.

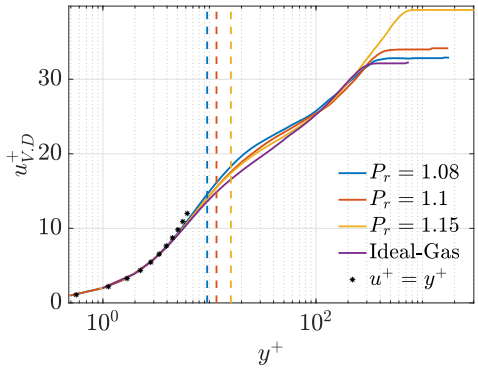

(b) $u^+_{V.D} - y^+$.

Figure 5.13: (a) Evolution of the root mean squared density fluctuations along the wall-normal direction for various free-stream reduced pressures. (b) Evolution of the mean velocity profile using the Van Driest scaling. The dotted lines represent the location of the pseudo-critical temperature. All profiles have been taken from a fully turbulent flow.

The decomposition of the total mean stress into the viscous stress $\overline{\mu \partial u/\partial y}$ and the Reynolds stress $-\bar{\rho}\widetilde{u''v''}$ normalised by the wall shear stress is represented in Fig 5.14. In all cases, the viscous stress collapses well in the log-law region but some non-negligible differences are noticed in the viscous sublayer and buffer layer where the strong variations of properties appear. Similar to the mean velocity profiles, the stress profiles also exhibit a tendency to collapse towards the reference curve computed with the IG model as the pressure increases.

The Reynolds stress reveals an increase in amplitude with reduced pressure, indicating a difference in peak amplitude and position that suggests the absence of universal scaling, as explained by Wu *et al.* [140]. From a zoom in the near-wall region ($y^* < 15$) in Fig 5.14(b), it can be observed that the amplitude of the Reynolds stress in the viscous sublayer ($y^* < 4$) is similar for all pressures, but deviates from the case employing the ideal-gas law. This deviation is caused by the presence of significant density fluctuations at these wall-normal locations, which have similar amplitudes regardless of the pressure but are much larger than those computed with the IG law. Subsequently, this later stress is reduced with the pressure at higher y^*. The opposite behaviour occurs regarding viscous stress. The position where both stresses intersect is located at higher y^* for lower pressure, indicating that the viscous stress becomes more important using higher reduced pressure. This shows that the dynamics of the momentum field are primarily governed by the molecular components for $y^* < 6$ and by the

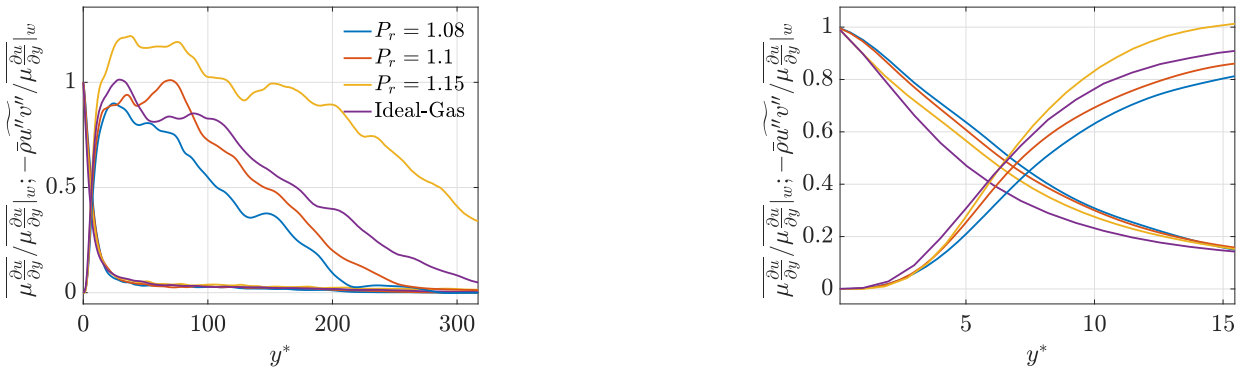

(a) $Re_{\delta;sub} = Re_{\delta;trans} = 440$. (b) $Re_{\delta;sub} = 620; Re_{\delta;trans} = 680$.

Figure 5.14: (a) Decomposition of the total momentum stress into the viscous stress $\overline{\mu\partial u/\partial y}$ and the Reynolds stress $\bar{\rho}\widetilde{u''v''}$. All cases are normalised by the viscous stress at the cold wall. (b) Zoom-in the near-wall region.

turbulent components for $y^* > 20$. These results indicate that the density fluctuations in the heated transcritical turbulent boundary layers do have a significant impact on the Reynolds shear stress and the mean velocity profiles.

5.4 Influence of the Mach number

To assess the influence of the free-stream Mach number and the associated compressibility effects on the transition of a transcritical boundary layer, two different simulations are conducted with the thermodynamic parameters of Tab 5.2, while the numerical parameters are specified in Tab 6.1 for the case labelled as *3D Pr 1.1*.

Simulation	$p_r = \frac{p^*_\infty}{p^*_c}$	$T_r = \frac{T^*_\infty}{T^*_c}$	$T_{w;r} = \frac{T^*_w}{T^*_c}$	M	Ec
1	1.1	0.92	1.08	0.4	0.05
2	1.1	0.92	1.08	0.1	$2.89 \cdot 10^{-3}$

Table 5.2: Thermodynamic parameters used in the different transcritical simulations with different free-stream Mach number.

The linear stability curves corresponding to the thermodynamic parameters presented in Tab 5.2 are shown in Fig 5.15. These figures demonstrate that only Mode II is excited within the computational domain used. The introduction of perturbations occurs within a stable region for both simulations, but the instability develops more rapidly with $M = 0.4$ at $Re_\delta = 470$, compared to $M = 0.1$ at $Re_\delta = 510$. Physically, a lower free-stream Mach number corresponds to lower velocity magnitudes, which result in less energy available to excite the perturbations in the flow. It is important to note that the excitation of second harmonics could potentially activate Mode I with the smaller Mach number.

The modal representation depicted in Fig 5.16(a) confirms that the instability of $(\omega_0, 0)$ is delayed when using a smaller free-stream Mach number. This delayed growth has an impact on the development of the oblique mode. Even though a delayed transition of the fundamental mode occurs with $M = 0.1$, the transition takes place at approximately the same Reynolds number for both $M = 0.4$ and $M = 0.1$,

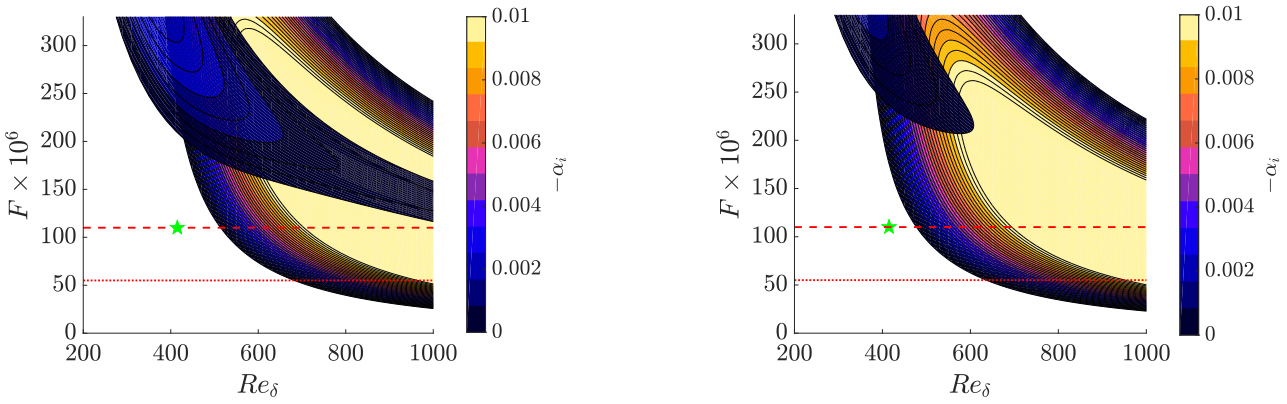

(a) $M = 0.1$. (b) $M = 0.4$.

Figure 5.15: Representation of the stability diagram for various Mach number using a reduced pressure of $P_r = 1.1$ with a wall temperature fixed at $T_w/T_{cr} = 1.08$.

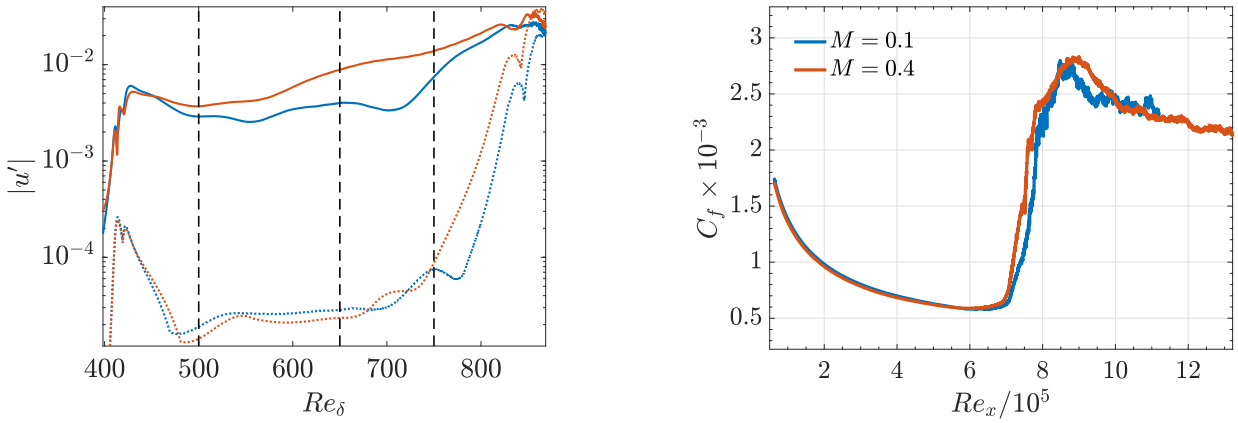

(a) FFT modes. (b) C_f.

Figure 5.16: Representation of different FFT modes obtained with different Mach numbers. (full lines) represents the mode $(\omega_0, 0)$, (:) represents the mode $(\omega_0/2, \beta)$. The black dotted lines represents the position where the profiles will be extracted. (b) Representation of the skin-friction coefficient.

namely at 850 and 865 respectively, as observed in the friction coefficient shown in Fig 5.16(b). This similarity in the transition position can be attributed to the growth rate of the oblique mode, which used $M = 0.4$ is computed to be 65% of the growth rate observed at a smaller Mach number between $Re = 780$ and 830. However, the growth of the skin-friction coefficient in the transition region is very similar, except for the slight delay, as well as the amplitude of the overshoot. This figure highlights the significant changes in the oblique mode for different Mach numbers, suggesting that they are likely influenced by the compressibility effects.

The snapshot of the streamwise velocity in the $(x-z)$ planes at $y^* \approx 10$ in Fig 5.17 reveals a similar pattern in the early Λ-vortices, with a maximum value located at their heads. The vortices start to appear at $x = 575\delta_0$ for both cases, but the main difference lies in the location where the flow becomes turbulent. At the lower Mach number, the growth of the complete triangular vortices is relatively limited compared to $M = 0.4$. As a result, the breakdown, which occurs due to spanwise interactions, progresses more rapidly, and the recognisable Λ pattern disappears after $x = 600\delta_0$, whereas it remains

visible until $x = 650\delta_0$ at lower Mach numbers. The streamwise velocity fields reveal a modification in the length and strength of the Λ-vortices as the Mach number varies. It can be observed that the length of these vortices decreases as the Mach number increases. At the same time, the velocity decreases, indicating a compression and concentration of the Λ-vortices. This behaviour can be attributed to the lower energy levels associated with lower Mach numbers. As the Mach number decreases, the vortical structures weaken, leading to a slower increase in turbulence levels within the flow.
It should be noted that the maximum skin-friction coefficient along the spanwise direction occurs at $z = 5\delta_0$ and $15\delta_0$, the locations where the Ω-vortices lift up and breakdown, as revealed by the Q-criterion in Fig 5.18. These representations use a spanwise direction of length $30\delta_0$ and are very similar for both Mach numbers.

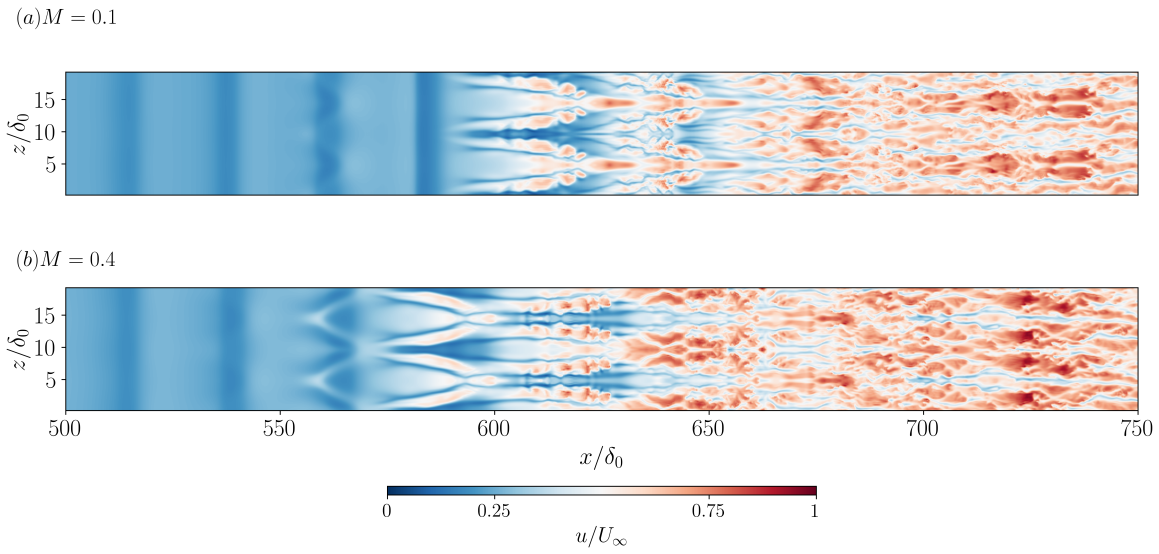

Figure 5.17: Instantaneous snapshot of the streamwise velocity in the $(x - z)$ planes at $y^* \approx 10$ in the transition region.

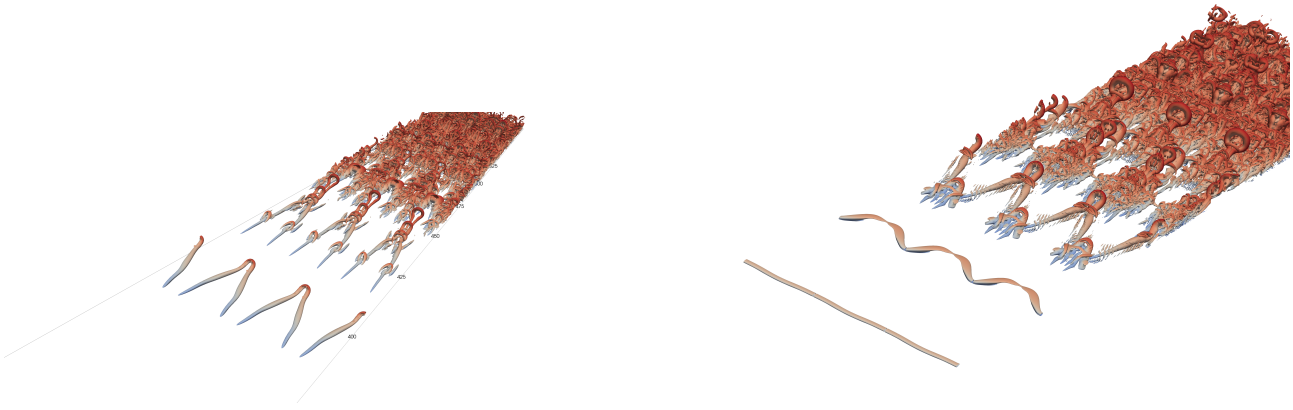

(a) $M = 0.1$.

(b) $M = 0.4$.

Figure 5.18: Instantaneous isosurfaces of the second invariant of the velocity gradient tensor, Q, coloured by streamwise velocity for various Mach numbers. A video of the transcritical breakdown at $M = 0.1$ is provided at `https://youtu.be/ujm5_8kEuEk`.

The streamwise velocity fluctuation profiles extracted at various Reynolds numbers, specifically $Re_\delta = 500$, 650, and 750, indicated by black dotted lines in Fig 5.16(a), are presented in Fig 5.19. These profiles reveal that the Mach number does not significantly affect the overall shape of the fundamental profile, except for the location of its maximum value, which is positioned closer to the wall for lower Mach numbers. Furthermore, an additional observation is the presence of a smoother peak in the oblique profiles when using a lower free-stream Mach number. This suggests that reducing the Mach number of the incoming flow results in a more gradual variation of the oblique profiles, in contrast to the sharper peak observed at higher Mach numbers. The presence of a broader peak in the velocity fluctuation profiles at lower Mach numbers makes it easier to capture and can be a contributing factor to the easier convergence observed in simulations with lower Mach numbers.

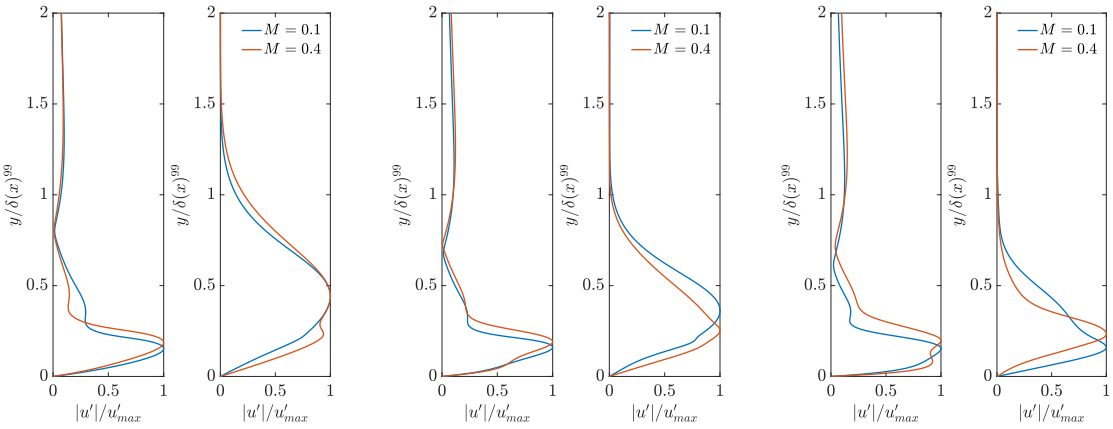

Figure 5.19: Evolution of the streamwise velocity fluctuation profile for the fundamental mode (left) and the subharmonics $(\omega_0/2, \beta)$ (right) for (a)$Re_\delta = 500$, (b)$Re_\delta = 650$ and (c) $Re_\delta = 750$.

The visualisation of the fluctuation density profile, normalised by the maximum amplitude using $M = 0.4$, of the fundamental and oblique mode at a Reynolds number of $Re_\delta = 650$, illustrated in Fig 5.20, demonstrates a reduction in amplitude as the Mach number decreases. A ratio of 55% in terms of amplitude exists in the fundamental profile, this ratio. Analogous to the fluctuation velocity profile, lowering the Mach number brings the peak closer to the wall. This figure provides insight into the underlying cause for the broader peak in the streamwise velocity profiles and the improved convergence of simulations when using a smaller Mach number.

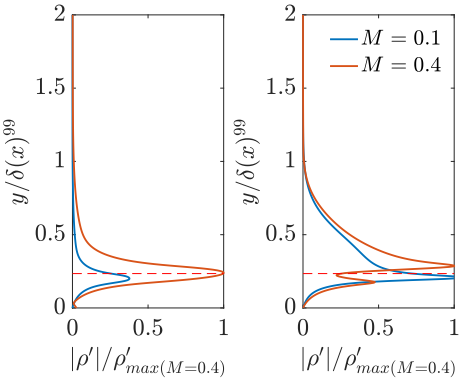

Figure 5.20: Fundamental and subharmonic density fluctuation profiles at $Re_\delta = 650$ for both free-stream Mach numbers. The red dotted line represent the position of the pseudo-critical temperature.

Mean turbulent statistics for different mach number

Interestingly, it is observed that the free-stream Mach number has a minimal impact on the RMS value of the density, dynamic viscosity, and specific heat fluctuations in the turbulent region, as shown in Fig 5.21. Therefore, the Mach number and acoustic effects do not exert a substantial influence on the

mean and fluctuation properties in a transcritical turbulent boundary layer.

The deviation of the mean velocity profiles from the reference profile, as observed in the log-law region ($10 < y^+ < 120$) using Van Driest scaling, remains consistent regardless of the Mach number. This confirms that the deviation is primarily caused by the significant variation in density. The high RMS values of the different thermodynamic quantities, as shown in Fig 5.21, support this attribution, as well as the study of Guo [141]. Although the Mach number is reduced, it does not necessarily lead to a reduction in the RMS value of the density fluctuation. However, it is noteworthy that the maximum fluctuations of density occur at $y^+ \approx 6$, while the mean profiles still closely match the reference profile within this region. This reveals the influence of those fluctuations primarily outside the buffer layer, suggesting a limited impact on the flow dynamics within the viscous sublayer since all the profiles match the relationship $u^+ = y^+$, scaled with δ_0, below $y^+ = 5$.

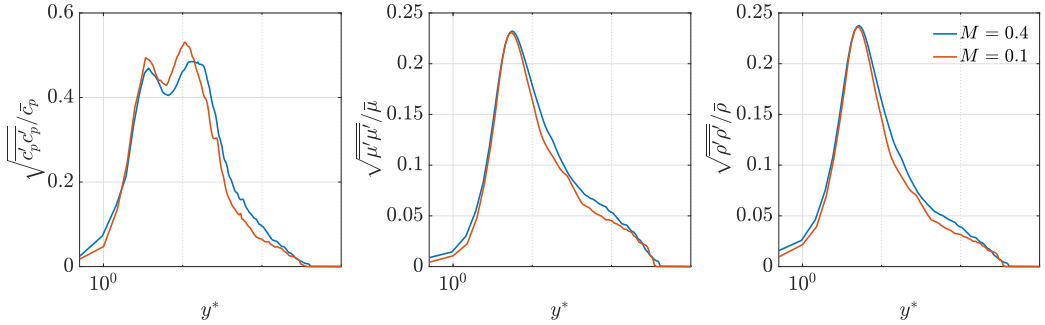

Figure 5.21: Profiles for RMS quantities for (a) dynamic viscosity μ, (b) constant pressure specific heat c_p and (c) density ρ. All profiles are normalised by Reynolds-averaged mean quantities.

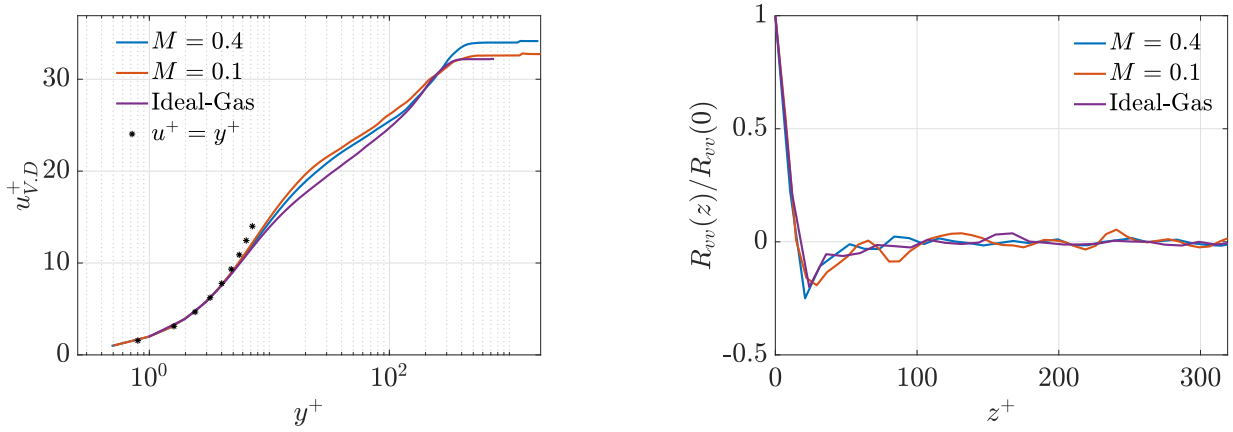

(a) $u^+_{V.D} - y^+$.

(b) $R_{vv}(z)/R_{vv}(0)$.

Figure 5.22: (a) Representation of the mean velocity profile in the turbulent region using the Van Driest scaling for various Mach numbers. (b) Representation of the autocorrelation tensor for the wall-normal velocity along the spanwise dimension measured in wall units.

The characteristic length of the coherent structures, indicated by the sharp minimum in the two-point correlation of the wall normal velocity components, demonstrates an apparent increase for lower Mach numbers. For Mach = 0.4, the length is approximately $\Delta z^+ = 20$, whereas for lower Mach numbers, it measures around $\Delta z^+ = 24$. The latter length is more in line with the characteristic length

computed using the ideal-gas model. Nevertheless, it should be noted that the spanwise discretisation is relatively coarse, and enhancing the results could be achieved by increasing the number of points and averaging over multiple periods. These findings provide valuable insights into the behaviour of vortical structures and turbulence in relation to the Mach number.

5.5 Influence of the wall temperature

The effect of the position of the pseudo-critical temperature on the transition and RMS quantities in a fully turbulent flow will be analysed by modifying the wall temperature. Three simulations will be conducted using the thermodynamic parameters specified in Tab 5.3 and the numerical parameters corresponding to case *3D Pr 1.1* in Tab 6.1. It is important to note that the wall temperatures have been selected in such a way that the dimensionless wall temperature $T_w = T_w^*/T_\infty^*$ exceeds the dimensionless pseudo-critical temperature of $T_{pc}^*/T_\infty^* = 1.102$. This ensures that all boundary layers are in a transcritical condition.

Simulation	$p_r = \frac{p_\infty^*}{p_c^*}$	$T_r = \frac{T_\infty^*}{T_c^*}$	$T_{wall;r} = \frac{T_w^*}{T_c^*}$	$T_{wall} = \frac{T_w^*}{T_\infty^*}$	Ec
1	1.1	0.92	1.04	1.1.3	0.05
2	1.1	0.92	1.08	1.18	0.05
3	1.1	0.92	1.12	1.21	0.05

Table 5.3: Thermodynamic parameters used in the different simulations.

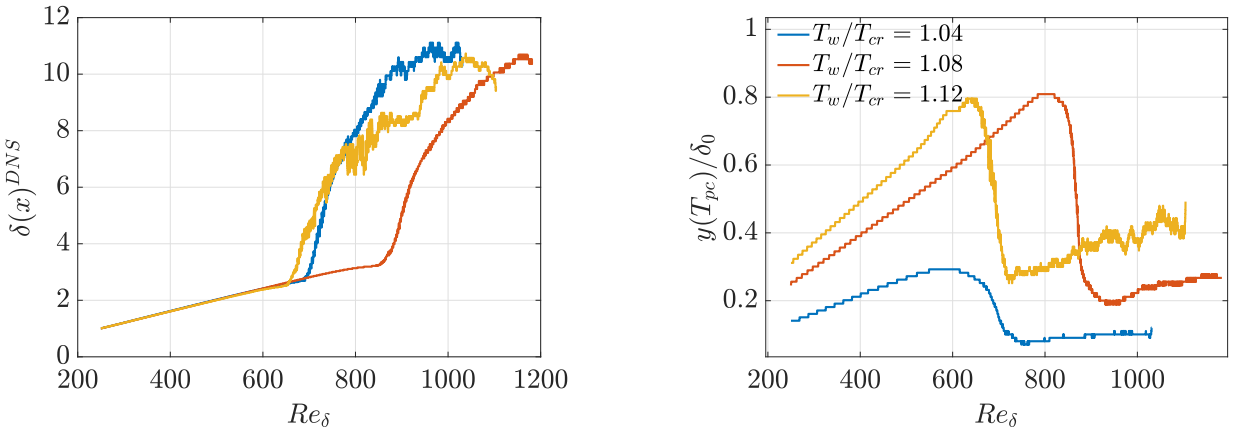

(a) $\delta^{DNS}(x)$.

(b) Pseudo-critical temperature.

Figure 5.23: (a) Evolution of the $\delta^{99}(x)$ boundary layer thickness along the flat-plate for various wall temperatures. (b) Position of the pseudo-critical temperature in the wall-normal direction throughout the domain for various wall temperatures.

The increase in the position of the Widom line, as a function of wall temperature, can be observed in Fig 5.23(b), which shows the location of the pseudo-critical temperature in the wall-normal direction. This indicates that reducing the wall temperature leads to a decrease in the position of the Widom line. However, the growth of the boundary layer thickness, as shown in Fig 5.23(a), suggests that the wall temperature has no influence in the laminar region. Interestingly, the two temperatures that are farthest apart exhibit an earlier transition, indicated by a sudden change, compared to the case

computed with $T_w/T_{cr} = 1.08$. This contrasts with the results obtained in a subcritical boundary layer in Sec 5.1, where an increase in wall temperature resulted in a delayed transition.

Surprisingly, the stability curves obtained with the lower wall temperature, presented in Fig 5.24, only show the presence of Mode I. This mode can be identified by its significantly lower growth rate compared to Mode II. As the wall temperature increases, the presence of Mode I decreases, almost disappearing when using $T_w/T_{cr} = 1.08$, and completely vanishing within the observed frequency range when using $T_w/T_{cr} = 1.12$. However, higher wall temperatures show the appearance of Mode II, which exhibits significant variation with the wall temperature. This causes the initial perturbations (indicated by the green pentagram) to fall outside the unstable range when $T_w/T_{cr} = 1.08$, and inside the unstable range when $T_w/T_{cr} = 1.12$. It is worth noting that the perturbations also fall within the unstable region of Mode I. This difference and its consequences can be observed in the modal representation and the corresponding skin-friction coefficient shown in Fig 5.25.

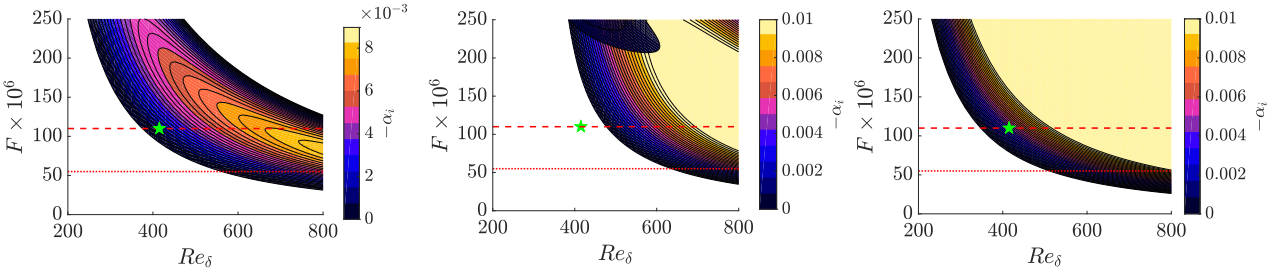

Figure 5.24: Zoom on the stability diagram computed with the properties in Tab 5.3. The left plot is computed with $T_w/T_{cr} = 1.04$, the middle plot is computed with $T_w/T_{cr} = 1.08$ and the right plot computed with $T_w/T_{cr} = 1.12$. The red dotted lines represent the fundamental and subharmonics frequencies. The green pentagram represents the middle of the disturbance strip.

The growth of the fundamental mode, which directly starts after the introduction of the perturbations, is observed for both $T_w/T_{cr} = 1.04$ and $T_w/T_{cr} = 1.12$ cases, with mean growth rates in the primary instability region of approximately $-\alpha_i = 2.5 \cdot 10^{-3}$ and $8 \cdot 10^{-3}$, respectively. This difference results from the presence of either the unstable Mode I or the unstable Mode II, which exhibit different levels of instability. The secondary instabilities for both simulations occur at approximately $Re_x = 3.3 \cdot 10^5$. However, due to the presence of Mode II, the growth rate of the oblique mode is higher for $T_w/T_{cr} = 1.12$, resulting in an earlier interaction at $Re_x = 5 \cdot 10^5$, compared to $Re_x = 5.5 \cdot 10^5$ and thus C_f increases earlier.
In the simulation with a wall temperature of $T_w/T_{cr} = 1.08$, the introduction of perturbations in the stable region leads to a decrease in the amplitude of the fundamental mode until it crosses the stability diagram at $Re_x = 2.4 \cdot 10^5$. Then, the growth rate of this mode resulting from the primary instability is about $-\alpha_i = 3.2 \cdot 10^{-3}$, which falls between the mean growth rates of the previous simulations. This result is consistent with the stability diagram, which predicted a larger growth rate for Mode II that increases with temperature. As a result, the secondary instability and transition occur later for this temperature, as observed from the friction coefficient and the boundary layer thickness. It is observed that when only Mode II is excited, increasing the wall temperature results in a broader and stronger unstable Mode II, leading to an earlier transition. This behaviour is in contrast to what is typically observed in a subcritical boundary layer, as an increase in wall temperature tends to delay the transition.

The absence of a distinct overshoot in the skin-friction coefficient, shown in Fig 5.25, for the two boundary layers transitioning from Mode II was previously observed in Sec 5.1. While the wall temperature has a negligible influence on the maximum value of the overshoot, with a maximum of $2.8 \cdot 10^{-3}$ and $2.7 \cdot 10^{-3}$ for $T_w/T_{cr} = 1.08$ and $T_w/T_{cr} = 1.12$ respectively, this discrepancy may also be attributed to the averaging over a too small number of samples. However, in the case of a transcritical boundary layer transitioning solely due to the unstable Mode I, a distinct overshoot appears with a significantly larger amplitude of 4.1×10^{-3}, which is a 35% increase, compared to the other simulations. Therefore, the previous discussion regarding the friction coefficient can be adjusted, as the lack of overshoot is not due to the thermodynamic properties of the flow but rather to the unstable Mode II.

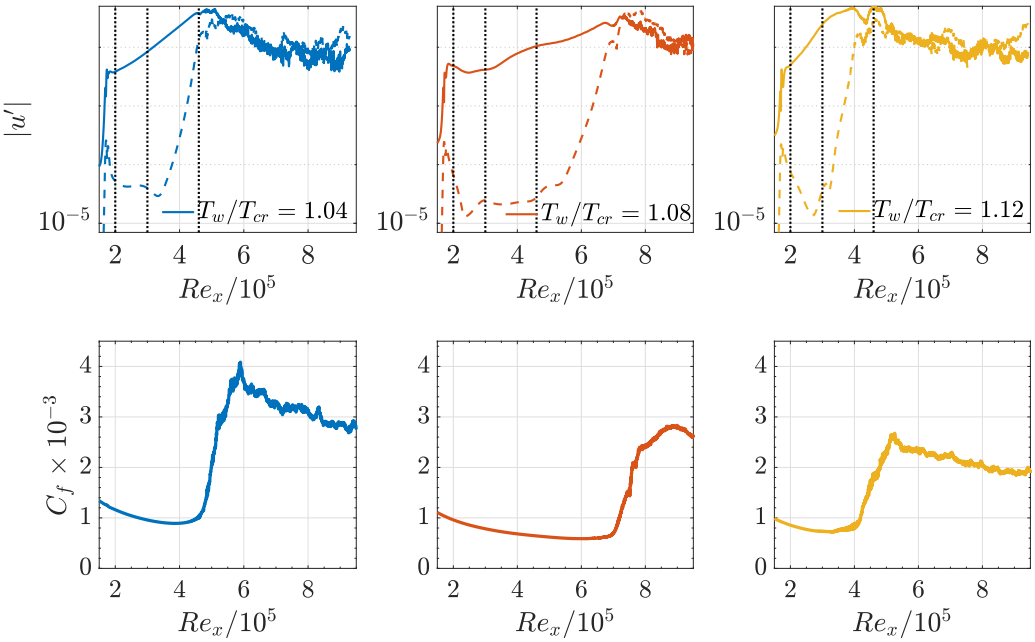

Figure 5.25: Representation of the growth of the two-dimensional mode $(\omega_0, 0)$ and the oblique mode $(\omega_0/2, \beta)$, and the corresponding skin-friction coefficient for various wall temperature. The black dotted line indicates the location from which the fluctuation profiles are extracted.

The influence of the wall temperature on the streamwise velocity and density fluctuation profiles, given in Fig 5.27 and 5.26, is observed at various Reynolds numbers, depicted by black dotted lines on the modal representation in Fig 5.25. These Reynolds are $Re_\delta = 450,\ 550$ and 680. At $T_w/T_{cr} = 1.04$, both the fundamental and subharmonic velocity profiles exhibit the characteristic shape associated with Mode I, which is typically observed in a subcritical boundary layer (as discussed in Sec 5.1). The main difference compared to the subcritical profiles is the presence of a small peak in the fluctuation profiles, which results from the pseudo-critical temperature (indicated by the blue dotted line).

The influence of wall temperature on the density profiles, shown in Fig 5.26, is evident. Each profile has been divided by the maximum amplitude of the profiles computed with the higher wall temperature, which is expected to produce larger peaks. The fundamental and subharmonic profiles extracted at the first two locations reveal the presence of a sharper and higher peak as the wall temperature increases. The higher position of the peak is consistent with the location of the pseudo-critical temperature. However, it should be noted that the peak location does not exactly match with the position of the pseudo-critical temperature, although this difference decreases with increasing wall

temperature. Moreover, the difference in amplitude for the fundamental fluctuation profiles becomes more pronounced as the Reynolds number increases. The last profiles extracted at $Re\delta = 680$ show the earlier transition of the two simulations conducted with $T_w/Tcr = 1.04$ and $T_w/T_{cr} = 1.12$, evidenced from the deviation of the profiles from the reference profile. Increasing the wall temperature leads to larger density fluctuations, which in turn increases the influence of non-ideal gas effects.
The analysis of the effects of those fluctuations on the streamwise velocity profiles resulting from Mode II is given in Fig 5.27. The fundamental profiles during the primary instability show relatively similar characteristics, with discrepancies in the maximum locations attributed to local flow conditions. However, the oblique modes appear to be significantly altered by the wall temperature and the amplitude of the fluctuation, as a broader and higher peak is observed as the temperature decreases. For instance, at Reynolds numbers of 550 and 650, the peak is observed at $y/\delta^{99} = 0.4$ for $T_w/T_{cr} = 1.12$ and at $y/\delta^{99} = 0.2$ for $T_w/T_{cr} = 1.08$. The decreasing slope is more pronounced at the lower temperature, which is probably a result of the lower fluctuation in density. This leads to the appearance of a minimum close to 1 for the latter temperature and close to 1.4 for the higher wall temperature. The profiles taken at higher Reynolds numbers reveal the earlier transition in the simulations conducted with $T_w/T_{cr} = 1.04$ and 1.12, as indicated by the absence of clear patterns and the presence of a wavy shape in the profiles.

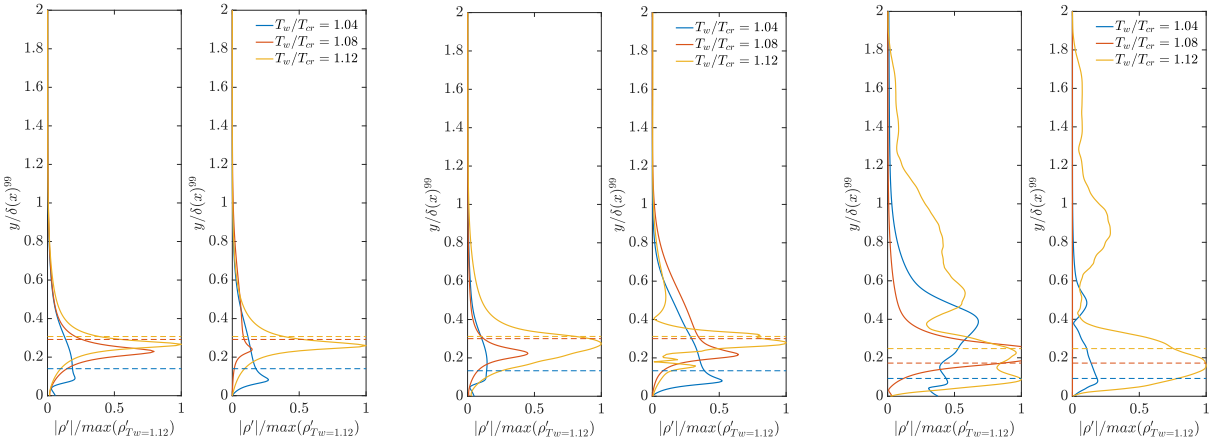

(a) $Re_\delta = 450$ (b) $Re_\delta = 550$ (c) $Re_\delta = 680$

Figure 5.26: Representation of the density fluctuation profiles for the $2D$ fundamental eigenmode $(\omega_0, 0)$ (left) and the oblique mode $(\omega_0/2, \beta)$ (right) at various Reynolds numbers. (a) $Re_\delta = 450$; (b) $Re_\delta = 550$; (c) $Re_\delta = 680$. All these profiles have been normalised by the maximum value of the simulation conducted with $T_w/T_{cr} = 1.12$.

The root mean square amplitudes of the specific heat at constant pressure, dynamic viscosity, and density in a fully turbulent flow, depicted in Fig 5.28, indicate a reduction in the magnitude of these perturbations for lower wall temperatures, with the maximum amplitude becoming closer to the wall. These results are consistent with the fluctuation profiles previously analysed, indicating that the wall temperature has a significant influence not only on the transition region but also on the turbulent statistics. A notable observation is a sudden decrease in amplitude for all quantities when using $T_w/T_{cr} = 1.04$, while the maximum amplitude remains fairly similar, with $\sqrt{\overline{\rho'\rho'}}/\bar{\rho} \approx 0.25$, for the two highest temperatures. These large density fluctuations result in significantly higher non-ideal effects compared to the simulation conducted with $T_w/T_{cr} = 1.04$, as observed. The other mean statistics are not presented here because the same conclusion can be drawn. As the fluctuations increase in amplitude, the different mean statistics deviate from the ideal gas reference.

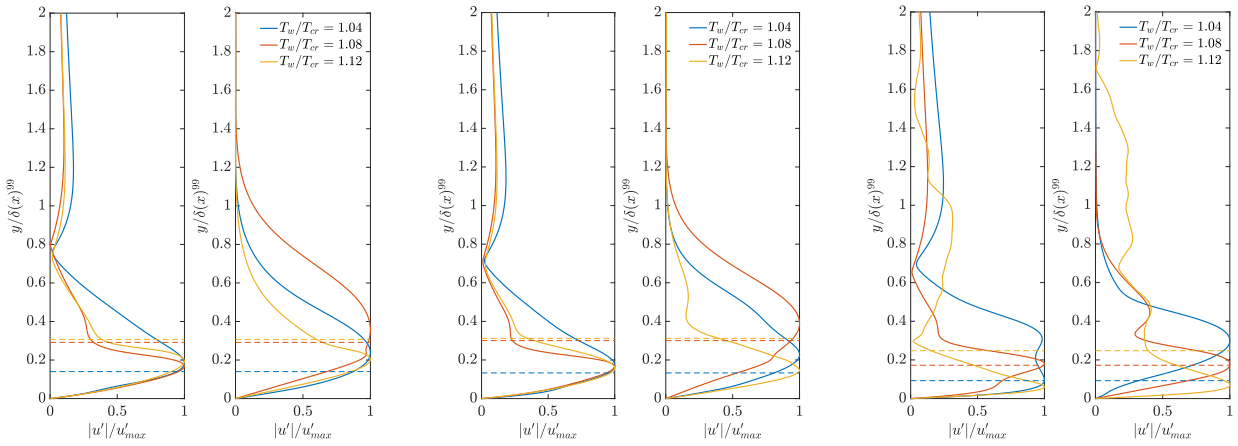

Figure 5.27: Representation of the streamwise velocity fluctuation profiles for the $2D$ fundamental eigenmode $(\omega_0, 0)$ (left) and the oblique mode $(\omega_0/2, \beta)$ (right) at various Reynolds numbers. (a) $Re_\delta = 450$; (b) $Re_\delta = 550$; (c) $Re_\delta = 680$. All these profiles have been normalised by their maximum values.

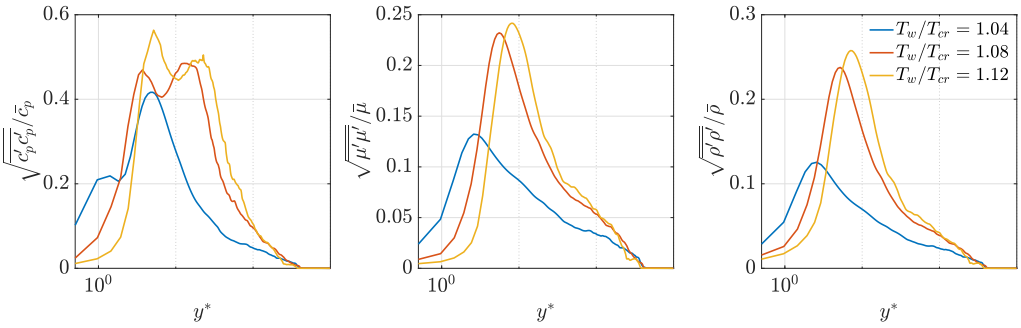

Figure 5.28: Profiles for RMS quantities for (a) dynamic viscosity μ, (b) constant pressure specific heat c_p and (c) density ρ. All profiles are normalised by Reynolds-averaged mean quantities

Chapter 6

Conclusion

6.1 Summary

Zero-pressure gradient flat-plate boundary layers, perturbed in the laminar region, with heated isothermal walls at supercritical pressure, have been studied using direct numerical simulations solving the full compressible Navier-Stokes equations.

The primary objective was to investigate the robustness of the DNS code in analysing the transition of a transcritical boundary layer, which poses challenges due to strong nonlinear non-ideal effects near the pseudo-critical line. To ensure accurate and reliable simulations, a cautious analysis of the domain size and numerical grid was conducted. The grid analysis determined the optimal grid spacing in each direction, considering the need for capturing all flow physics, while maintaining high computational efficiency. This study highlights the importance of accurately discretising the disturbance strip to effectively capture disturbance waves. It was observed that refining the grid in only one direction was insufficient for accurate transition predictions. Furthermore, grid refinement in all directions was necessary to avoid unphysical simulations, and reduce the amplitude of spurious oscillations caused by the combined effect of the Widom line and the transition to a turbulent flow. The analysis revealed a significant challenge in achieving numerical convergence when using a free-stream reduced pressure of $P_r = 1.08$. The large density fluctuations near the pseudo-critical point hindered convergence due to limited computational power, resulting in an abnormal growth of the excited oblique mode $(\omega_0/2, \beta)$ and its interaction with the other excited mode, two-dimensional, at different streamwise locations. In addition, the investigation showed two possible modal behaviours concerning the growth of the oblique mode, raising questions about the sensitivity of those modes. Thus, two solutions have been proposed. Firstly, an increase of free-stream pressure away from the critical point yielded a reduction of the spurious fluctuations, facilitating convergence. Secondly, the free-stream Mach number has been reduced to minimise acoustic effects, which results in broader and lower density fluctuation peaks, leading to faster convergence. More specifically, the analysis revealed abrupt density variations across the Widom line, with $\sqrt{\overline{\rho'\rho'}}/\bar{\rho}$ approximately equal to 0.25 when using $P_r = 1.08$ and decreasing to 0.2 with $P_r = 1.15$.

The second objective of this study was to compare the breakdown mechanisms between of a transcritical boundary layer with a subcritical one. A distinct behaviour of the skin-friction coefficient was observed, showing a significantly lower overshoot-amplitude in thetranscritical case. Moreover, notable differences in the length and strength of the coherent structures were identified, attributed to the substantial density variation caused by the Widom line. It was found that large density fluctuations invalidate Morkovin's hypothesis, and significantly alter the near-wall turbulence and the resulting turbulence statistics.

The final objective of this work was to investigate the influence on the transition at a higher free-stream

reduced pressure and lower Mach number. It was observed that a pressure increase led to a delayed transition, although similar transition patterns were observed. Nevertheless, increasing the pressure did not have any noticeable impact on the C_f-overshoot in the turbulent region. On the other side, a the Mach-number reduction, in order to minimise acoustic effects, resulted in root mean squared values of turbulent thermodynamic quantities with the same amplitude as those computed at higher Mach numbers. This final modification led to more accurate density fluctuation profiles, ensuring faster computational times and improved numerical convergence.

6.2 Future work

Overall, this thesis provides valuable insights into the breakdown mechanisms of transitional boundary layers at supercritical pressure, emphasising the importance of a careful numerical discretisation of the strong nonlinear non-ideal effects. In future works, there are several potential areas of investigation, which are based on the results of this work. Discovering a different perturbation method, or providing a physical explanation for the occurrence of large disturbance harmonics during the laminar flow excitation would be advantageous for a smoother transition, unaffected by high frequency components. Secondly, the investigation of the wall heat transfer between the isothermal flat-plate and the transcritical flow could have significant implications for various industrial applications. Additionally, the analysis of the turbulent kinetic budget equation could also shed light on how the fluid motion are affected by the presence of the Widom line. These potential future research directions would contribute to a deeper understanding of the behaviour of laminar-turbulent transition in supercritical boundary layers.

Case	M	Ec	Pr	S_f	L_y	L_z	Re_{st}	Re_{end}	n_x	n_y
$2D$ Validation	0.4	0.05	1	5.8	40	1	250	900	1500	300
$2D$ Harmonics study	0.4	0.05	1	6	20	1	250	850	200	100
$2D$ Harmonics	0.4	0.05	1	6	40	1	250	850	6000	400
$3D$ IG	0.35	0.05	0.75	5.8	20	10	250	800	3000	220
$3D$ Sayadi	0.35	0.05	0.75	5.8	20	9.63	250	800	3000	200
$2D$ Resolution	0.4	0.05	1	5.8	20	1	250	500	X	250
$3D$ Height Influence	0.4	0.05	1	[5/5.8/6]	[20/40/60]	9.63	250	800	1000	[200/250/280]
$3D$ Sponge Influence	0.4	0.05	1	5	40	9.63	250	800	1000	600
$3D$ Study-Grid-1	0.4	0.05	1	6	40	9.63	250	1100	X	500
$3D$ Study-Grid-2	0.4	0.05	1	5.8	40	9.63	250	800	[1950/2450/3000/4500]	250
$3D$ Study-Grid-3	0.4	0.05	1	5.8	40	9.63	250	800	X	250
$3D$ Study-Grid-Equid	0.4	0.05	1	5.8	40	9.63	250	800	[3426/5140/6850]	250
$3D$ Study-Wall-normal	0.4	0.05	1	10	40	9.63	250	800	[3426/5140/6850]	420
$3D$ Pr = 1.1	0.4	0.05	1	10	40	9.63	250	1050	6000	420
$3D$ $P_r = 1.15$	0.4	0.05	1	10	40	9.63	1200	2000	3146	420

Table 6.1: Values of numerical and physical parameters used in the different simulations. Re_{pt} and l_{pt} stands, respectively, for the Reynolds number defining the center of the disturbance strip and the length of the disturbance strip. All length are non-dimensionalised by the 99^{th} boundary layer thickness at the inlet of the domain, δ_{99}^{th}. X refers to a value modified during the analysis.

Case	n_z	$L_{sp;in}$	$L_{sp;out}$	$L_{sp;top}$	Re_{pt}	l_{pt}	$F_1 \times 10^6$	A_1	$F_2 \times 10^6$	A_2
$2D$ Validation	1	28	150	5	320	10	100	$5 \cdot 10^{-10}$	-	-
$2D$ Harmonics study	1	20	20	5	300	10	110	10^{-3}	-	-
$2D$ Harmonics	1	20	20	5	300	10	110	X	-	-
$3D$ IG	40	20	20	1	415.8	10	100	$2.5 \cdot 10^{-3}$	55	$7.5 \cdot 10^{-5}$
$3D$ Sayadi	40	20	20	1	415.8	10	100	$2.5 \cdot 10^{-3}$	55	$5 \cdot 10^{-5}$
$2D$ Resolution	1	20	20	1	300	10	110	$7.5 \cdot 10^{-3}$	-	-
$3D$ Height Influence	30	20	20	[6.66/13.33/20]	415.8	10	110	$2.5 \cdot 10^{-3}$	55	$7.5 \cdot 10^{-5}$
$3D$ Sponge Influence	30	20	20	X	415.8	10	110	$7.5 \cdot 10^{-3}$	55	$7.5 \cdot 10^{-5}$
$3D$ Study-Grid-1	30	20	20	5	415.8	10	110	$7.5 \cdot 10^{-3}$	55	$7.5 \cdot 10^{-5}$
$3D$ Study-Grid-2	30	20	20	5	415.8	10	110	$7.5 \cdot 10^{-3}$	55	$7.5 \cdot 10^{-5}$
$3D$ Study-Grid-3	X	20	20	5	415.8	10	110	$7.5 \cdot 10^{-3}$	55	$7.5 \cdot 10^{-5}$
$3D$ Study-Grid-Equid	[64/96/128]	20	20	5	415.8	10	110	$2.5 \cdot 10^{-3}$	55	$7.5 \cdot 10^{-5}$
$3D$ Study-Wall-normal	[64/96/128]	20	20	5	415.8	10	110	$2.5 \cdot 10^{-3}$	55	$7.5 \cdot 10^{-5}$
$3D$ Pr = 1.1	64	20	20	5	415.8	10	110	$2.5 \cdot 10^{-3}$	55	$7.5 \cdot 10^{-5}$
$3D$ $P_r = 1.15$	64	20	20	13.33	1300	10	40	$2.5 \cdot 10^{-3}$	20	$7.5 \cdot 10^{-5}$

Table 6.2: Values of numerical and physical parameters used in the different simulations. Re_{pt} and l_{pt} stands, respectively, for the Reynolds number defining the center of the disturbance strip and the length of the disturbance strip. All length are non-dimensionalised by the 99^{th} boundary layer thickness at the inlet of the domain, δ_{99}^{th}. X refers to a value modified during the analysis.

Appendix A

Supercritical fluid

Sutherland's law coefficients for CO_2

	μ_0 [Kg/m.s]	T_0 [K]	S_μ [K]	κ_0 [W/m.K]	S_κ [K]
CO_2	$1.37 \cdot 10^{-5}$	273	222	0.0146	1800

Table A.1: Sutherland's law coefficients for CO_2.

Constant value for the supercritical CO_2

M Kg/mol	R_g J/(Kg.K)	dof -	ω -	T_{crit} K	p_{crit} bar	v_{crit} Kg/m^3
0.0440098	188.9	9	0.224	304.13		0.00208

Table A.2: Constant value for the supercritical CO_2 taken from the Refprop [61].

Derivation of the reduced Van der Waals equation

The dimensional Van der Waals equation of state

$$\left(p + \frac{a}{V^2}\right)(V - b) = RT \tag{A.0.1}$$

can be rewritten in terms of dimensionless variables using the critical parameters T_r, p_r and ν_r. At the critical point one has

$$\frac{\partial p}{\partial \nu}|_{T=T_c} = 0, \quad \text{and} \quad \frac{\partial p^2}{\partial \nu^2}|_{T=T_c} = 0$$

leading to $V_c = 3b$, $p_c = \frac{a}{27b^2}$ and $T_c = \frac{8a}{27bR}$. This lead to

$$a_r = \frac{a^*}{p_c^* \nu_c^{*2} = 3}, \quad b_r = b^*/\nu_c^* = \frac{1}{3}, \quad R_r = \frac{1}{Z_c}. \tag{A.0.2}$$

Introducing those equations in the Van der Waals EoS leads to

$$\left(p_r p_c + \frac{a}{(\nu_r \nu_c)^2}\right)(\nu_r \nu_c - b) = RT_r T_c, \Rightarrow \left(\frac{p_r a}{27b^2} + \frac{a}{(3b)^2 \nu_r^2}\right)(3b\nu_r - b) = RT_r \cdot \frac{8a}{27bR} \tag{A.0.3}$$

$$\left(p_r + \frac{3}{\nu_r^2}\right)(3\nu_r - 1) = 8T_r \tag{A.0.4}$$

Appendix B

Validation 2D simulation

The simulation has been realised with the parameters corresponding to case *2D Validation* in Tab 6.1.

B.1 Comparison criteria

As revealed Sec 2.4, different possible criteria can be used to post-process the results obtained from the direct numerical simulation. Fig B.1 compares the results obtained with the different criterion. It turns out that the criteria based on the kinetic energy give the worst results and the strongest oscillations in the growth rates curve. Nevertheless, these criteria should be more precise as it takes the whole wall-normal direction into account. This could be caused by a too-coarse mesh far away from the wall. The two other criteria based on a single point give results closer to the LST one. To easily compared with experiments, criteria based

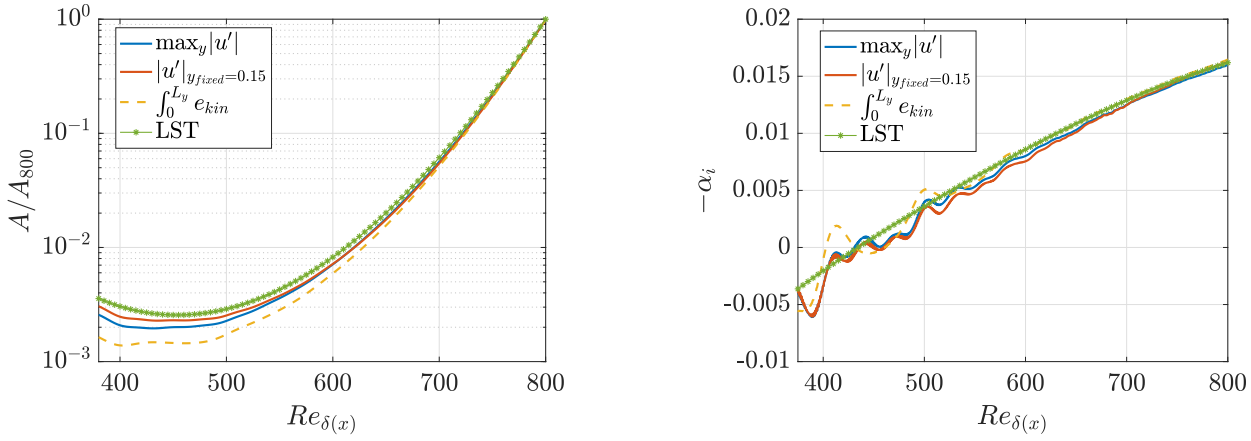

(a) Amplitude .

(b) Growth rate .

Figure B.1: Validation of the results using different criteria with two periods. The amplitude of each result has been normalised by the amplitude at $Re_{delta(x)} = 800$.

B.2 Influence number of periods

Note that all the presented results have been computed by criterion $y_{fixed} = 0.25$. The influence of the number of periods to conduct the Fast Fourier Transform seems negligible when we use more than

2 periods as revealed Fig B.2.

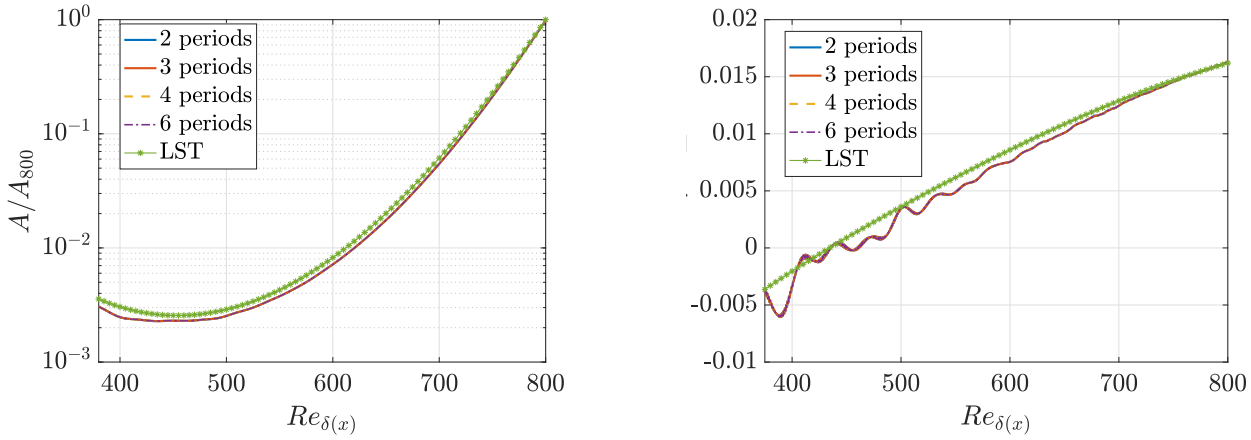

(a) Amplitude.

(b) Growth rate.

Figure B.2: Validation of the results using the y_{fixed} criterion at a value of $y = 0.25$ using different number of periods. The amplitude of each result has been normalised by the amplitude at $Re_{\delta(x)} = 800$.

B.3 Influence wall-normal position

Then, the fixed position using y criterion must also be validated using different values. It turns out that they both give similar results after $Re_\delta = 600$ except for the higher position, $y = 0.5$ which causes more oscillations and underestimates the amplitude of the perturbations at the beginning of the domain.

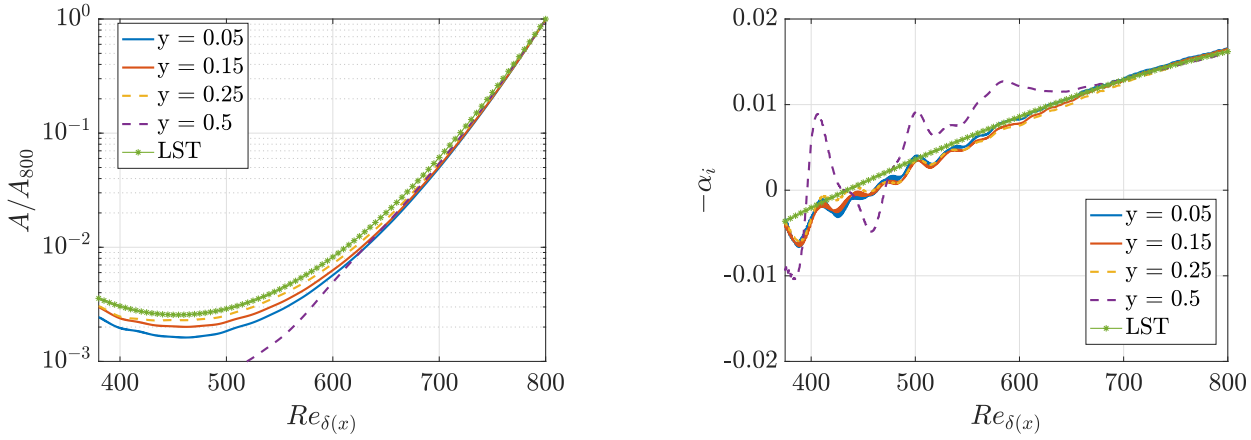

(a) Amplitude .

(b) Growth rate .

Figure B.3: Validation of the results using the y_{fixed} criterion at different value of $y = 0.25$ using two periods. The amplitude of each result has been normalised by the amplitude at $Re_{\delta(x)} = 800$.

Appendix C

Derivation of the skin-friction coefficient

The theoretical formulae for the skin-friction coefficient C_f given as

$$C_f = \frac{\tau_w}{\frac{1}{2}\rho_\infty U_\infty^2}, \quad \text{with} \quad \tau_w = \mu_w \frac{\partial u}{\partial y}, \tag{C.0.1}$$

where τ_w being the wall shear stress. The self-similar variables ψ and f are introduced as

$$\eta = \frac{y}{\delta(x)}, \quad f' = \frac{u}{U_\infty}. \tag{C.0.2}$$

The evaluation of the velocity gradient at the wall become

$$\frac{\partial u}{\partial y}|_w = U_\infty \frac{\partial f'}{\partial y} = U_\infty (\frac{\partial f'}{\partial \eta}|_w \frac{\partial \eta}{\partial y}) = U_\infty f''(0)/\delta(x). \tag{C.0.3}$$

Introducing that $\delta(x) = \sqrt{\frac{2\mu_w x}{U_\infty \rho_w}}$ leads to a wall shear stress of

$$\tau_w = \mu_w U_\infty \sqrt{\frac{U_\infty \rho_w}{2\mu_w x}} f''(0) \tag{C.0.4}$$

The skin-friction coefficient becomes

$$C_f = \frac{\mu_w U_\infty \sqrt{\frac{U_\infty \rho_w}{2\mu_w x}} f''(0)}{\frac{1}{2}\rho_\infty U_\infty^2} \tag{C.0.5}$$

$$C_f = \frac{U_\infty^2 f''(0) \sqrt{\mu_w}\sqrt{\rho_w}}{\frac{\sqrt{2}}{2}\rho_\infty U_\infty^2 \cdot \sqrt{U_\infty x}}. \tag{C.0.6}$$

The Reynolds number $Re_x = \frac{U_\infty x \rho}{\mu}$ can be introduced such that

$$C_f = \sqrt{\frac{\mu_w \rho_w}{\mu \rho}} \frac{2f''(0)}{\sqrt{2} \cdot \sqrt{Re_x}} = \sqrt{2} f''(0) \cdot C_w^{1/2} Re_x^{-1/2} \tag{C.0.7}$$

Blasius solution for an incompressible laminar fluid recovers that $f''(0) = 0.4695$.

Appendix D

Non-ideal gas simulations

D.1 Effect of the grid ratio

The influence of the spanwise grid spacing is conducted using $\Delta x_{\text{turb}} = 0.25$. The growth of the modes, in Fig D.1 and the relative errors in Tab D.1, reveals the minimal influence of this ratio.

$\Delta x_{\text{turb}}/\Delta z$	ε [%] $(\omega_0, 0)$	ε [%] $(\omega_0/2, \beta)$
078	2	1.8
1	1.29	0.98
1.5	0.44	0.4

Table D.1: The relative errors of the different FFT modes computed on a mesh refined in the streamwise direction with a grid spacing of $\Delta x_{\text{turb}} = 0.25$. The errors are computed with respect to the finest grid for Re_δ ranging from 400 to 700.

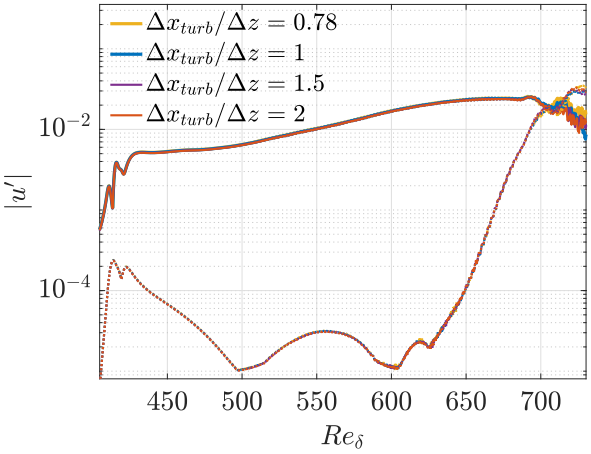

Figure D.1: Representation of the different FFT modes obtained with $\Delta x_{\text{turb}} = 0.25$ and various refinements in the spanwise direction. $(-)$ represents the mode $(\omega_0, 0)$, $(..)$ represents the mode $(\omega_0/2, \beta)$.

D.2 Amplitude of FFT modes in a matrix form

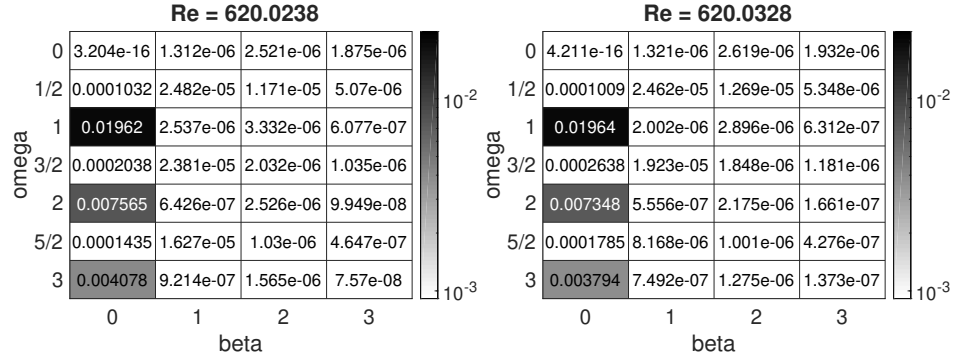

(a) $\Delta x = 0.075$.

(b) $\Delta x = 0.15$.

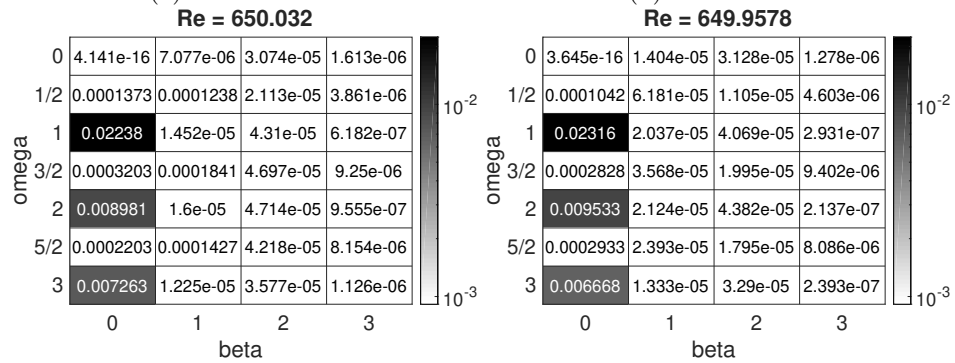

(c) $\Delta x = 0.075$.

(d) $\Delta x = 0.15$.

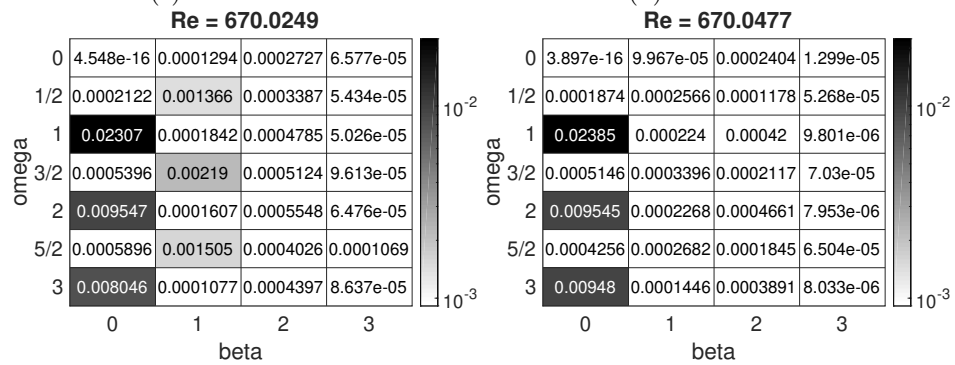

(e) $\Delta x = 0.075$.

(f) $\Delta x = 0.15$.

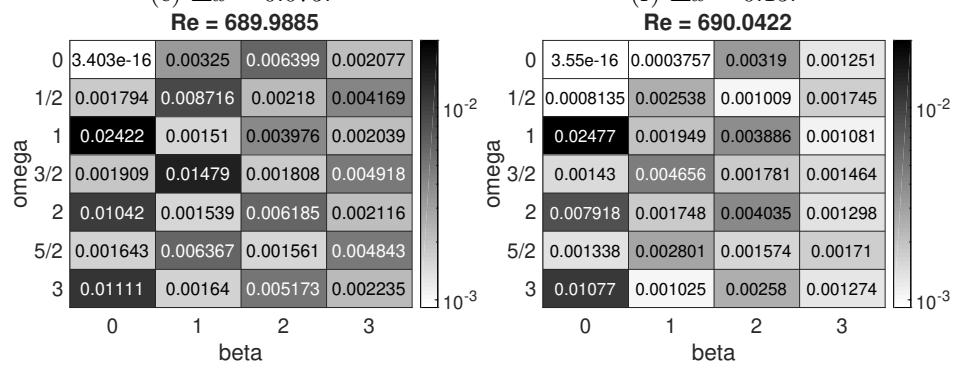

(g) $\Delta x = 0.075$.

(h) $\Delta x = 0.15$.

Figure D.2: Representation of the amplitude of different modes at $Re_\delta = 620$, 650, 670 and 690.

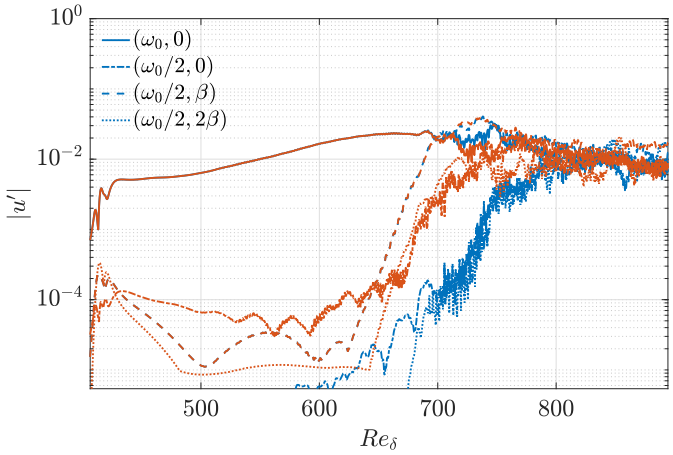

Figure D.3: Representation of FFT modes obtained exciting 7 (red) and 2 (blue) oblique modes.$(-)$ represents the mode $(\omega_0, 0)$, $(-.-)$ represents $(\omega_0/2, 0)$, $(--)$ represents $(\omega_0/2, \beta)$, $(..)$ represents $(\omega_0/2, 2\beta)$.

D.3 Influence different oblique modes

Two different simulations were conducted using the physical and numerical parameters corresponding to case *3D Study-Grid 3*. In the first simulation, seven different oblique modes ranging from -3β to 3β were excited, while in the second simulation, only two modes, $-\beta$ and β, were excited. The growth of all oblique modes is shown in Fig D.3. Remarkably, it is observed that the path followed by the first oblique mode $(\omega_0/2, \beta)$, which is responsible for the transition, remains unchanged regardless of the number of excited oblique modes. Consequently, based on this figure, it can be concluded that exciting the remaining modes are useless as they do not alter the turbulence development process. The same conclusion can be drawn from the C_f.

D.4 Fluctuation profiles on two equidistant meshes

The streamwise velocity and fluctuations profiles conducting with the same physical parameters on two meshes refined differently in the streamwise direction are presented in Fig D.5.

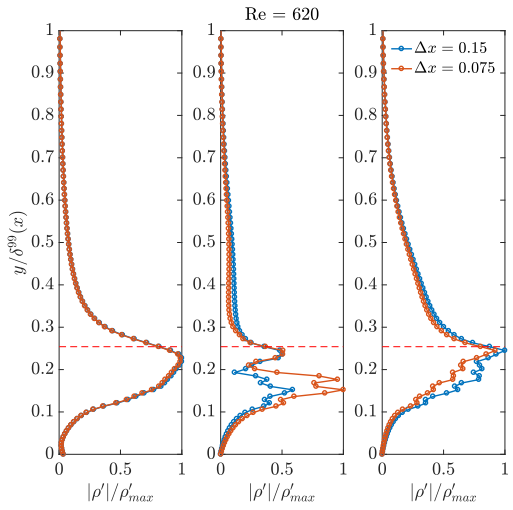

(a) $Re_\delta = 620$.

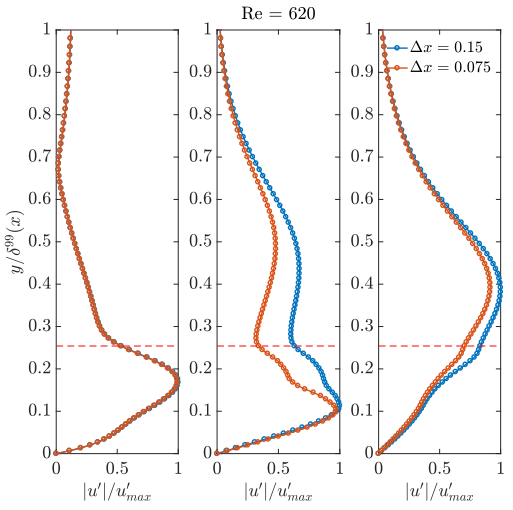

(b) $Re_\delta = 620$

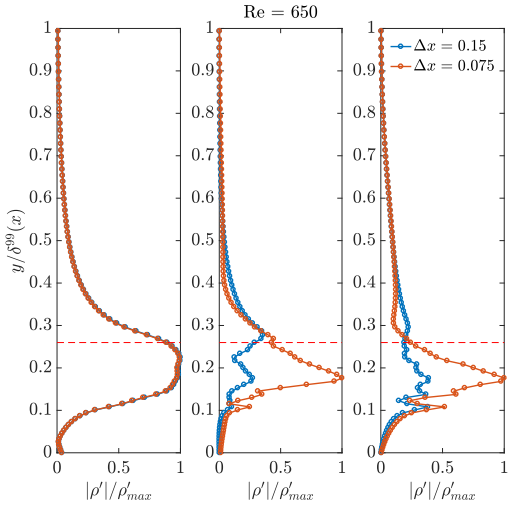

(c) $Re_\delta = 650$.

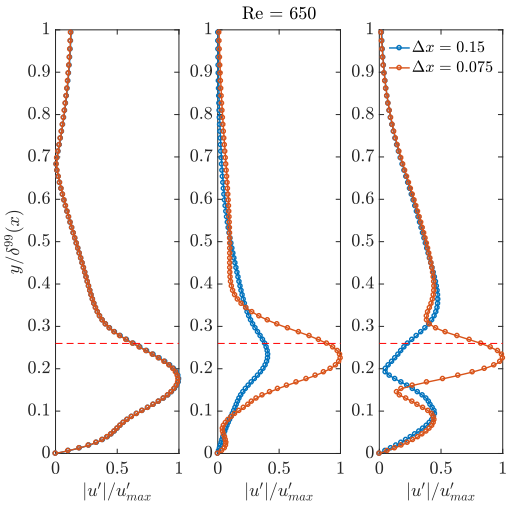

(d) $Re_\delta = 650$.

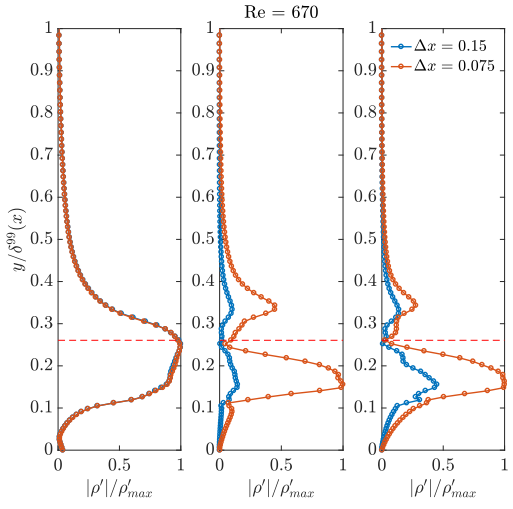

(e) $Re_\delta = 670$.

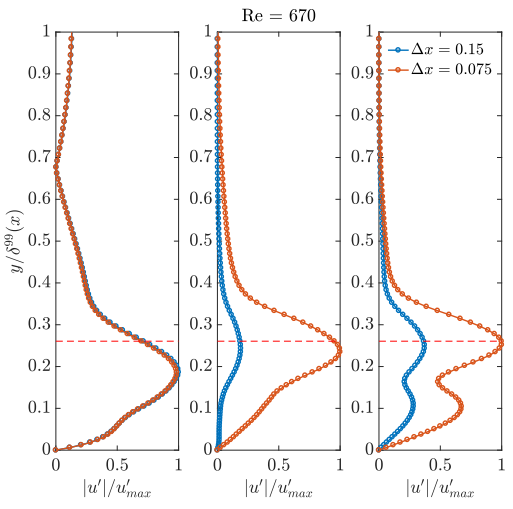

(f) $Re_\delta = 670$.

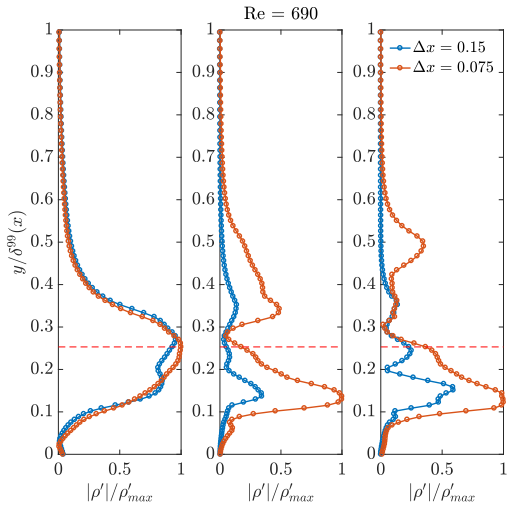

(a) $Re_\delta = 690$.

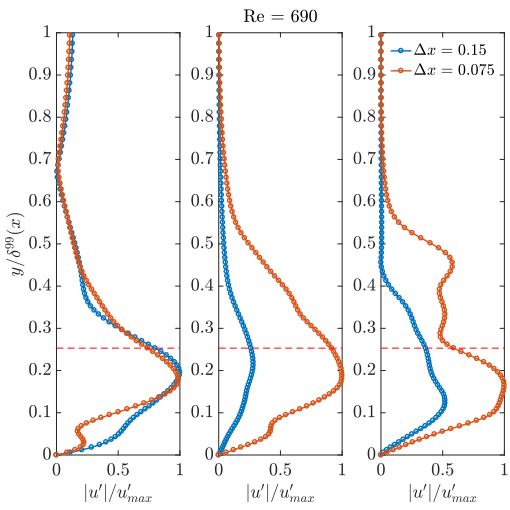

(b) $Re_\delta = 690$.

Figure D.5: Representation of both the density fluctuation profile and the streamwise velocity fluctuation profile for the fundamental mode (left) $(\omega_0, 0)$ and the oblique modes (middle) $(\omega_0/2, \beta)$ and (right) $(\omega_0/2, 2\beta)$ at different Reynolds. The red lines indicate the location of the pseudo-critical temperature.

D.5 Influence top boundary

The evolution of different modes as a function of the top sponge configurations.

Fig D.6 reveals that the subharmonic mode $(\omega_0/2, 0)$ is highly affected by the modification of the sponge but the present oscillations are inside the laminar region. Both figures reveal the necessity to use a sponge length larger than 5. Fig **??** shows that the sponge strength must be larger than 0.5 but not larger than 5.

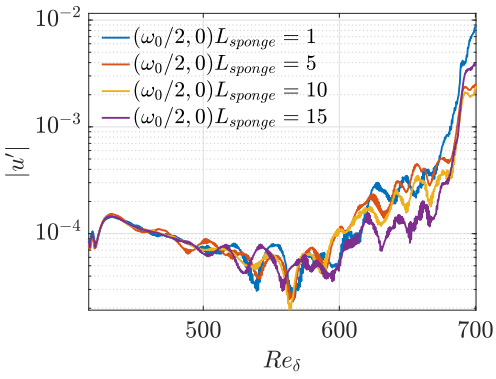

(a) $(\omega_0/2, 0)$.

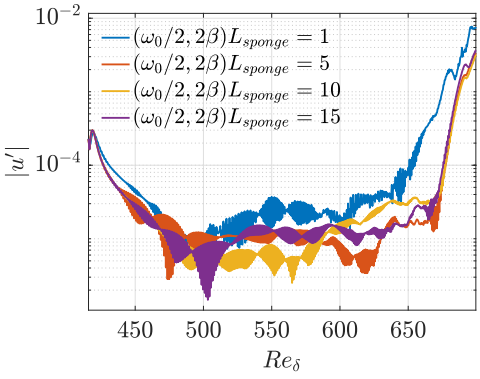

(b) $(\omega_0/2, 2\beta)$.

Figure D.6: Evolution of (a) the two-dimensional subharmonics mode $(\omega_0/2, 0)$ and (b) the oblique mode $(\omega_0/2, 2\beta)$ for different sponge length at the top of the domain.

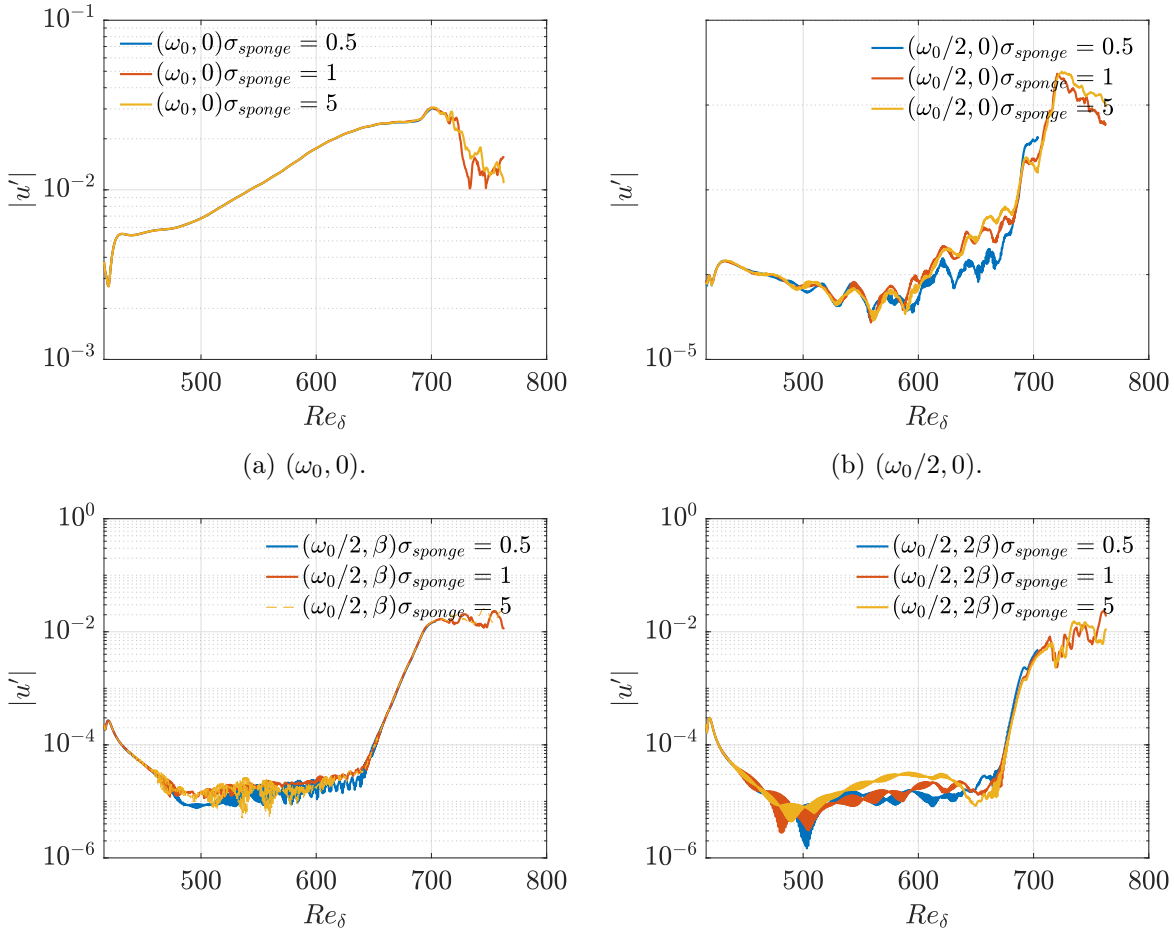

(a) $(\omega_0, 0)$.

(b) $(\omega_0/2, 0)$.

(c) $(\omega_0/2, \beta)$.

(d) $(\omega_0/2, 2\beta)$.

Figure D.7: Evolution of FFT modes for different sponge strength at the top of the domain.

Discretisations of the forcing wave

The influence of the number of points used in the disturbance strip on the different eigenmodes is given in Fig D.8. The same conclusion made on the $2D$ modes can be drawn namely that using more than 120 points on the disturbance strip with a length of 10 seems to be enough to converge.

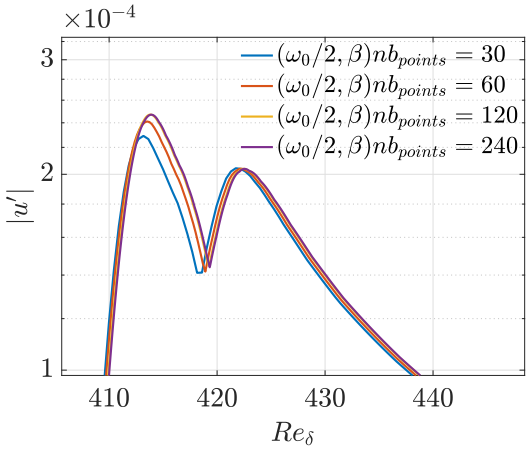

(a) $(\omega_0/2, \beta)$.

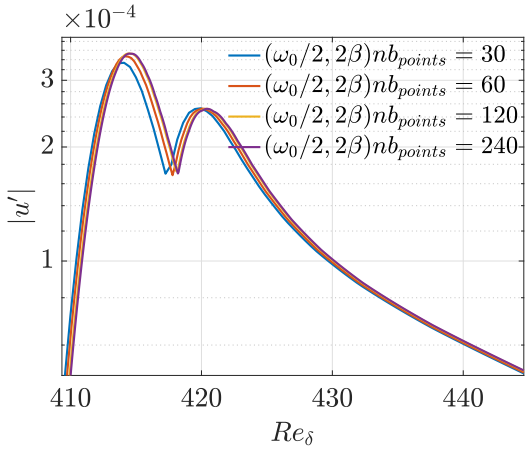

(b) $(\omega_0/2, 2\beta)$.

Figure D.8: Representation of the oblique modes $(\omega_0/2, \beta)$ and $(\omega_0/2, 2\beta)$ inside the disturbance strip for various number of points used to discretize the forcing area.

The influence of the number of samples per period in Fig D.9 shows that a larger number of samples increase the accuracy of the results. The amplitude of the different modes almost collapse using more than 20 samples bu doubling the number of samples requires to double the number of files, such that 10 samples will be kept.

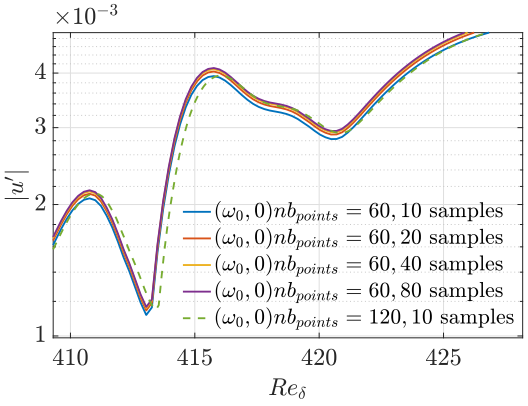

(a) $(\omega_0, 0)$.

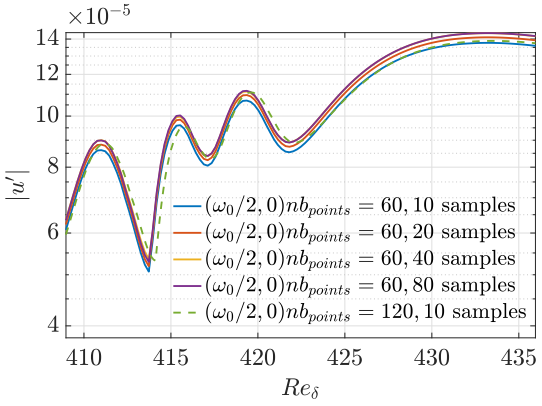

(b) $(\omega_0/2, 0)$.

Figure D.9: Representation of the FFT modes $(\omega_0, 0)$ and the subharmonic $(\omega_0/2, 0)$ for using 60 points on the disturbance strip with different numbers of samples per period. The mode computed with 120 points in the disturbance strip is used as reference.

D.6 Streamwise velocity fields in a subcritical and transcritical boundary layer

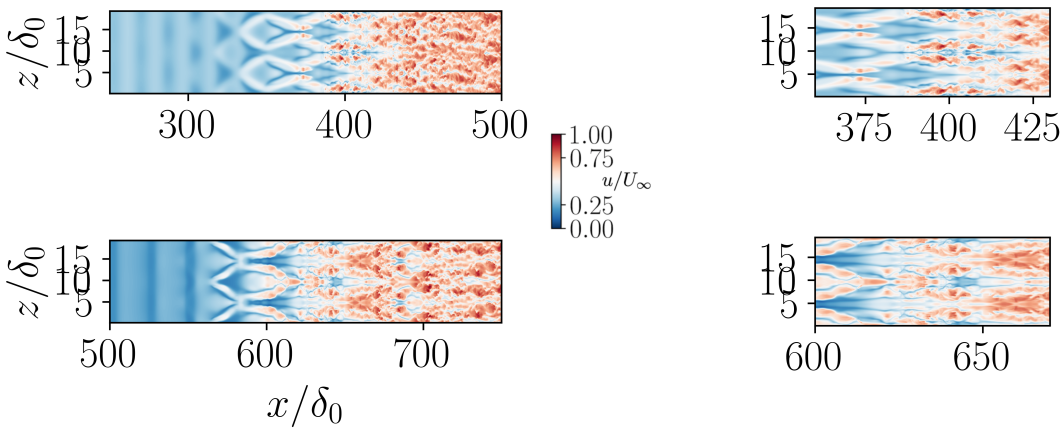

Figure D.10: Representation of the streamwise velocity fields in the subcritical boundary layer with $T_w/T_{cr} = 1$ (top) and the transcritical boundary layer (bottom)

Appendix E

Higher frequency components

The amplitude of the different harmonics will be analysed as a function of various numerical parameters on a $2D$ case.

E.1 Influence of the grid

Fig E.1 reveals that using $n_x = 1000$ enables to capture correctly the fundamental harmonics but is clearly not sufficient to capture the second harmonics. From those figures, it turns out that using $2n_x$ which is 2000 points in the streamwise direction is necessary to capture the second harmonics. Note also that the same mesh enables to accurate capture the third harmonics.

E.2 Influence of number of samples

Fig E.2 represents the amplitude of the first two harmonics computed with different numbers of samples per period. Using 5 and 10 samples per period doesn't allow to capture the second harmonics properly, while 15 does. In the same way, 15 samples don't capture the third harmonics. In this study, the focus is put on the first 3 harmonics and therefore, 20 samples will be chosen.

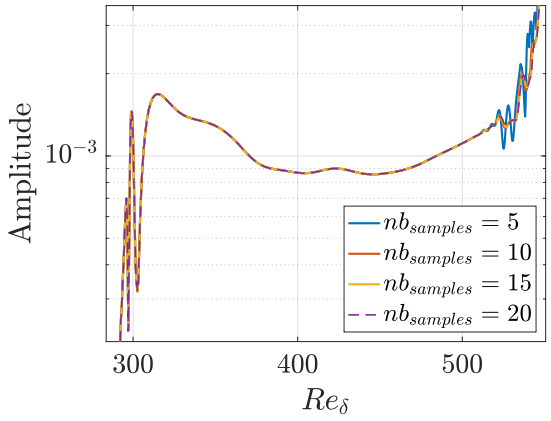

(a) $1st$ harmonic .

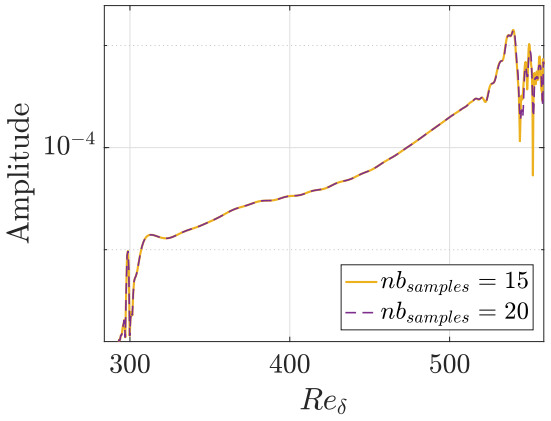

(b) $2nd$ harmonic.

Figure E.2: Representation of the first two harmonic for different numbers of samples per period.

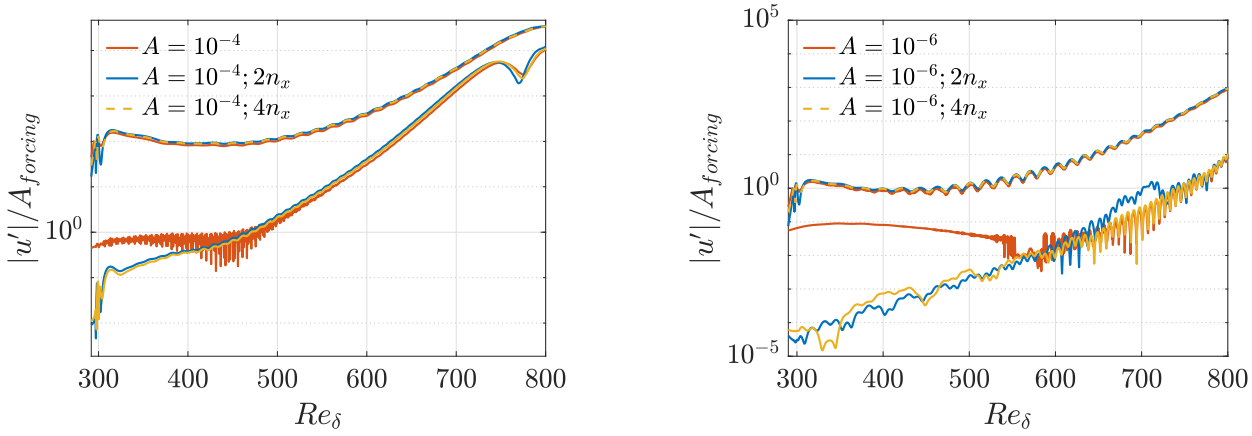

(a) $A = 10^{-4}$. (b) $A = 10^{-6}$.

Figure E.1: Representation of the first two harmonic, normalised by the forcing amplitude, with $A = 10^{-6}$ and 10^{-4} in $2D$ simulations.

E.3 Influence sponge

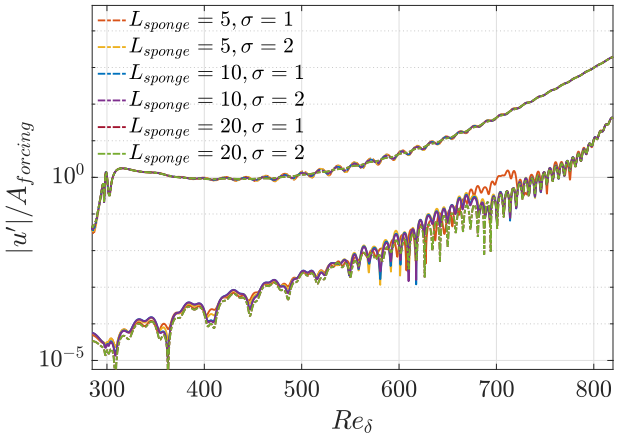

Figure E.3: Representation of the first two harmonics, non-dimensionalised by the forcing amplitude of 10^{-6}, present in the response of a $2D$ transcritical simulation for various top-sponge configuration.

Fig E.3 shows the small impact on the top sponge length and strength on the first two harmonics using a forcing amplitude of 10^{-6}.

E.4 Influence top height

Fig E.4 reveals the very low impact of the domain height on the amplitude of the different harmonic.

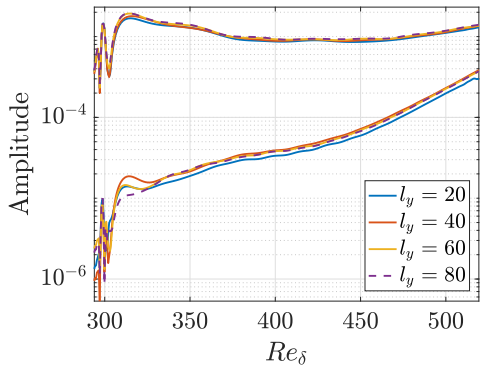

Figure E.4: Representation of the first two harmonic for different wall normal dimension.

Appendix F

Transcritical simulation with higher pressure

The simulations conducted with $P_r = 1.15$ is conducted with the thermodynamic quantities corresponding to *Transcritical 2* in Tab 4.4. It is worth noting that increasing the pressure once again results in the smoothing of sharp property gradients, rendering further grid analysis unnecessary. The linear stability curve shown in Fig F.1(a) demonstrates that increasing the pressure delays the transition, consistent with the observations made with $P_r = 1.1$. Using these parameters, the two unstable modes become distinctly separated. Mode I is located at a higher frequency and lower Reynolds number, while Mode II is positioned at high Reynolds numbers and low frequencies. However, the same physical parameters as before would become inadequate as a frequency of 110×10^{-6} would not excite Mode II. The location of the disturbance strip, as well as the fundamental and subharmonic frequencies, has been modified to achieve the desired H-type transition as

$$Re_{pt} = 1300, \quad F_1 = 40 \cdot 10^{-6} \quad \text{and} \quad F_2 = 20 \cdot 10^{-6}. \tag{F.0.1}$$

Significant modifications have been made to the physical and numerical parameters of the simulation, in case *3D* $P_r = 1.16$ in Tab 6.1. These modifications were implemented while keeping the grid spacing unchanged in each direction. The modal representation, given in Fig F.1(b), reveals the importance of both oblique modes $(\omega_0/2, \beta)$ and $(\omega/2, 2\beta)$ in the transition process as they intersect the fundamental mode at approximately the same Reynolds number. Consistent with the use of $P_r = 1.08$ and 1.1, as well as the LST diagram, the growth of the fundamental mode $(\omega_0, 0)$ decreases with increasing pressure. For example, it demonstrates a growth rate of $-\alpha_i = 0.0038$ when $P_r = 1.1$ after $Re_\delta = 720$, whereas this growth rate is $-\alpha_i = 0.0029$ when $P_r = 1.15$ for Reynolds above 1350.

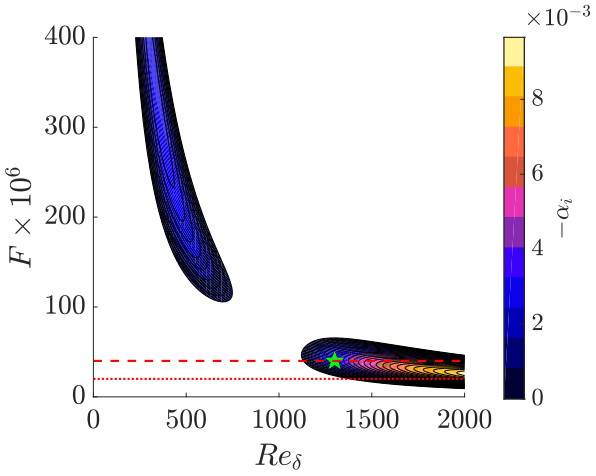

(a) Linear stability diagram.

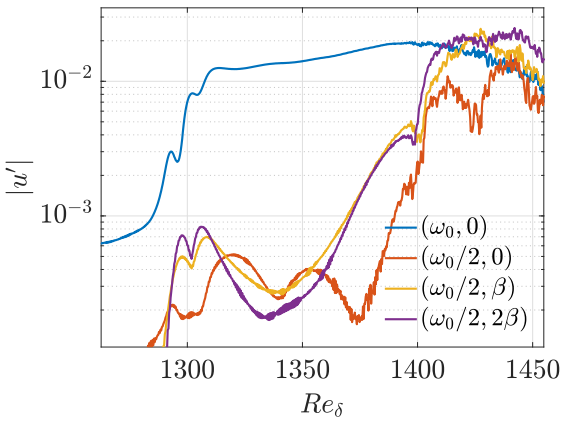

(b) FFT modes.

Figure F.1: (a) Representation of the linear stability diagram with the corresponding thermodynamic properties for *Transcritical 2*. The red dotted line represents the fundamental and subharmonic frequencies and the green pentagram the middle of the disturbance strip. (b) Representation of the fundamental mode and three different excited oblique modes.

Bibliography

1. Sfen. *Le prix de l'électricité augmente... et ça ne devrait pas s'arrêter !* `https://www.sfen.org/rgn/prix-electricite-augmente-ca-arreter/`. 2021.
2. Pope & B, S. *Turbulent Flows* (Cambridge University Press, 2000).
3. G., D. P. & H., R. W. Hydrodynamic Stability. *Cambridge University Press* (2004).
4. Kachanov, Y. S. Physical mechanisms of laminar boundary-layer transition. *Annual Review of Fluid Mechanics* **26,** 411–482 (1994).
5. Klebanoff, P., Tidstrom, K. D. & Sargent, L. M. The three-dimensional nature of boundary-layer instability (1957).
6. G., K. L. S., Komoda, H. & Vasudeva, B. . R. Detailed flow field in transition. *Proc. 1962 Heat Transf and Fluid Mech , pp. 1-26.* (1962).
7. Jaluria, Y. & Gebhart, B. On transition mechanisms in vertical natural convection flow. *Journal of Fluid Mechanics* **66,** 309 (1974).
8. Lock, G. S. H. & Trotter, F. J. D. Observations on the structure of a turbulent free convection boundary layer. *International Journal of Heat and Mass Transfer* **11,** 1225 (1968).
9. Bertrand, B., Malte, H. & Ralph, K. Critical phenomena: 150 years since Cagniard de la Tour. *Journal of Physical Studies. 13* (2009).
10. Brunner, G. Applications of Supercritical Fluids. *Annual Review of Chemical and Biomolecular Engineering* **1.** PMID: 22432584, 321–342. `https://doi.org/10.1146/annurev-chembioeng-073009-101311` (2010).
11. Haas, T. J., Foglia, T. A. & Marmer, W. N. in *Supercritical Fluid Technology in Oil and Lipid Chemistry* 2nd, 269–287 (AOCS Press, 2002). ISBN: 978-1893997627.
12. Poling, B. E., Prausnitz, J. M. & O'Connell, J. P. *The Properties of Gases and Liquids* 5th. ISBN: 978-0070116825 (McGraw-Hill, 2000).
13. Sengupta, U., Nemati, H., Boersma, B. J. & Pecnik, R. Fully Compressible Low-Mach Number Simulations of Carbon-dioxide at Supercritical Pressures and Trans-critical Temperatures. Flow Turbulence Combust 99, 909–931 (2017). 122301. `https://doi.org/10.1007/s10494-017-9872-4`.
14. Kawai., S. Heated transcritical and unheated non-transcritical turbulent boundary layers at supercritical pressures (2019).
15. MORKOVIN, M. V. Critical evaluation of transition from laminar to turbulent shear layers with emphasis of hypersonically traveling bodies, (1969).
16. G. Cooppola, F. C. & de Luca, L. Discrete energy-conservation properties in the numerical simulation of the navier stokes equations. *Appl, Mech. Rev. 71* (2019).
17. Abgrall., R. How to prevent pressure oscillations in multicomponent flow calculations: A quasi conservative approach. *J.Comput. Phys. 125* (1996).

18. Shima, N., Kuya, Y., Y.Tamaki & S.Kawai. Preventing spurious pressure oscillations in split convective form discretization for compressible flows. *J.Comput. Phys. 427* (2021).
19. Schmitt, T., Selle, L., Ruiz, A. & Cuenot., B. Large-eddy simulation of supercritical-pressure round jets. *AIAA Journal* (2010).
20. Jiménez, J. Coherent structures in wall-bounded turbulence. *Journal of Fluid Mechanics* **842,** P1 (2018).
21. Ergin, F. G. o., Choudhari, M., Fischer, P. & Tumin., A. TRANSIENT GROWTH: EXPERIMENTS, DNS AND THEORY (2019).
22. Lord, R. Investigation of the character of the equilibrium of an incompressible heavy fluid of variable density. Proceedings of the London Mathematical Society. 14: 170–177. (1882).
23. Serkan Ozgen, S. A. K. Linear stability analysis in compressible, flat-plate boundary-layers. (2007).
24. L., L. & C.C., L. Investigations of the stability of the laminar boundary layer in a compressible fluid. *NASA* (1946).
25. Malik, M. Prediction and control of transition in supersonic and hypersonic boundary layers. *AIAA J. 27(11), 1487– 1493* (1989).
26. Gaster, M. On the effects of boundary-layer growth on flow stability. *J. Fluid Mech. vol. 66, no. 3, pp. 465–480.* (1974).
27. Smith, F. On the non-parallel flow stability of the Blasius boundary layer. *Proc. R. Soc. London, Ser. A, vol. 366, pp. 91–109.* (1979).
28. Fani, A. & Luchini, P. The importance of nonlinearities and higher harmonics in the linear instability of boundary-layer flows. *Journal of Fluid Mechanics* **875,** 1217–1242 (2019).
29. Ren, J., Fu, S. & Pecnik, R. Linear instability of Poiseuille flows with highly non-ideal fluids. *Journal of Fluid Mechanics* **859,** 89–125 (2019).
30. Tollmien, W. General Instability Criterion of Lam- inar Velocity Distributions. T 1 M. No. 792, (1936).
31. Tollmien, W. The Production of Turbulence. T.M., (1931).
32. Rempfer, D. & Fasel, H. F. Evolution of three-dimensional coherent structures in a flat-plate boundary layer (2006).
33. H., F. & U., F. R. Numerical investigation of the three-dimensional development in turbulent boundary layers (1990).
34. Monkewitz, P. A. & Chomaz, J.-M. Absolute and convective instabilities of the Batchelor vortex. *Journal of Fluid Mechanics* **219,** 195–214 (1990).
35. Christensen, K. T. & Adrian, R. J. Statistical evidence of hairpin vortex packets in wall turbulence. *Journal of Fluid Mechanics* **431,** 433–443 (2001).
36. W., S. & A., T. Experiments on the subharmonic route to turbulence in boundary layers (1984).
37. Sayadi, T., Hamman, C. W. & Moin, P. Direct numerical simulation of complete H-type and K-type transitions with implications for the dynamics of turbulent boundary layers. *Journal of Fluid Mechanics* **724,** 480–509 (2013).
38. S., B., W., M. D. G. & U., R. Turbulence mechanism in Klebanoff transition: a quantitative comparison of experiment and direct numerical simulation. *J. Fluid Mech. 459, 217–243.* (2002).
39. Ya., K. Y. L. V. & V., K. V. Nonlinear development of a wave in a boundary layer. (1977).

40. F., F. H. & U., R. U. K. Non-parallel stability of a flat plate boundary layer using the complete Navier-Stokes equations. (1990).
41. J., S. P. & S., H. D. A new mechanism for rapid transition involving a pair of oblique waves. *Phys. Fluids A 4, 1986–1989.* (1992).
42. Elofsson, A. & Henrikalfredsson, P. An experimental study of oblique transition inplane Poiseuille flow. *Fluid Mech. vol. 358, pp. 177–202* (1998).
43. Saric, W. S. & Thomas, A. S. W. *Experiments on the subharmonic route to turbulence in boundary layers* in (1984).
44. Vinuesa, R., Örlü, R., Schlatter, P. & Hanifi, A. Turbulent boundary layer transition over a flat plate: an assessment of the current state-of-the-art. *Journal of Fluid Mechanics* **802,** 654–687 (2016).
45. Fürst, J. Numerical Simulation of Transitional Flows with Laminar Kinetic Energy. (2013).
46. Langel, C. M. & Chow, R. A Computational Approach to Simulating the Effects of Realistic Surface Roughness on Boundary Layer Transition. (2014).
47. Mori, K. *et al.* Direct total skin-friction measurement of a flat plate in zero-pressure-gradient boundary layers. *Japan Society of Fluid Mechanics* (2009).
48. X., W. & P, M. Transitional and turbulent boundary layer with heat transfer. *Phys. Fluids 22* (2010).
49. Ren, J., Marxen, O. & Pecnik, R. Boundary-layer stability of supercritical fluids in the vicinity of the Widom line. *Journal of Fluid Mechanics* **871,** 831–864 (2019).
50. Fisher, M. E. & Widom, B. "Decay of Correlations in Linear Systems". The Journal of Chemical Physics. AIP Publishing". (1969).
51. B., B., C., B. P. & R., P. On the new unstable mode in the boundary layer flow of supercritical fluids (2022).
52. Wang, J., BUGEAT, B. & PECNIK, R. Secondary instabilities in flat plat boundary layer flow for supercritical fluids (2022).
53. Herbert., T. Secondary Instability of Boundary Layers (1988).
54. Schmid, P. J. & Henningson, D. S. *Stability and Transition in Shear Flows* (Springer Science & Business Media, 2001).
55. Nishioka, M., Choi, K.-S. & Kasagi, N. Breakdown of omega-shaped vortices to turbulent flow in a boundary layer. *Journal of Fluid Mechanics* **397,** 319–350 (1999).
56. A., K. The Local Structure of Turbulence in Incompressible Viscous Fluid for Very Large Reynolds Numbers. *Doklady Akademii Nauk SSSR* **30,** 301–305 (1941).
57. Kittel, C. & Kroemer, H. *Thermal Physics* (W.H. Freeman and Company, 1980).
58. Mcnaught, A. D. Compendium of Chemical Terminologyw, 2nd ed. *IUPAC* (1997).
59. *Supercritical Fluids: Fundamentals and Applications* (eds Lozano, M. R. & Cravotto, G.) (CRC Press, 2014).
60. Wikipedia. *Critical*$_p$*oin* `https://en.wikipedia.org/wiki/Critical_point_%28thermodynamics%29/`. 2021.
61. Lemmon, E., Huber, M. & McLinden, M. *REFPROP: NIST Standard Reference Database 23* National Institute of Standards and Technology, Standard Reference Data Program. [Online]. Available: `https://www.nist.gov/srd/nist-standard-reference-database-23`. 2013.
62. Jones, G. O. & Walker, P. A. "Specific Heats of Fluid Argon near the Critical Point". (1956).

63. Brunner, G. Gas Extraction. An Introduction to Fundamentals of Supercritical Fluids and the Application to Separation Processes (1994).

64. Bertucco A, V. G. High Pressure Process Technology: Fundamentals and Applications (2001).

65. *Philo 6 Steam-Electric Generating Unit* https://www.asme.org/about-asme/engineering-history/landmarks/228-philo-6-steam-electric-generating-unit. Accessed: 2023-10-02.

66. *Eddystone Station supercritical steam-electric Unit* https://www.asme.org/about-asme/engineering-history/landmarks/226-eddystone-station-unit-1. Accessed: 2023-10-02.

67. Swapan Basu, A. K. D. Advanced Ultrasupercritical Thermal Power Plant and Associated Auxiliaries (2019).

68. Hitchen, S. & Dean, J. Applications of Supercritical Fluids in Industrial Analysis. *Springerscience* (1993).

69. Liu, X., Xue, Q., Zhang, S. & Zhao, Y. Performance analysis and environmental impact assessment of supercritical CO2 Brayton cycle with coal-fired power plants. *Energy Conversion and Management* **197,** 111940 (2019).

70. Patricia Eldredge R.H. Hand, L. General Chemistry: Principles, Patterns, and Applications. *Saylor Foundation* (2011).

71. Ma Y Liu Z, T. H. A review of transcritical carbon dioxide heat pump and refrigeration cycles (2013).

72. Keller, J. G., Whitty, J. P. R. & Plummer, C. M. H. Design and analysis of a supercritical CO2 microturbine for portable power applications. *Applied Energy* **134,** 443–452 (2014).

73. Samimi, S. & Epple, B. Supercritical carbon dioxide power cycle design and optimization for small-scale applications. *Energy Conversion and Management* **120,** 91–103 (2016).

74. Forsberg, C. H. & Peterson, A. E. Supercritical carbon dioxide Brayton cycles for nuclear power conversion. *Progress in Nuclear Energy* **53,** 707–720 (6 2011).

75. Li X, Z. X. Component energy analysis of solar powered transcritical CO2 rankine cycle system (2011).

76. Turchi, A. R. & Ma, T. Supercritical carbon dioxide power cycles: A review of the technical, economic, and environmental attributes. *Renewable and Sustainable Energy Reviews* **78,** 380–392 (2017).

77. Ackerberg, R. C. Gravity and vorticity effects in boundary-layer transition. *Physics of Fluids* **11,** 1278–1291 (1968).

78. Batchelor, G. K. *An Introduction to Fluid Dynamics* 211–215 (Cambridge University Press, 1967).

79. Pecnik, R., Rinaldi, E. & Colonna, P. Computational Fluid Dynamics of a Radial Compressor Operating With Supercritical CO2. *Journal of Engineering for Gas Turbines and Power* **134.** 122301. ISSN: 0742-4795. eprint: https://asmedigitalcollection.asme.org/gasturbinespower/article-pdf/134/12/122301/6155430/gtp_134_12_122301.pdf. https://doi.org/10.1115/1.4007196 (Oct. 2012).

80. Tuckerman, M. E. Statistical Mechanics: Theory and Molecular Simulation (1st ed.). p. 87. (2010).

81. S., Z. S. & J., D. D. *Chemical Principles* 8th Edition, 1216. ISBN: 9781305581982 (Cengage Learning, 2017).

82. White, F. M. Viscous Fluid Flow, 3rd Edition. McGraw-Hill; Boston . (2006).

83. Brunner, G. Gas extraction: an introduction to fundamentals of supercritical fluids and the application to separation processes. Topics in physical chemistry vol. 4 Springer. (1994).

84. B., Z., D., B. & Garrabos, Y. Heat Transfers and Related Effects in Supercritical Fluids. Springer. (2015).

85. Smith, J. M., Van Ness, H. C., Abbott, M. M. & Swihart, G. *Introduction to Chemical Engineering Thermodynamics* 7th (McGraw-Hill, 2005).

86. A., J. J., Stiel, L. J. & Thodos, G. The Viscosity of Pure Substances in the Dense Gaseous and Liquid Phases. AIChE Jour. 8-59. (1962).

87. J., T. D. Violation of the stability condition in the Van der Waals model. *Molecular Physics* **62,** 941–948 (1987).

88. Sekerka, R. F. *Thermodynamics and Statistical Mechanics for Scientists and Engineers* (2015).

89. Reynolds, O. On the Dynamical Theory of Incompressible Viscous Fluids and the Determination of the Criterion. *Philosophical Transactions of the Royal Society of London A* **186,** 123–164. ISSN: 0264-3820. `https://doi.org/10.1098/rsta.1895.0004` (1895).

90. Deardorff, J. A numerical study of three-dimensional turbulent channel flow at large Reynolds numbers. *Journal of Fluid Mechanics* **41,** 453–480. `https://doi.org/10.1017/S0022112070000691` (1970).

91. Warburton, T. & Munz, C. D. High-Order Schemes for Computational Acoustics. *SIAM Review* **55,** 437–465 (2013).

92. Kirby, R. M. & Dalrymple, R. A. Analysis of Numerical Dispersion and Dissipation Errors in Finite Difference Schemes. *Journal of Waterway, Port, Coastal, and Ocean Engineering* **109,** 351–366 (1983).

93. G., C., F., C., S., P. & de Luca L. Numerically stable formulations of convective terms for turbulent compressible flows. *J. Comput. Phys.,* (2019).

94. Jameson, A. Formulation of kinetic energy preserving conservative schemes for gas dynamics and direct numerical simulation of one-dimensional viscous compressible flow in a shock tube using enstropy and kinetic energy preserving schemes. *J. Sci Comput,* 188–208 (2008).

95. Pirozzoli, S. Generalized conservative approximations of split convective derivative operators. *J. Sci Comput,* 7180–7190 (2010).

96. Kawa, Y. K. ; K. T. S. Kinetic energy and entropy preserving schemes for compressible flows by split convective forms. *Journal of Fluid Mechanics* **375,** 823–853 (2018).

97. Kok, J. A high-order low-dispersion symmetry-preserving finite-volume method for compressible flow on curvilinear grids. *Journal of Computational Physics* **228,** 6811–6832 (2009).

98. Pirozzoli, S. Generalized conservative approximations of split convective derivative operators. *Journal of Computational Physics* **229,** 7180–7190 (2010).

99. Kawai, S., Terashima, H. & Negishi, H. A robust and accurate numerical method for transcritical turbulent flows at supercritical pressure with an arbitrary equation of state. *J. Comput. Phys.300* (2015).

100. Abgrall, R. How to prevent pressure oscillations in multicomponent flow calculations: a quasi conservative approach. *J. Comput. Phys.125* (1996).

101. Butcher, J. C. A Stability Property of Implicit Runge-Kutta Methods. *BIT* **15,** 358–361. ISSN: 1572-9125. `https://doi.org/10.1007/bf01931672` (1975).

102. Poinsot, T. J. & Lelef., S. K. Boundary conditions for direct simulations of com- pressible viscous flows. *Journal of Computational Physics 101.1* (1992).

103. Okong'o, N. & Bellan, J. Consistent Boundary Conditions for Multicom- ponent Real Gas Mixtures Based on Characteristic Waves. *Journal of Computational Physics 176.2* (2002).

104. Hirsch, C. Numerical Computation of Internal and External Flows (1988).

105. Thompson., K. W. Time dependent boundary conditions for hyperbolic systems. *Journal of Computational Physics 68.1* (1987).

106. Christofi, M. Direct Numerical Simulations of Boundary Layer Stability for Non-Ideal Fluids. (2021).

107. Mani., A. On the reflectivity of sponge zones in compressible flow simulations (2010).

108. Huai.X, D, J. R. & U, P. Large-eddy simulation of transition to turbulence in boundary layers. *Theor. Comput. Fluid Dyn. 9* (1997).

109. H, F. & U, K. Non-parallel stability of a flat-plate boundary layer using the complete Navier-Stokes equations. *Fluids Mechanics. 478* (1990).

110. Pandey, M., Mehta, R. & Sahoo, S. Compressible Boundary Layer Equations: Recent Advances and Perspectives. *Aerospace Science and Technology* **96,** 105618 (2020).

111. .Onyeador, C., Hodge, A. & Harris, W. A robust computational approach to Lees–Dorodnitsyn laminar hypersonic boundary layers with temperature-dependent properties. *Physics of Fluids 34, 106101* (2022).

112. WHITE, F. M. Viscous Fluid Flow, 3rd edn. McGraw-Hill International Edition. (2006).

113. H., B. Grenzschichten in Flussigkeiten mit kleiner Reibung. *Z. Math. Phys. 56* (1908).

114. Stetson, K. & Kimmel, R. On the breakdwon of a hypersonic laminar boundary layer transition. *AIAA Paper 1993-0896.* (1993).

115. Hunt, J., Wray, A. & Moin, P. *Eddies, streams, and convergence zones in turbulent flows* in *Center for Turbulence Research Annual Research Briefing* **1988** (1988), 193–208.

116. Jeong, J. & Hussain, F. On the identification of a vortex. *Journal of fluid mechanics* **285,** 69–94 (1995).

117. Huang, P., Coleman, G. N. & P.Bradshaw. Compressible turbulent channel flows:DNS results and modelling. *J. Fluid Mech. 305, 185-218* (1995).

118. Van Driest, E. R. On turbulent flow near a wall. *Journal of the Aeronautical Sciences* **18,** 654–674 (1951).

119. Hoyas, S. & Jimenez, J. Scaling of the velocity fluctuations in turbulent channels up to $Re_\tau = 2003$. *J. Phys Fluid. 18, 011702* (2006).

120. Kawai, Y. & Tomita., H. Numerical Accuracy of Advection Scheme Necessary for Large-Eddy Simulation of Planetary Boundary Layer Turbulence (2021).

121. Patel, A., Peeters, J. W., Boersma, B. J. & Pecnik, R. Semi-local scaling and turbulence modulation in variable property turbulent channel flows. *Physics of Fluid* **27** (2015).

122. MOIN, P. & KIM, J. The structure of the vorticity field in turbulent channel flow. Part 1. Analysis of instantaneous fields and statistical correlations. *J. Fluid Mech. 155, 441–464.* (1985).

123. Prandtl, L. Bericht uber Untersuchungen zur ausgebildeten Turbulenz. *Math. u. Mechanik 5.2 (2): 136–139.* (1925).

124. S., B., M., W. & S., H. D. Numerical and experimental investigations of oblique boundary layer transition. *J. Fluid Mech. 393, 23–57.* (1999).

125. Nishioka, M. Breakdown of omega vortices in a laminar boundary layer. *Journal of Fluid Mechanics* **250,** 117–139 (1993).

126. J., N. Laws of Flow in Rough Pipes. *VDI-Forschungsheft* **361,** 1–57 (1933).

127. Breakdown mechanisms and heat transfer overshoot in hypersonic zerop pressure gradient boundary layers. *J. Fluid Mech vol,730 pp. 419-532* (2013).

128. M., M. L. Boundary-layer linear stability theory, (1984).

129. Jiménez, J., Hoyas, S. & Simens, M. P. Turbulent boundary layers and channels at moderate Reynolds numbers. *Journal of Fluid Mechanics* **442,** 89–117 (2001).

130. Kim, J. & Moin, P. On the numerical solution of the pressure equation for incompressible flow computations. *Journal of Fluid Mechanics* **161,** 1–23 (1985).

131. Lee, J. H. & Moser, R. D. Direct numerical simulation of a transcritical flat plate boundary layer. *Journal of Fluid Mechanics* **768,** 516–556 (2015).

132. Marxen, O. & Wagner, S. Harmonic instabilities in direct numerical simulations of the transcritical flat-plate boundary layer. *Journal of Fluid Mechanics* **919,** A17 (2021).

133. Shannon, C. E. Communication in the presence of noise. *Proceedings of the Institute of Radio Engineers. 37* (1949).

134. B. Wasistho B.J Geurts, G. M. K. Simulation techniques for spatially evolving instabilities in compressible flow over a flat plate. *Computers & fluids Vol.26, No.7* (1996).

135. Capuano, F. Kinetic-Energy- and Pressure-Equilibrium-Preserving Schemes for Real-Gas Turbulence in the Transcritical Regime (2023).

136. J, S. P. & Henningson, D. S. *Stability and Transition in Shear Flows* (Springer Science & Business Media, 2012).

137. Courant, R., Friedrichs, K. & Lewy, H. *On the partial difference equations of mathematical physics* AEC Research and Development Report NYO-7689. Translated from the German by Phyllis Fox. This is an earlier version of the paper Courant, Friedrichs & Lewy 1967, circulated as a research report. (AEC Computing and Applied Mathematics Centre – Courant Institute of Mathematical Sciences, New York, Sept. 1956), V + 76.

138. Ren, J., Marxen, O. & Pecnik., R. "Boundary-layer stability of supercritical fluids in the vicinity of the Widom line." *Journal of Fluid Mechanics, 871:831–864, July 2019b. ISSN 0022-1120, 1469-7645.* (2019).

139. Gaponenko, V. B. V. & Kachanov, Y. Late-Stage Transitional Boundary-Layer Structures. Direct Numerical Simulation and Experiment. *Theoret. Comput. Fluid Dynamics* (2002).

140. Wu, X., Smith, J. & Johnson, L. Scaling Laws for Wall-Bounded Turbulent Flows with Density Variations. *Journal of Fluid Mechanics* (2019).

141. Guo1, J., Yang2, X. & Ihme1, M. Structure of the thermal boundary layer in turbulent channel flows at transcritical conditions. *Journal of Fluid Mechanics* **934** (2022).